

KING'S COLLEGE LONDON

DOCTORAL THESIS

**Computational haemodynamics and strain
analysis of aortic dissection in idealised and
patient specific aortic geometries: Understanding
the impact of dissection on cardiovascular
function**

Author:

DESMOND DILLON-MURPHY

Supervisors:

C. ALBERTO FIGUEROA, *Ph.D.*
DAVID A. NORDSLETTEN, *Ph.D.*

A thesis submitted in fulfilment of the requirements

for the degree of Doctor of Philosophy

DIVISION OF IMAGING SCIENCE & BIOMEDICAL ENGINEERING

SCHOOL OF MEDICINE

February 2016

KING'S
College
LONDON

ABSTRACT

Aortic dissection (AD) is characterised by the delamination of the aortic intima and the creation of a true and false lumen and has a high associated incidence of mortality. Morphology can vary significantly between patients and it has been observed that patients with similar morphology exhibit different outcomes: some present a stable patent false lumen for many months or even years, others exhibit stable full thrombus formation, and lastly a third group exhibits partial thrombus which has been associated with high morbidity relative to no thrombus formation. The haemodynamic conditions which lead to these outcomes still remain a subject of debate.

This dissertation describes a number of different studies that have utilised a variety of techniques to investigate a multitude of aspects of the haemodynamics experienced in cases of AD through four novel studies.

The primary study involves a patient specific analysis of an AD and aims to gather insight into the complex haemodynamics in AD using a variety of medical image data and Computational Fluid Dynamics (CFD). Several computer models of the aorta were created whereby morphometric parameters related to the dissection septum were altered, such as removal of the septum, and the variation of the number of connecting tears between the lumina. Patient-specific flow data at the inlet and 0D lumped parameter models representing the distal vasculature at each outlet were set to match 2D Phase Contrast-Magnetic Resonance Imaging (PC-MRI) flow data from the patient. Haemodynamics in the dissected aorta were compared to those in an equivalent healthy aorta, created by virtually removing the intimal flap (septum). Local regions of increased velocity, pressure, wall shear stress and alterations in flow distribution were noted. The computed flow pat-

terns compared favourably with those obtained using 4D PC-MRI. A lumped-parameter heart model was subsequently used to show that in this case there was an estimated 14% increase in left ventricular stroke work with the onset of dissection. Finally, the effect of secondary connecting tears (i.e. those excluding the primary entry and exit tears) was also studied, revealing significant haemodynamic changes when no secondary tears are included in the model, particularly in the true lumen where increases in flow over +200% and drops in peak pressure of 18% were observed.

Study 2 examines a wide variety of anatomical risk factors which have been implicated in the progression of AD. Sixteen idealised CAD models were created. Individual geometric features were altered in a controlled manner between each model with the aim of examining the degree to which haemodynamics are altered by features such of curvature, location of false lumen relative to the aortic curvature, and the patency and size of entry and exit tears. The study highlights the important role that tear patency plays in pulse pressure and mean pressure with the largest change seen with the exit tear occluded, leading to a 144% increase in pulse pressure and 7% increase in mean pressure.

Study 3 investigates quantification of strain in the aorta of a number of healthy subjects and AD patients. Dual phase black blood MRI and 3D segmentation techniques were utilised in an attempt to quantify the longitudinal, circumferential and volumetric strain the aorta experiences during the normal cardiac cycle, measurements being made via the tracking of material points in a Lagrangian framework. The analyses of the data show AD patients exhibit a wide variation of strains depending on the measurement location and the lumen being examined. There is a complex interplay between the true and false lumina. The data also suggest conditions which may be conducive to peeling and mode I type fracture.

Study 4 attempts to quantify the influence that compliance of the lumina has on hae-

modynamics via the use of a 0D model based on the 3D model created for the primary study. With large values of stiffness in the lumina this 0D model, while simple, provides a relatively faithful replication of the rigid 3D simulation. Conversely, when luminal compliance is included the results better match those observed with 2D PC-MRI suggesting compliance in the 3D domain is crucial to accurately model AD haemodynamics.

Understanding of false lumen haemodynamics and dynamics may help identify patients at risk of aortic growth, potentially aiding treatment planing. These studies have utilised image data, segmentation, and CFD to offer insight into the detrimental effects introduced by the AD flap on heart workload, tissue perfusion, false lumen pressure and thrombus formation, etc. as well as examining the effect compliance plays in AD. An improved understanding of these haemodynamics may ultimately provide a non-invasive method for patient risk stratification.

ACKNOWLEDGEMENTS

A life spent making mistakes is not only more honourable, but more useful than a life spent doing nothing.

-George Bernard Shaw

There are so many people I need to thank. Firstly, I certainly would not have got to this stage without the help and dedication of both my supervisors, Alberto and Dave, who through gritted teeth and dogged determination dragged me to today, and its to them that I owe my biggest thanks. I won't look fondly back on my first few months of this PhD and I will likely never forget that time, but I will all appreciate what getting through it did for me. I will also never forget the lengths, in both physical miles travelled and time given, and I will forever appropriate Alberto for continuing to supervise and guide me from 6,079 km away.

Special thanks goes to all those who do and have made up our fantastic lab. First of all, my partner in AD crime. Thanks Alia. Chris, you have persistently smiled at my bad bad jokes. You're a great mate, and Greggs is a fine institution. Slava is an apt name for the man who is a hero with the code. You've built one of the best bits of academic software out there. Be safe on the bike Miguel and keep it up, you're doing awesome simulations. Pouya, you're a legend. Nan the man, and the first friend I made in KCL who always had time for me. **Dr.** Kev-La, Caoimhín, the quiet birth; my brotha from another motha with 1/18 Irish in ye. I miss you big dawg. Fede, Ah... Aladino, some day we'll know what controls the flow, but we'll always know the lefter the worster (we still have to organise that trip). And while I'm talking about the mates in Michigan I miss, a

massive thanks to Miquel, Jonas and Amaia for making me welcome when I came. And of course, who could forget Ed?

I will always remember those I have met in KCL. They are not only some of the most talented, professional and hard working scientists around, but also fantastic people I feel proud to know. A big thanks to the guys who did the Tommies Social. You were great guys to work with and I will be back. Ross, I'm looking forward to seeing ye at MorganStock 2016. Sally, you're as amazing as your stories and you always have milk to hand. Andrew and all of the IT team and admin staff, Marie, keep me entertained with more tales of puppet adventure, Simone, I may never forgive you for that karaoke, I don't think the rest of the pub will either, Big Nick, perhaps the most Kiwi lad I know who I don't think I ever heard talk about rugby, Matt, you're as keen as Fede for that Nutella, there's way too many people to remember, but you all know who you are. A big special thanks goes to Eoin. Go bhfuil tú ar an ghaoth faoi bhun mo sciatháin, the D'arc to my Drico. We've had some great times being stereotypical in this town, the night watching the filming of 'Aul Jimmy Bond being a high point, let's keep at it sure.

But I owe as much of the thanks to my family and friends. Jenny for being the best sister anyone could ever hope to have. Ciaran, you're the guy I want to be when I grow up, despite the fact you're 12 years my junior. You're the most inspirational, talented guy and I'm proud to call you my brother. Ronan, I'll always be there for you. Fran, my stunningly beautiful girlfriend for supporting me and putting herself in the rarefied air of being one of the tiny population who will actually read this. I am still glad I got on the wrong flight that day. Liam, Johnny, Marc, Rory, Zazer, et al., you're such a savage bunch of mates. I miss you all, and while we're on it, thanks to Dublin, this is a true tale of two cities. To all the attendees of der penthaus over the years, thanks for putting up with me, and a special thanks to my first running mate here, Niall, the guy who made

me feel at home in London.

Most of all though, thanks to my amazing Mom and Dad. You have always been there for me and undertaking this PhD was no exception. Dad, thanks for giving me the strength to keep going with it when I thought I couldn't, Mom thanks for pulling out all the stops when I needed it.

And finally, thanks to whomever decides to pick this up and read it. A bold choice.

PUBLICATIONS

Publications arising from this thesis:

- 1 **Desmond Dillon-Murphy**, Alia Noorani, David Nordsletten and C. Alberto Figueroa, *Multi-modality image-based computational analysis of haemodynamics in aortic dissection*, Biomech. Model. Mechanobiol. (2015), doi:[10.1007/s10237-015-0729-2](https://doi.org/10.1007/s10237-015-0729-2)
- 2 Sabrina Ben Aïmed, **Desmond Dillon-Murphy** and C. Alberto Figueroa, *Computational Study of Anatomical Risk Factors in Idealized Models of Type B Aortic Dissection* Eur J Vasc Endovasc Surg. (Under review)
- 3 **Desmond Dillon-Murphy**, Alia Noorani, Markus Henningsson and C. Alberto Figueroa, *Strain quantification via dual phase black blood MRI in healthy and aortic dissection subjects*, (Under review)

CONFERENCES ATTENDED

- SITE 2013, *Barcelona, Spain* - Preliminary models Section [3.1](#) - Poster Presentation
- MECbioeng 2013, *Ascot, London* - Preliminary results Section [4.1](#) - Oral Presentation
- UK Bioengineering Conference 2013, *Strathclyde* - Preliminary results Section [4.1](#) - Oral Presentation
- CMBE 2013, Hong Kong - Preliminary results Section - [4.1](#) - Oral Presentation
- MECbioeng 2014, London - Results Section - [4.1](#) - Oral Presentation

- MEIBioEng meeting 2015, *Leeds* - Results Section 4.2 - Oral Presentation
- CMBE 2015, *Cachan, Paris* - Results Section 4.2 - Oral Presentation

OTHER DISTINCTIONS

- Best poster, SITE Barcelona 2013
- Best presentation, MECbioeng 2013
- Cover image of Encyclopaedia of Computational Mechanics, Vol. III, Fluids, *Stein, Erwin and De Borst, Rene and Hughes, Thomas J. R.*, 2016 edition

OTHER NOTABLE PUBLICATIONS

- Federica Cuomo, Sara Roccabianca, **Desmond Dillon-Murphy**, Nan Xiao Jay D. Humphrey, and C. Alberto Figueroa, *Effects of Age-Associated Regional Changes in Human Central Artery Mechanics on Systemic Hemodynamics Revealed by Computational Modeling*, Am J Hyperten (Under review)
- Nicholas Gaddum, **Desmond Dillon-Murphy**, Richard Arm, Gareth Morgan, Tobias Schaeffter, Tarique Hussain, *Increased Aortic Strain and Strain Rate in Aortic Coarctation Treated with Stent Angioplasty; An Experimental and Clinical Study*, (Under review)

CONTENTS

Abstract	2
Unit conversion table	18
Glossary	19
1 Introduction	1
1.1 Overview	2
1.2 Primary patient specific study	4
1.3 Computational Study of Anatomical Risk Factors	6
1.4 Strain quantification via dual phase black blood MRI	7
1.5 Impact of septum distensibility on simulated haemodynamics using a LPN	7
1.6 Thesis structure	8
2 Motivation	10
2.1 Clinical Background	11
2.1.1 Pathogenesis	11
2.1.2 Etiology	12
2.1.3 Classification	16
2.1.4 Diagnosis	19
2.1.5 Management	19
2.1.6 Follow up	21
2.1.7 Summary	23
3 Methods	28
3.1 Primary patient specific study	29

Contents	11
<hr/>	
3.1.1 Patient Details	29
3.1.2 Imaging	29
3.1.3 Computational fluid dynamics	36
3.2 Computational study of anatomical risk factors	44
3.3 Strain quantification via dual phase black blood MRI	48
3.3.1 Image acquisition	48
3.3.2 Strain Measurements	49
3.3.3 Image analysis	51
3.3.4 Image segmentation	52
3.3.5 Dimensional measures and strain calculations	53
3.4 Impact of septum distensibility on simulated haemodynamics using a LPN	55
4 Results	57
4.1 Primary patient specific study	59
4.1.1 Investigation 1: Haemodynamic alterations in AD	59
4.1.2 Investigation 2: Analysis of the impact of the flap on left ventricular function	70
4.1.3 Investigation 3: Sensitivity study of the impact of secondary entry tears	72
4.2 Computational study of anatomical risk factors	78
4.2.1 Haemodynamic alterations in undissected and dissected aortic models	79
4.2.2 Impact of curvature	82
4.2.3 Impact of FL location relative to aortic curvature	82
4.2.4 Impact of tear size - proximal and distal tears of equal size	84
4.2.5 Impact of the tear size - proximal and distal tear of different sizes	86
4.2.6 Impact of tear shape	90

Contents	12
4.2.7 Impact of tear patency	90
4.3 Strain quantification via dual phase black blood MRI	93
4.3.1 Measurement locations	93
4.3.2 Healthy subjects	94
4.3.3 Aortic dissection patients	97
4.4 Impact of septum distensibility on simulated haemodynamics using a LPN	101
5 Discussion	107
5.1 Primary patient specific study	108
5.2 Computational Study of Anatomical Risk Factors	113
5.3 Strain quantification via dual phase black blood MRI	117
5.4 Impact of septum distensibility on simulated haemodynamics using a LPN	122
5.5 Potential of AD modelling	123
6 Conclusions	125
6.1 Primary patient specific study	126
6.1.1 Limitations	126
6.2 Computational Study of Anatomical Risk Factors	129
6.2.1 Limitations	130
6.3 Strain quantification via dual phase black blood MRI	130
6.3.1 Limitations	131
6.4 Impact of septum distensibility on simulated haemodynamics	132
6.4.1 Limitations	133
7 Future Work	134
7.1 Imaging	135
7.2 Pressure data	136
7.3 Lack of compliance in 3D domain	136

7.3.1	Immersed boundary method	139
7.3.2	Fictitious domain method & mortar element method	140
7.3.3	Immersed finite element	140
7.3.4	Immersed structural potential method	141
7.4	Potential for future studies	141
8	Other contributions	142
8.1	Introduction	143
8.2	Effects of Age-Associated Regional Changes	143
8.2.1	Overview	143
8.2.2	Contribution: CAD modelling	144
8.3	Haemodynamic and morphological changes over time	147
8.4	Patient specific segmentation for 3D printing	151
8.4.1	Experimental aortic coarctation simulation to assess the interaction of stents with haemodynamics and arterial wall	151
8.4.2	Haemodynamic and strain alterations arising from varying tear patency in cases of aortic dissection	154
	Bibliography	156

LIST OF FIGURES

2.1	Motivation: AD pathogenesis	13
2.2	AD classification	17
2.3	AD classification flowchart	18
2.4	Motivation: AD thrombus configuration	24
2.5	Motivation: AD mechanics	27
3.1	Primary patient specific study: Available image data	30
3.2	Primary patient specific study: Abdominal CT data and AD segmentation process	32
3.3	Primary patient specific study: Undissected and dissected models	35
3.4	Primary investigation: Boundary conditions	38
3.5	Primary patient specific study: Mesh adaptation	43
3.6	Anatomical Risk Factors in Idealised Models study: Idealised models schematic	45
3.7	Strain quantification study: Lagrangian and Eulerian measurements in the aorta	51
3.8	Strain quantification study: Magnitude and gradient image	53
3.9	Strain quantification study: Measures of strain	55
4.1	Primary patient specific study: Undissected model results	62
4.2	Primary patient specific study: Baseline dissected model results	63
4.3	Primary patient specific study: Regions affected due to the presence of AD	65
4.4	Primary patient specific study: 2D PC-MRI versus CFD flow results	67

4.5	Primary patient specific study: versus versus CFD velocity results at peak systole	68
4.6	Primary patient specific study: Inflow waveforms and PV loops	72
4.7	Primary patient specific study: CFD V 4D PC-MRI	73
4.8	Primary patient specific study: Effect of tear patency on TL and FL flow and pressure	75
4.9	Primary patient specific study: Effect of altering number of secondary patent tears	77
4.10	Anatomical risk factors in idealised models study: Pressure alterations in undissected and dissected aortic models	80
4.11	Anatomical risk factors in idealised models study: Impact of curvature	83
4.12	Anatomical risk factors in idealised models study: Impact of FL location relative to aortic curvature	85
4.13	Anatomical risk factors in idealised models study: Impact of tear size - proximal and distal tears of equal size	87
4.14	Anatomical risk factors in idealised models study: Impact of tear size - proximal and distal tears of different sizes	88
4.15	Anatomical risk factors in idealised models study: Impact of tear shape	91
4.16	Anatomical risk factors in idealised models study: Impact of tear patency	92
4.17	Strain quantification study: Selected material planes in the aorta	95
4.18	Strain quantification study: Typical aortic strain measures in a healthy volunteer	96
4.19	Strain quantification study: Healthy subject strains	98
4.20	Strain quantification study: Aortic strain in dissected patient A	99
4.21	Strain quantification study: Aortic strain in dissected patient B	100
4.22	0D AD Study: 0D AD Circuit	103

4.23	Impact of septum distensibility on simulated haemodynamics: pressures and flows	106
5.1	Primary patient specific study: Example of direct 3D segmentation	109
5.2	Primary patient specific study: 2D PC-MRI	110
5.3	Anatomical risk factors in idealised models study: Laplaces law	115
5.4	Strain quantification Study: Aortic root motion	118
5.5	[Strain quantification Study: Strain distribution in vessels with curvature	121
5.6	[Strain quantification Study: Mode I crack propigation	121
8.1	Other Contributions - Ageing study: Illustrative 3D geometrical models .	146
8.2	Other Contributions - Time related changes in AD: Example geometries .	149
8.3	Other Contributions - Time related changes in AD: Initial results example	150
8.4	Other Contributions - Patient Specific segmentation for 3D printing: Patient A: CAD models	152
8.5	Other Contributions - Patient Specific segmentation for 3D printing: Patient A: Final phantom model	153
8.6	Other Contributions - Patient Specific segmentation for 3D printing: Patient B: CAD model of AD	155

LIST OF TABLES

1	Unit conversion table	18
3.1	Primary patient specific study: Scan settings for both thoracic and abdominal CTA scans of an AD subject	31
3.2	Primary patient specific study: Scan settings for scans of an AD subject.	33
3.3	Strain quantification study: Subject details	48
4.1	Primary patient specific study: RCR parameters for investigation 1	60
4.2	Primary patient specific study: Heart model parameters	71
4.3	Primary patient specific study: Mesh sizes	74
4.4	Anatomical risk factors in idealised models study: Mean flows	81
4.5	Anatomical risk factors in idealised models study: Peak velocities	81
4.6	0D AD Study: Component description	103

UNIT CONVERSION TABLE

Table 1: Unit conversion table

Property	SI Units	Units preferred in text	Equivalent Conversions
Length	m	1 mm	0.039 in
Area	m ²	1 mm ²	0.01 cm ²
Volume	m ³	1 mm ³	6.102 × 10 ⁻⁵ in ³ s ⁻¹
Volume flow rate	m ³ s ⁻¹	1 mm ³ s ⁻¹	6.102 × 10 ⁻⁵ in ³ s ⁻¹
Weight	kg	1 g	0.002 lb
Velocity	m s ⁻¹	1 mm s ⁻¹	0.039 in s ⁻¹
Pressure	kg m ⁻¹ s ⁻²	1 mmHg	133.3 Pa
WSS	Pa	1 dyne cm ⁻²	0.1 Pa
Density	kg m ⁻³	1 g ml	1 g cm ⁻³
Viscosity	kg m ⁻¹ s	1 mPa s	0.001 PI
Hydraulic Resistance (<i>R</i>)	km m ⁻⁴ s ⁻¹	1 g mm ⁻⁴ s ⁻¹	10,000 g cm ⁻⁴ s ⁻¹
Vessel Compliance (<i>C</i>)	m ⁴ s ² kg ⁻¹	1 mm ⁴ s ² g ⁻¹	1 × 10 ⁻⁴ cm ⁴ s ² g ⁻¹
Fluid inductance (<i>L</i>)	kg m ⁻⁴	1 g cm ⁻⁴	10,000 g cm ⁻⁴
Stiffness/Young's modulus	Pa	1 Pa	1.45 × 10 ⁻⁴ PSI
Voltage	V	1 mV	
Preload	kg m ⁻¹ s ⁻²	1 g mm ⁻¹ s ⁻²	1 Pa
Elastance	kg m ⁻⁴ s ⁻²	1 g mm ⁻⁴ s ⁻²	1.45 × 10 ⁻⁴ PSI
Work	J	1 kJ	1000 kg m ² s ⁻²
			737.6 ft lb
			0.94782 BTU

GLOSSARY

2D PC-MRI Flow sensitive Phase Contrast MRI (PC-MRI) with Velocity Encoding (VENC) in a single direction acquired at a plane. 15, 17, 30, 33, 55, 56, 58, 63, 65, 66, 81, 83, 84, 88, 90–92, 98, 100, 125, 128–130, 132, 134, 136, 146, 147, 152, 154, 157, 158, 160, 172, 175

3DSSFP 3D Steady-state free precession MRI. 176

4D PC-MRI Flow sensitive PC-MRI with VENC in 3 directions acquired at a single plane or as an image stack. 28, 30, 47, 55, 56, 92, 96–99, 132, 160

AA Aortic Arch. 78, 117–121, 123–125, 141, 143, 144

AAo Ascending Aorta. 78, 117–121, 123–125, 141–143

AD Aortic Dissection. 14, 17, 25, 27–34, 36–52, 54–59, 69–71, 73, 76, 78, 80, 83–85, 88, 89, 94–96, 102, 117, 118, 121, 125–127, 132–138, 143, 147, 148, 152–158, 161, 166, 168, 172, 174, 175, 179, 180

ALE Arbitrary Lagrangian-Eulerian. 163, 164, 166

Antihypertensive A class of drugs used to treat hypertension. 46, 54, 133

Apoptosis The process of programmed cell death. 40

ASL Arterial spin labelling. 161

Atherosclerosis The accumulation of plaques of fatty streaks (white blood cells) leading to the thickening of the arterial wall. 40

BPM Beats per Minute. 58, 71

- CAD** Computer Aided Design. 31, 58, 69, 78, 102, 126, 152, 156, 169, 177, 180
- CFD** Computational Fluid Dynamics. 14, 15, 28, 29, 31–33, 51, 56, 71, 80, 90–92, 96–98, 125, 128, 130, 133, 136, 137, 146–148, 154, 161, 176
- Cf-PWV** Carotid-to-Femoral Pulse Wave Velocity (PWV). 168, 169
- CRP** C-reactive protein. 44
- CS** Coronary Sinus. 170, 171
- CT** Computed X-Ray Tomography. 14, 30, 43, 57, 97–99, 132, 147, 152, 160, 161, 172, 174, 175
- CTA** Computed X-Ray Tomography Angiography. 17, 30, 44, 46, 47, 55–57, 59, 96
- DA** Descending Aorta. 78, 84, 85, 88, 98, 117–121, 123–125, 130, 141–144
- DInoA** Distal to the **Innominate Artery** (InoA). 118, 119, 125, 143
- E_{Cir} Circumferential Strain. 76, 79, 117, 118, 120–125, 141, 144
- E_{Long} Longitudinal Strain. 76, 79, 117, 118, 121, 122, 125, 141, 142, 144
- E_{Vol} Volumetric Strain. 76, 77, 79, 117, 118, 121, 122, 125, 141, 143, 144
- ECG** Electrocardiogram. 58, 74
- Elastolysis** Deficits in the elastic tissue. 40
- Endovascular Aortic Repair** Repair of the aorta using a stent graft. See Section 2.1.5.
20, 29
- EVAR** Endovascular Aortic Repair. 20, 29
- FDM** Fictitious Domain Method. 165
- FE** Finite Element. 61, 71

FEM Finite Element Method. 165

FL False Lumen. 15, 27–31, 36–38, 42, 44–52, 54, 57–59, 69, 70, 72, 78, 80, 84, 88, 90–93, 96, 98–100, 102–118, 121, 123–125, 127–130, 132–140, 143–145, 147, 148, 151–157, 160, 162, 166, 172–174, 179, 180

FSI Fluid Structure Interaction. 80, 147, 154, 166, 169, 179

GAG Glycosaminoglycan. 41, 168

HPC High Performance Computer. 67, 71

Hyalinisation The formation of hyalin, a glassy material which is created in cells. 40

Hypercholesterolemia The presence of high levels of cholesterol in the blood. 40

Hypertension High blood pressure defined as a systolic/diastolic pressure persistently above 140/90 mmHg. 19, 40, 47, 54

IBM Immersed Boundary Method. 164–166

IcoA Intercostal Artery. 118, 119, 121, 124

IFM Immersed Finite Element. 165

IMA Inferior Mesenteric Artery. 84

InoA Innominate Artery. 20, 22, 117, 118, 141, 170, 171

ISPM Immersed Structural Potential Method. 166

LCCA Left Common Carotid Artery. 84–87, 118, 119, 125, 171

LCoA Left Coronary Artery. 117–119, 121, 125, 141, 143, 170, 171

LPN Lumped Parameter Network. 30, 64, 65, 71, 80, 83, 125, 126

LSCA Left Subclavian Artery. 84, 118, 119, 125, 141, 142, 170, 173

Mean Pressure The average value of pressure over the entire cardiac cycle. 22, 102–104, 106–117, 128, 135, 138–140

MMP Matrix Metalloprotease. 39, 135

MP Mean Pressure. 22, 102–104, 106–117, 128, 135, 138–140

MRI Magnetic Resonance Imaging. 32, 43, 44, 46, 47, 58, 73, 77, 94, 96, 147, 156, 160, 161, 169, 172

NURBS Non-Uniform Rational Basis Spline. 57, 58

ODE Ordinary Differential Equation. 81

PC-MRI Phase Contrast MRI. 14, 16, 19, 25, 65, 90–94, 96, 125, 151, 152, 160

PInoA Proximal to the InoA. 117–119, 125, 142, 143

PP Pulse Pressure. 22, 103, 106, 108, 110, 113, 114, 117, 134, 138, 139, 168

PPr peak-to-peak range. 128–130

Pulse Pressure The peek to peek value of pressure between systole and diastole. 22, 103, 106, 108, 110, 113, 114, 117, 134, 138, 139, 168

PV Pressure-Volume. 94–96, 135

PWV Pulse Wave Velocity. 20, 168

RCCA Right Common Carotid Artery. 84

RCR Resistor-Capacitor-Resistor. 22, 29, 32, 33, 71, 72, 81, 83, 84, 126, 127, 146, 157, 158, 175

Resistor-Capacitor-Resistor The three element [windkessel](#) model consisting of a resistor, representing the characteristic impedance of the vessel, connected in series with a grounded RC (resistor and capacitor in parallel) representing the impedance and compliance of the distal vasculature. [22](#), [29](#), [32](#), [33](#), [71](#), [72](#), [81](#), [83](#), [84](#), [126](#), [127](#), [146](#), [157](#), [158](#), [175](#)

RSCA Right Subclavian Artery. [84](#)

SMA Superior Mesenteric Artery. [84–87](#)

SMC Smooth Muscle Cell. [24](#), [39](#), [40](#), [168](#)

STL STereoLithography. [176](#)

SUPG Streamline Upwind Petrov-Galerkin. [62](#)

Syncope A temporary loss of consciousness and muscle function, also known as fainting. [44](#)

TAAD Type A Aortic Dissection. [23](#), [27](#), [41](#), [42](#), [44](#), [45](#), [51](#), [73](#), [121](#), [124](#), [141](#), [156](#)

TAWSS Time Averaged Wall Shear Stress. [23](#), [88](#)

TBAD Type B Aortic Dissection. [23](#), [27](#), [30](#), [31](#), [41–43](#), [46](#), [51](#), [54](#), [73](#), [102](#), [121](#), [124](#), [137–140](#), [156](#)

TEVAR Thoracic Endovascular Aortic Repair. [140](#)

TGF- β transforming growth factor- β . [41](#)

Time Averaged Wall Shear Stress The mean [Wall Shear Stress \(WSS\)](#) experienced over the cardiac cycle.. [23](#), [88](#)

TL True Lumen. [15](#), [27](#), [29](#), [30](#), [36–38](#), [44–46](#), [48](#), [50](#), [51](#), [54](#), [57–59](#), [69](#), [72](#), [78](#), [80](#), [84](#), [85](#), [88](#), [90–93](#), [96](#), [98–100](#), [102–118](#), [121](#), [123–125](#), [127–130](#), [132](#), [133](#), [135](#), [137](#), [138](#),

140, 143, 144, 147, 151, 152, 155–157, 160, 162, 166, 172, 173, 180

TSGP Transluminal Stent Graft Placement. 42, 45

TTE Transthoracic Echocardiography. 44

Tunica Adventitia The outer most layer of the vessel wall consisting of blood vessels and connective tissue. 25

Tunica Intima The thin inner most layer of the vessel wall consisting of endothelial cells. 25, 36, 40, 45

Tunica Media The thick layer in the middle of the vessel wall. Primarily made up of connective tissue and Smooth Muscle Cells (SMCs). 25, 36, 37, 39, 40

Type A Aortic Dissection A dissection involving the ascending aorta using the Stanford classification. The equivalent on the DeBakey classification is a Type I (involving the ascending aorta only) or Type II (involving the ascending and descending aorta). These dissections are typically treated as medical emergencies requiring immediate open surgical repair upon presentation. 23, 27, 41, 42, 44, 45, 51, 73, 121, 124, 141, 156

Type B Aortic Dissection A dissection involving the ascending aorta using the Stanford classification. The equivalent DeBakey classification is a Type I (involving the ascending aorta only) or Type II (involving the ascending and descending aorta). These dissections are typically treated as medical emergencies requiring immediate open surgical repair upon presentation. 23, 27, 30, 31, 41–43, 46, 51, 54, 73, 102, 121, 124, 137–140, 156

Vasa Vasorum The network of small blood vessels present in the walls of larger vessel walls which supply blood to larger arteries and veins. 40

Velocity Encoding [PC-MRI](#) is sensitive to a limited range of velocities. This range is set by the velocity encoding.. [19](#), [25](#), [90](#), [92](#), [152](#), [153](#), [160](#)

VENC [Velocity Encoding](#). [19](#), [25](#), [90](#), [92](#), [152](#), [153](#), [160](#)

Vessel Wall The vessel wall is made up of [intima](#), [media](#) and [adventitia](#). In cases of [Aortic Dissection \(AD\)](#) a defect in the intima propagates along the vessel, separating the intima and parts of the media from the vessel creating a false lumen. [24](#), [36](#), [39–41](#), [47](#), [59](#)

Windkessel model Electric circuit analogues of the vasculature where vascular resistance and compliance may be represented by resistors and capacitors and fluid inertia may be represented by inductors. Such systems can be studied using circuit analysis. There are many designs, perhaps the most common being the 3 element RCR [[122](#), [154](#)]. [23](#), [29](#), [62–64](#), [71](#), [81](#), [84](#), [93](#), [126](#), [134](#), [138](#), [157](#), [160](#)

WSS [Wall Shear Stress](#). [23](#), [28](#), [30](#), [83](#), [86](#), [87](#), [89](#), [135](#)

1

INTRODUCTION

This chapter will provide an overview of the project and its aims, the primary disease this work is concerned with, aortic dissection, and will introduce the four main studies which will be undertaken in this thesis.

Contents

1.1	Overview	2
1.2	Primary patient specific study	4
1.3	Computational Study of Anatomical Risk Factors	6
1.4	Strain quantification via dual phase black blood MRI	7
1.5	Impact of septum distensibility on simulated haemodynamics using a LPN	7
1.6	Thesis structure	8

1.1 Overview

Aortic Dissection (AD) was first reported over 200 years ago and it remains a disease with a high associated mortality rate. It is characterised by a tearing of the aortic wall resulting in a delamination of the wall and creation of a septum (or intimal flap) separating a **True Lumen (TL)** (which includes the original intimal layer) and a **False Lumen (FL)** (created between the intimal and medial layers of the vessel) through which blood flows and is exchanged between the two lumina via communicating tears. As shall be discussed in more detail in Chapter 2, the pathogenesis is still not fully understood, the disease has a complex etiology, and diagnosis is often difficult. There remains debate about the best way to treat **AD** patients.

Patients with what is termed acute **ADs** are treated as medical emergencies, and undergo immediate surgical intervention. This is the case if, for example, the **AD** involves the ascending aorta (a **Type A Aortic Dissection (TAAD)**) or results in side organ ischemia. However, as with all surgeries, such intervention carries an element of risk, and, if the **AD** involves the descending aorta only (a **Type B Aortic Dissection (TBAD)**), there is no significant ischemia evident, and if the **AD** is deemed to be stable, clinicians may opt to avoid surgery and treat the **AD** pharmacologically. Such cases are termed chronic **ADs**. However independent of the treatment the primary aims remain the same, to stabilise the **FL**, reducing pulse and mean pressure in the **FL** and ideally promoting full thrombus formation throughout the **FL** [56, 136, 53, 100].

Regardless of the treatment, complexity or classification of dissection, patients have a poor long-term prognosis with 50% mortality at five years [142]. The majority of deaths occur due to adverse haemodynamics in the **FL** leading to aortic expansion, growth of the **AD** and rupture. Current anatomical predictors of adverse outcomes include initial aortic size, patent (or partially thrombosed) **FL**, and diseases which cause degradation

of connective tissues such as Marfan syndrome. Such anatomical predictors of poor outcomes are used to customise follow-up strategies and optimise treatment planning. However, due to the specific conditions experienced as a result of each individual AD patient's geometry, physiological indices such as intra-aortic haemodynamics (pressure and flow) may, in fact, provide improved patient-specific predictors of outcomes.

Modelling allows for the numerical simulation of haemodynamic conditions in the vasculature. Given a faithful three dimensional geometry and carefully tuned boundary conditions, [Computational Fluid Dynamics \(CFD\)](#) can be used to determine patient specific haemodynamics and has the advantage of allowing quantification of pressure throughout a domain without the necessity of invasive procedures (such as pressure catheters), allowing calculation of velocity information potentially more accurate than can be acquired with patient imaging methods such as [4D PC-MRI](#), and allows for accurate determination of fields such as [Wall Shear Stress \(WSS\)](#) which cannot be measured *in vivo*. It has been hypothesised that high pressure in the [FL](#) may lead to propagation of the dissection, while high velocities in the [FL](#), which lead to high [WSS](#), may impede thrombus formation [[142](#), [141](#), [140](#)].

The primary aim of the work presented in this thesis is to add insight into the complex haemodynamics of [AD](#) via the use a variety of modelling tools. To this end, a number of novel studies have been designed.

1.2 Primary patient specific study: Multi-modality image-based computational analysis of haemodynamics in aortic dissection

A number of studies [71, 120, 69, 16, 70, 144, 68, 72, 15, 73, 2] have shown that analysis of blood flow through patient specific geometries using CFD can yield significant insight into the complex haemodynamics present in AD patients which may be difficult or impossible to quantify with other means. For example, in a longitudinal study involving an AD patient with image data acquired pre- and post-aneurysmal development, Tse et al. [144] investigated the influence that the aneurysm has on haemodynamics. A similar study can be found in Karmonik et al. [74]. Karmonik also investigated how flow and pressure patterns in the vicinity of the AD are affected when either the entry tear or exit tear are occluded [69], haemodynamic changes pre- and post-Endovascular Aortic Repair (EVAR) [68], as well as a comparison between haemodynamics in a healthy subject and those in a patient with AD [73]. Rudenick et al. [117] performed a combined experimental and computational study using an idealised phantom of an AD, comparing measured and simulated flows in both the TL and FL, showing good agreement. In Chen et al. [15], the haemodynamics of an AD patient were studied in a model that included primary entry and exit tears, as well as a secondary tear. Lastly, Alimohammadi et al. [2] performed a study in a simpler dissection model using coupled Resistor-Capacitor-Resistor (RCR) Windkessel models at the outlet branches.

Secondary intimal tears in the dissection flap are thought to occur due to avulsion around branching vessels as the dissection propagates [157]. Studies have found that patients with AD generally present with more than two tears [115, 78]. However, as will be shown, tears may be difficult to identify in the medical image data, due to the small size and

potential motion artefacts in the septum. In this study, we used a combination of two imaging modalities, [Computed X-Ray Tomography Angiography \(CTA\)](#) and [4D PC-MRI](#), to try to detect the location of these secondary tears.

For the presentation of this study the haemodynamic impact of different [AD](#) morphometric parameters is examined by conducting the following three novel investigations:

1. An analysis of the haemodynamic changes introduced by the dissection septum in the descending aorta. Here, a comparison of haemodynamic predictions was made between a multi-branched, multi-scale model of [AD](#) and a baseline healthy aortic model created by virtually removing the septum. This approach enables us to investigate specific changes in blood flow, pressure, [WSS](#), etc. directly attributable to the [AD](#).
2. An estimation of the additional stroke work imposed by the [AD](#) on the heart using a tuned [Lumped Parameter Network \(LPN\)](#) heart model.
3. A quantification of the impact of the often ignored secondary tears on [AD](#) haemodynamics. These tears, typically found in the vicinity of visceral branches, are difficult to visualise due to limitations in the image resolution and motion artefacts. In this investigation, three different [AD](#) models with varying number of tears were examined. The results demonstrate that while these tears may be difficult to image, they can, if present, have a significant influence on the haemodynamics.

In all previous studies on [AD](#) haemodynamics, a validation of numerical predictions against *in vivo* imaging data is lacking. We aim to address this by using rich medical imaging data ([Computed X-Ray Tomography \(CT\)](#), [2D PC-MRI](#) and [4D PC-MRI](#)) to inform our simulation and validate our results, comparing simulated and measured flows in several [TL](#) and [FL](#) locations in the descending aorta of a patient with an acute [TBAD](#). The work has been published [27].

1.3 Computational study of anatomical risk factors in idealised models of TBAD

There are numerous TBAD morphologies and anatomical predictors of long-term complications, however, the mechanisms behind aortic growth are poorly understood. Clinical and experimental studies have identified anatomical risk factors of aortic expansion such as FL location and orientation relative to the aortic curvature, number and size of intimal tears, tear patency and location, and FL patency [7, 39, 38, 117, 142, 140]. Studies have shown that the absence or occlusion of a distal tear leads to elevated pressures, FL partial thrombosis and aortic growth [142, 1, 141]. FL haemodynamics seem to play an important role in the aneurysmal complications, but they are difficult to measure clinically and the numerous factors determining FL haemodynamics make it problematic to perform systematic comparisons between AD patients [7, 117, 142, 141].

The aim of this study was to perform, for the first time, a systematic study of haemodynamic alterations associated with morphological predictors of aortic growth using CFD in a series of idealised Computer Aided Design (CAD) models of TBAD. The models were based on anatomical dimensions. Each model examined the effect of varying a single predictor. By varying each predictor in such a controlled manner it is possible to quantify and compare which predictors lead to less favourable haemodynamic conditions. The work presented here has been submitted for publication [6].

1.4 Strain quantification via dual phase black blood MRI in healthy and aortic dissection subjects

Although AD itself adds a separate dimension, the complexity of the aorta as an organ should not be forgotten. The movement of the aorta during the cardiac cycle, the changes in its diameter, area, length and volume are remarkable. The addition of such motions upon a fragile intimal flap must not be taken lightly [147, 98].

The aetiology of AD is multifactorial and unfavourable loading conditions have been hypothesised to aid in the propagation of AD. Fractures where the cyclical stress acts in a plane normal to the crack edge between the intima and media (a mode I type fracture) cause peeling [127, 49]. Direct measurement of these stresses remains impractical *in vivo*, but the strains generated can be quantified via the use of medical imaging and measurement of the deformations of the vasculature throughout the cardiac cycle.

The aim of this study is to use imaging techniques, specifically a form of Magnetic Resonance Imaging (MRI) imaging known as black-blood MRI, to acquire high quality 3D images of the aorta at systole and diastole and use them to measure aortic strain in both healthy subjects and in cases of AD. Strains were measured at the same material points in three-dimensions in systole and diastole in a so called Lagrangian approach. The work presented in this thesis is under review for publication [26].

1.5 Impact of septum distensibility on simulated haemodynamics using a LPN

The results of the 3D CFD simulation in section 4.1 will show that while tuning of the RCR boundary conditions applied at each outlet allowed for a close match of mean flows

between the patient specific 2D PC-MRI and simulated data, there existed a mismatch between the peak-to-peak range from the minimum to maximum value in the flow wave. It was believed that this may be due to a limitation of the CFD method in which a rigid wall assumption was adopted and the relatively large distensibility of the septum and the aorta itself was not accounted for, and the only compliance in the system was applied via the capacitor elements in each of the 0D RCRs at the outlets.

Following from work done by Rudenick et al. [117, 119], a study was devised to use a 0D representation of the 3D AD geometry with the hope of recovering the peak to peak flow in each of the lumina. This simple model, while not capable of reproducing the complex flow fields seen in the AD, particularly around the septum tears, does allow for the adjustment of the compliance of each of the lumina. An attempt was made to replicate the measured flows from both the 3D simulation and 2D PC-MRI data by varying the stiffness of the lumina which in turn could explain the mismatch between the flow wave forms of the 3D simulation.

1.6 Thesis structure

The structure of the remainder of this thesis is as follows: Chapter 2 discusses the clinical background of AD, highlighting the complex haemodynamics and etiology of the disease motivating this research, as well as providing a brief overview of AD classification, and the treatment and management strategies which may be employed. Chapter 3 provides the methods employed for each individual study. In Chapter 4 the results from the above-mentioned studies are presented. Chapter 5 contains the interpretation and discussion of the results. The conclusions of these studies is presented in Chapter 6 along with a summary of the limitations of the methods utilised. Chapter 7 details suggestions on how this work might lead to future research and address some of these limitations. Lastly,

Chapter 8 summarises a number of other projects undertaken during this research which are either yet to be completed, or do not fall under the scope of AD.

2

MOTIVATION

This chapter will examine the clinical background of aortic dissection, looking at the history of the disease, its pathogenesis, etiology, diagnosis and clinical management and will introduce the concepts this thesis will address.

Contents

2.1	Clinical Background	11
2.1.1	Pathogenesis	11
2.1.2	Etiology	12
2.1.3	Classification	16
2.1.4	Diagnosis	19
2.1.5	Management	19
2.1.6	Follow up	21
2.1.7	Summary	23

2.1 Clinical Background

AD is characterised by the delamination of the vessel wall resulting in the separation of the lumen and creation of a TL and FL [118]. The earliest recorded death from AD dates to October 25th 1760. It was on the morning of this date that the 76 year old King of England, King George II, retired to the royal toilet. Soon after his valet de chambre, a German by the name of Schröder, heard a noise that he described as louder than the royal wind. Upon investigating he found the King lying dead on the floor with a large cut on his face. A little over a month later, the Royal Surgeon, Dr Frank Nicholls, reported on the autopsy of the body, recording that the pericardium was distended and filled with a pint of blood, a hole in the right ventricle large enough to allow the doctor to fit his finger into, and a transverse fissure an inch and a half long on the inside of the aorta [56, 136, 53, 100].

Today, more than 200 years later, AD is still seen as a morbid event, and despite recent improvements in management techniques, hospital mortality rates remain high [36, 118, 143]. Elective surgery has shown to have associated morbidity of between 0% and 27% and in the case of emergency surgery can have a morbidity of over 50% [75].

2.1.1 Pathogenesis

The pathogenesis of AD is still not fully understood, however it is believed that a tear in the intima is initiated allowing the media to be exposed to pulsatile blood flow. This can result in the formation of a longitudinal medial cleavage. It may also be caused by the development of a haematoma from a haemorrhage in the media leading to perforation of the intima [36]. From this initial formation a flap begins to grow and continues to propagate between the middle and outer two thirds of the media, causing the formation

of the TL and FL with communication between the two volumes via a single or multiple tears. The largest proximal tear is usually referred to as the entry tear while the largest distal tear as the exit tear [118, 77, 168] (see Figure 2.1).

The TL, due to pressure fluctuations, demonstrates expansion and forward flow during systole. During diastole the TL can collapse which may give rise to risk of ischemia of organs supplied by the local side branches. In the FL, flow can be seen to be delayed, absent or even reversed, depending on the geometry, configuration of the tears and the degree of communication between the TL and FL [36]. As the AD grows, multiple tears may be induced due to the propagation of the AD around side branches, especially around the abdominal vessels and the renal arteries [134, 133].

2.1.2 Etiology

AD has a complex etiology and may be induced by any mechanism that causes a weakening of the media [36, 168]. The disease more frequently affects men than women with ratios of 2:1 to 5:1 being quoted in the literature [77, 21]. Other than gender, there have been a number of predisposing factors which have been pointed to as possible causes of AD.

Genetic Predisposition

There are a number of genetic factors that have been linked to the development of AD, the most common being Marfan syndrome, Ehlers-Danlos syndrome, and annuloaortic ectasia and familial AD [103, 36, 168, 21]. While genetic predisposition has a lower incidence than other etiologies in terms of total ADs, they are seen as the greatest risk factor to patients younger than 40 years and have been identified as a clinical predictor of complications [56, 168, 21, 39].

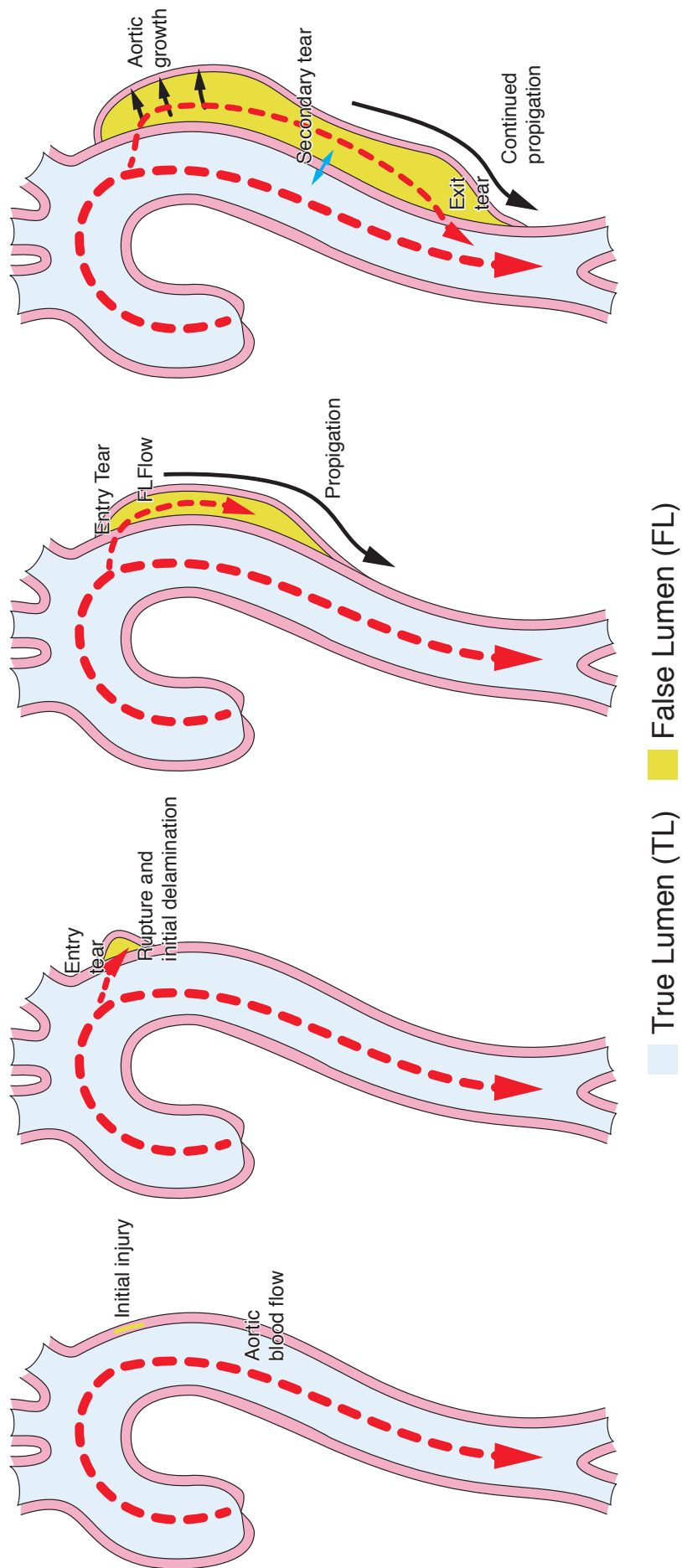


Figure 2.1: Motivation: AD pathogenesis While the pathogenesis of AD is not fully understood, it is thought that some damage to the intima of the aorta causes the initiation of a tear, exposing the media to pulsatile blood flow. This leads to a delamination of the vessel wall and creation of a TL and FL which can propagate along the vessel. Blood may be communicated between each of the lumina via a number of communicating tears (image adapted from [142]).

2.1.2.0.1 Marfan Syndrome

Marfan syndrome, the most common tissue disorder has a reported incidence of between 1/5000 to 1/10000 [103, 36, 80]. The disorder is characterised by mutations clustered around the fibrillin-1 gene, causing a deficit of fibrillin to be produced and affects the skin and dura matter and the skeletal, ocular, integumentary, pulmonary, and cardiovascular systems [103, 36, 134, 80]. The condition may lead to progressive weakness of the aortic wall due to deterioration of elastin in the media [103, 168, 134]. It is believed that Marfan syndrome causes an activated phenotype of Smooth Muscle Cells (SMCs) which may be initiated by the fragmentation of medial elastic layers and elastolysis caused by an enhanced expression of Matrix Metalloprotease (MMP) [103].

2.1.2.0.2 Ehlers-Danlos Syndrome

Ehlers-Danlos syndrome has a quoted incidence of 1/5000 [103] and is characterised by joint hypermobility, skin hyperextendability, and tissue fragility [103, 36]. This is due to mutations in the body's collagen, disrupting the α helix secondary structure of the collagen [158]. One of the 15 collagen types known to be affected by Ehlers-Danlos syndrome is Type I collagen found in vasculature [134, 158, 86]. The disrupted collagen fibrils have lower Young's moduli than expected, and ADs are therefore able to propagate at lower pressures [134].

2.1.2.0.3 Annuloaortic ectasia and Familial Aortic Dissection

Annuloaortic ectasia's effect on the aorta is similar to that of Marfan's syndrome. It is a proximal ascending aorta dilation which was first recognised by Ellis et al. in 1961 [35, 36]. In patients presenting with thoracic aortic aneurysms, at least five mutations of the FBN1 gene have been identified [103, 36].

Hypertension

Hypertension is one of the most prevalent conditions in patients presenting with AD and is seen as the most important risk factor with figures of 70% to 80% of AD coupled with hypertension being quoted in the literature [133, 39, 126, 95]. Half of ADs for women aged 40 years or younger occur during pregnancy, and of those 25% to 50% also present with hypertension [77].

Patients presenting with AD coupled with hypertension have a higher frequency of distal dissection rather than proximal [95]. It is thought that extra cellular fatty acid deposition, calcification, fibrosis and intimal thickening as well as parallel degeneration, apoptosis and elastolysis with hyalinisation of collagen accelerates extracellular matrix degeneration. Both mechanisms, caused by hypertension, lead to aortic ulcers and atherosclerosis [103, 77]. It is believed that this leads to disruption of the vasa vasorum, decreasing blood supply to the media and causing necrosis of the SMCs [36, 134]. Hypertension may eventually lead the formation of an intramural hematoma, remodelling of the aortic wall and aortic dilation and eventually to intimal rupture due to increased hoop stress in the aortic wall (where hoop stress for a cylinder (σ_{Θ}) is the product of pressure (P) and vessel radius (r) divided by vessel wall thickness (t), i.e. $\sigma_{\Theta} = (P \times r)/t$) [36, 77, 134, 21].

Smoking, hypercholesterolemia, and consumption of benzoylmethylecgonine (cocaine) are seen as additional risk factors [103, 36, 77].

Iatrogenic Factors

Iatrogenic AD due to insults of the aortic wall caused by surgical repair or examination such as catheter intervention or valvular surgery is cited as a cause for AD [103].

Deceleration Trauma

Deceleration trauma, such as car accidents or falls from height, have also been linked to AD [36, 77, 24].

Glycosaminoglycans

Glycosaminoglycans (GAGs) have been postulated as a possible cause of the development and progression of AD. GAGs are long unbranching polysaccharides which contribute to the compressive rather than tensile stiffness of soft tissues as they retain a high degree of water content due to their high negative charge [25]. What has been suggested is that overexpression of GAGs by transforming growth factor- β (TGF- β) could cause intarlamalar swelling pressures which exceed the normal compressive stress in the aortic wall, and may therefore lead to delamination of the aortic wall [25].

2.1.3 Classification

There are a number of different classifications for AD, the most common being the De Bakey and the Stanford classifications. ADs may also be classified as acute or chronic, and complicated or uncomplicated ADs. The Stanford classification subdivides ADs into those involving the ascending aorta, TAAD, and those that do not, TBAD. The De Bakey classification, established by Dr Michael Ellis De Bakey who pioneered the present day gold standard surgical intervention technique for TAAD, further divided the classification into those that involve the ascending and descending aorta (Type I), those that involve only the ascending aorta (Type II) and those that involve only the descending aorta only (Type III) (see Figure 2.2) [103, 36, 77, 21, 88]. Due to the variety of differing geometries of AD, a number of other classification schemes have been proposed, however these have

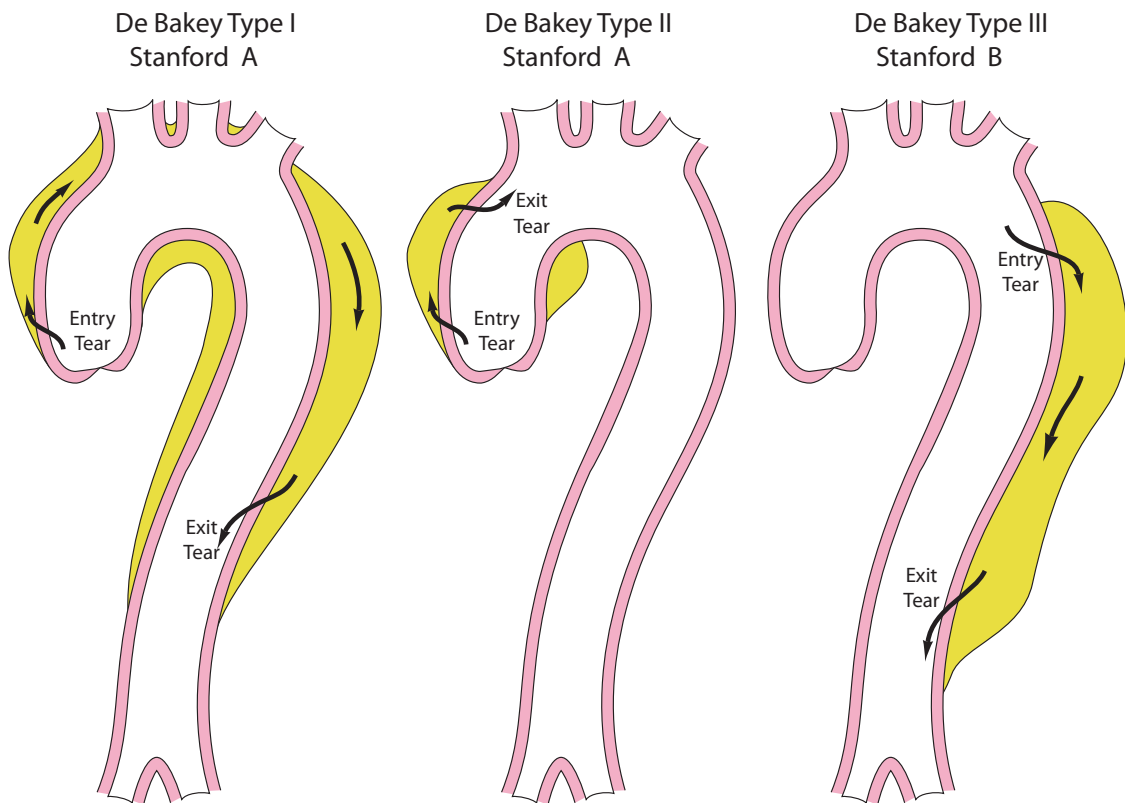


Figure 2.2: AD classification The various common forms of classification for AD with a FL (shown here as yellow) single primary entry tear and single exit tear (note, in a true AD there may exist only a single entry tear, or there may be multiple secondary tears along the length of the septum). The Stanford TAAD includes any dissection which involves the ascending aorta while TBAD includes any type that does not involve the ascending aorta. Under the De Bakey classification, ADs that involve the entire aorta are classified as Type I, those which involve the ascending aorta alone are classified Type II, while those involving the descending aorta alone are classified Type III. A number of other classification schemes have been proposed which have yet to receive wide acceptance. Image adapted from [36].

yet to receive wider acceptance [103, 36].

Chronic ADs are those treated pharmacologically with no surgical intervention for longer than a two week period, whereas acute ADs refer to those treated immediately either by open vascular surgery or a Transluminal Stent Graft Placement (TSGP) [77, 93, 55, 67]. Approximately 33% of ADs are classified as chronic and are almost exclusively limited to the ADs involving the descending aorta (TBAD) [93].

Complicated ADs are those presenting with ischemia due to malperfusion of arteries with branching roots originating in the FL and TAAD due to added risk of occluding coronary or carotid vessels [103, 21, 67, 131]. Complicated ADs require urgent care to

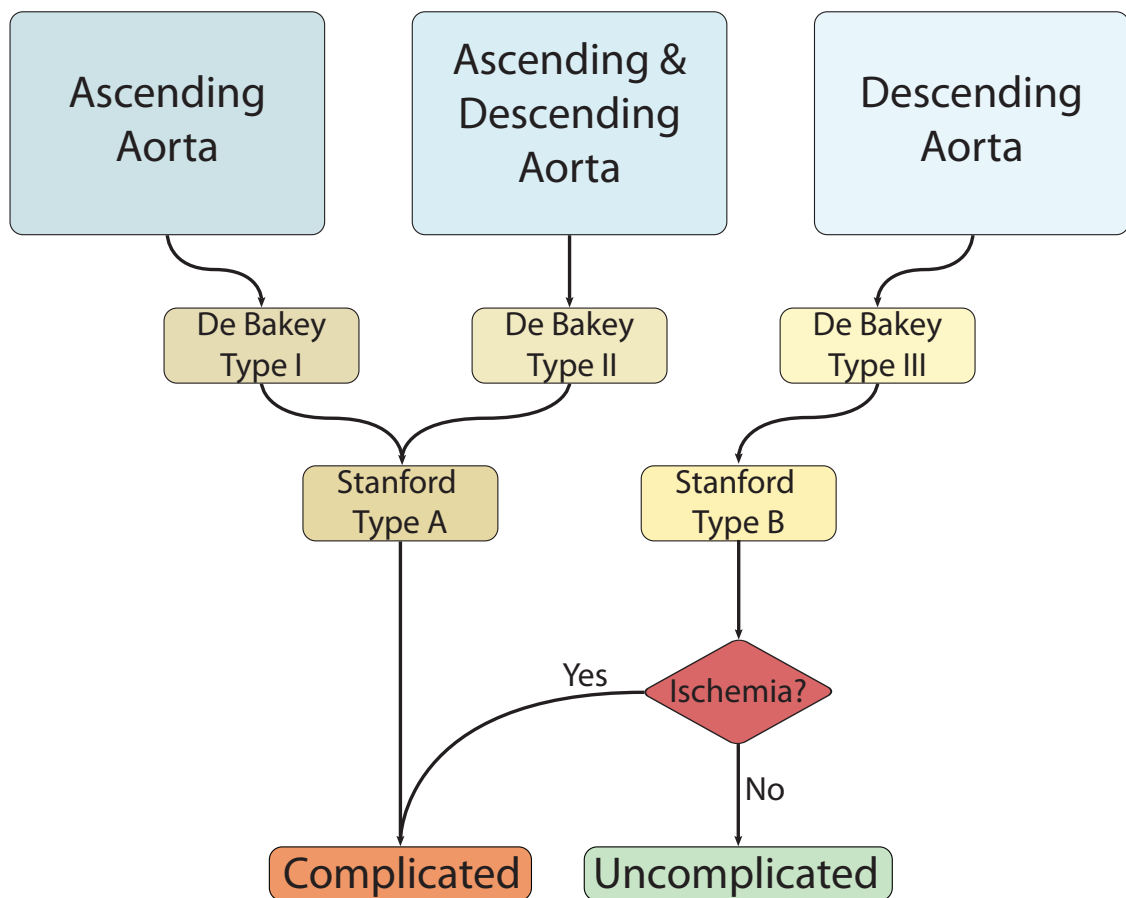


Figure 2.3: AD classification flowchart This flow chart breaks down how ADs are classified depending on whether they include the ascending aorta or not, and whether ischaemia is present. Complicated ADs are routinely treated as emergencies upon presentation. Uncomplicated dissections may be stable for months or even years with antihypertensive treatment alone.

restore perfusion, with a mortality of 20% at day 2, and 25% to 50% in 28 days [21, 131].

Uncomplicated TBADs can be treated pharmacologically and perform relatively well in the short term, with survival rates of around 90% within a month and between 75% and 90% within one year [103, 77, 21, 131]. They do however require frequent follow up and re-examination with MRI or CT, CT generally providing better diagnostic imaging but also imparting ionising radiation to the patient. Associated long-term mortality outcomes are relatively poor with 30% to 50% mortality at 5 years [21, 102].

2.1.4 Diagnosis

Typically, a patient with **AD** will present with severe back or chest pain. Malperfusion due to the **FL** causing obstruction of side branches results in limb ischemia and pulse defects. **Syncope** may be experienced. After the initial onset of chest pain, cardiac failure due to aortic regurgitation may pervade particularly with **TAAD**, however it is common for symptoms to be vague and nonspecific [103, 93].

It is therefore critical to use imaging techniques to diagnose and classify the dissection, and on average two different techniques are used to diagnose **AD**. The main modalities considered are **CTA**, **MRI**, angiography, and **Transthoracic Echocardiography (TTE)** [103, 36]. The choice of imaging technique tends to depend on the experience of the clinicians dealing with the patient and the equipment available [36].

The principal aims when imaging dissection are confirmation of the **TL** and **FL**, the size of the **FL**, and the location of entry and exit tears. Contrast imaging or Doppler ultrasound may also be used to characterise flow through the **FL**, identifying the potential for thrombus formation and possible malperfusion due to low flow, as well as identifying the risk of retrograde or antegrade propagation of the **FL** [103, 36].

Presently there are no biomarkers which are capable of indicating **AD**, however research into markers such as D-Dimers (typically used to detect thrombosis formation) and increased levels of **C-reactive protein (CRP)** (typically used to detect inflammation) are showing some potential [103, 36, 126].

2.1.5 Management

It is critical that correct assessment of the condition of the **AD** is made in order to determine the best course of treatment, however the ideal strategy for treating **AD** remains

an area of debate [88, 55, 153, 20].

Open Surgical Repair

If the AD is complicated, i.e. if ischemia is evident, or if the AD is of TAAD (De Bakey Type I or II) classification, either open surgery or TSGP is usually opted for [34].

There is a high mortality associated with surgery due not only to the preoperative state of the aorta, but also due to the typically older age of such patients who often have other underlying conditions [81]. The main goals of open surgical repair involve restoring the TL flow, however the best method to do so remains unclear [21, 88, 40]. A number of options exist, but essentially follow the procedure described by De Bakey i.e. the replacement of the aorta involving the intimal tear with a prosthetic graft, resecting the tear and restoring TL flow, and excluding the primary proximal intimal tear and therefore inducing thrombosis formation [21, 24, 93, 131]. When dealing with a TAAD, aortic valve replacement may also be necessary [131, 40, 121].

Endovascular Treatment

In recent years, TSGP has come to be seen as an alternative to open surgical repair, and especially applicable to those who may be at high risk due to age or secondary conditions [40]. The first stent graft replacements were performed in the 1990's, and it has become more widely accepted since that time [10]. The primary aim of TSGPs is to occlude the proximal intimal tear and thereby both reduce pressure in the FL and reduce the risk of rupture, and also decrease blood flow into the FL and induce thrombus formation, ultimately close the FL and restore flow to the TL [133, 131, 153, 114, 89]. Since the first TSGP repair was performed, studies have shown favourable results, with success rates between 77% and 100% [10, 114]. However, full thrombosis is rarely seen especially when

the dissection is relatively long [114].

Pharmacological

Pharmacological treatment is reserved for those patients who exhibit uncomplicated, **TBAD** (De Bakey Type III **AD**) with low risk of rapid progression [36, 153]. Typically **antihypertensive** treatments, beta blockers and morphine sulphate are used to try and maintain normal blood pressure and thereby reduce risk of further propagation of the **FL**, aortic growth and rupture [36, 21, 93, 102, 34], the ultimate goal of such treatment being the creation of full thrombus in the **FL**, a seen as a favourable outcome for **AD** patients as it both stabilises the **FL** and restores blood flow to the **TL** [142]. Pharmacological treatment is seen as the preferential course of action due to the high mortality rates associated with surgery, with mortality rates for uncomplicated **AD** of 35% to 50% as opposed to 10% with medical intervention after one month [21, 34]. Over time, the **FL** may exhibit endothelialisation and calcification, adding to the complexity of the disease [85, 156].

2.1.6 Follow up

AD demands constant follow up and monitoring irrespective of the treatment pursued [36]. **MRI** is frequently recommended for monitoring of stable **ADs** [36, 57]. The advantages of **MRI** are numerous: it does not impart any energy into the body, it is considered to be much safer than X-rays and **CTA** scans, and the images obtained can be of a relatively high resolution. Also the fact that scans can be layered means that a three dimensional view of the inside of the body can be obtained, allowing the portions of the body to be viewed from any angle, as well as allowing the identification of landmarks to align successive scans and track the growth of the **FL** [36, 13, 105]. The use of blood pool agents

can be used to improve the accuracy of scans and 4D PC-MRI flow data describing the blood velocities can be acquired [20, 19]. CTA however is recommended in emergency situations as scan times are usually faster and image quality can be better than that acquired with MRI, allowing for better identification and quantification of small features [36, 57], and is the most common method of imaging AD [36].

Survival remains an area of concern, and despite improvements of between 4% and 9%, long term overall survival rates of between 50% to 80% after five years and 30% to 60% after ten years remain [39]. Those undergoing medical intervention have an associated survival rate of 50% to 70% after five years [21]. This suggests that management and monitoring strategies remain dissatisfactory and there is a necessity to better understand how FL expansion and morbidity are related [143, 21]. It has been observed that growth rates of the dissection are strongly correlated with risk of negative events, with 24% chance associated with a growth rate of 0.05 cm/year as opposed to 45% with a growth rate of 0.2 cm/year [21].

It has been theorised that significant flexional forces between the mobile heart and ascending aorta and the relatively fixed descending aorta which is tethered to the spinal column may be a significant contributor to the development of AD [77, 21].

Another issue which may complicate prognosis are the variety of conditions that can initiate the development of an AD. These differing etiologies have very different biological effects, for example Marfan Syndrome may cause the degeneration of the vessel walls with blood pressure remaining at normal levels, while hypertension leads to stiffer vessels and increased pressure.

2.1.7 Summary

AD has a complex etiology and poor prognosis. It therefore represents a disease that warrants further study and investigation. For chronic AD patients, it is currently the norm for clinicians to monitor the size and progression of the dissection post-diagnosis [118], as discussed previously. It is known that haemodynamics plays an important role in the development of cardiovascular diseases such as AD and AD can lead to dramatically altered haemodynamics and elastodynamics in the aorta. Blood flow can be communicated via either lumen, different branching vessels may be supplied mainly via the TL or FL, pressure in the FL may be significantly above normal physiological levels and the creation of the AD creates a thin septum flap which can undergo significant deformation throughout the cardiac cycle.

Furthermore, patients who may, on first examination, appear to have similar geometries can have vastly different outcomes. Thrombus formation is associated with lower blood velocity [19]. Depending on the velocity of blood in the FL some patients may exhibit patent FL relatively thrombus free. Others may experience full FL thrombus, restoring blood flow to the TL and stabilising the AD. A final group of AD patients can experience partial thrombus formation. This group is of particular concern being associated with a 2.7 fold increase in risk of a morbid event due to the AD (see figure 2.4) [142]. This increase may be due to the thrombus occluding distal tears and creating a blind-sac, resulting in a dramatic increase in FL pressure and increased risk of aortic growth and may lead to eventual FL rupture [142]. It is therefore clear that haemodynamics play an important role in the outcome of AD patients, velocity being key in the development of FL thrombus, and pressure key to the risk of growth or rupture of the FL. These haemodynamics are unique for each patient and are dependent on each patient's specific cardiac performance, structural properties of the vasculature and geometry of AD.

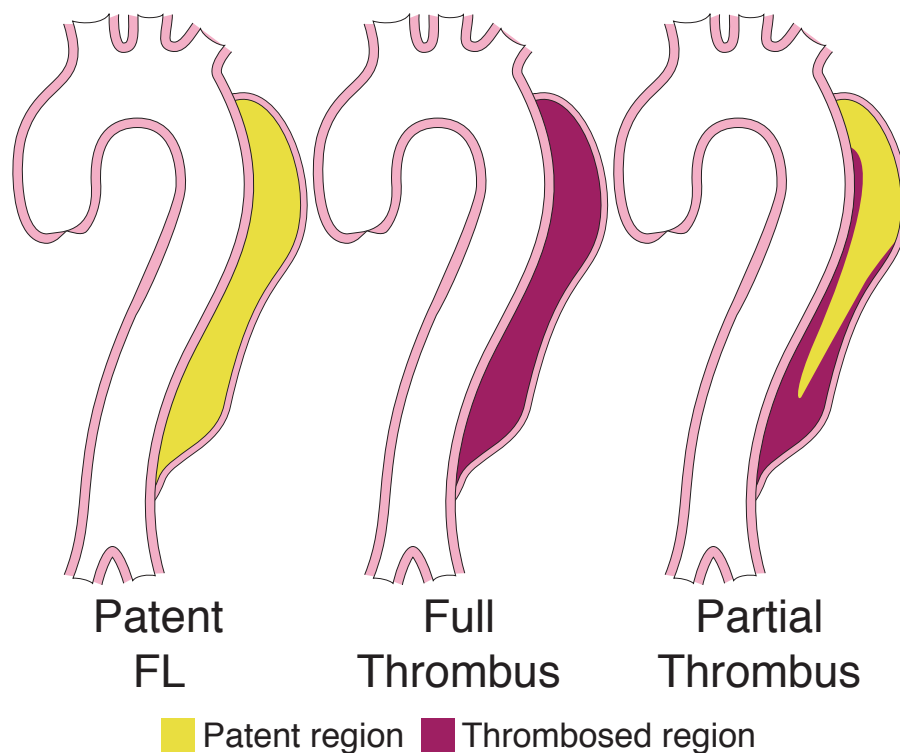


Figure 2.4: Motivation: AD thrombus configuration. Patients who, on first examination, have relatively similar geometries can have wildly different outcomes. There may be no thrombus formation in the FL (*left*), full thrombogenesis (*centre*) or partial thrombogenesis (*right*). AD patients in this last group are associated with a 2.7 fold increase in the risk of a morbid event due to their AD due to increased risk of aortic growth and FL rupture. Both FL thrombogenesis, being associated with reduced blood velocity [19], and aortic growth, experienced due to high pressure in the FL, are dependant on FL haemodynamics. Better knowledge of how FL geometry affects these haemodynamics could lead to better patient risk stratification in the future (image adapted from [142]).

There have been many studies examining how the geometry of the AD may influence the local haemodynamics and as such correlate the progression of the AD with the degree of altered haemodynamics. Through phantom studies it has been found that communication between the TL and FL through secondary tears at locations other than the proximal and distal tears may be a major contributor to complete collapse of the TL during diastole [143, 133]. Weiss et al. in their study on tear size and location found that patients who presented with tears on the concave side of the aortic arch (i.e. the inner circumference) were at higher risk of development of a complicated dissection and postulated that the geometry of the dissection leads to less favourable haemodynamics, in particular due to local changes in the pressure gradient [153]. Tam et al. in their animal study found evidence for a linear relationship between the depth of the initial tear and the pressure required for the propagation of the AD [134]. *In vitro* studies also suggest that larger tears may lead to TL collapse, increasing the risk of organ ischemia [115].

In vitro studies have investigated how the size and presence of entry and exit tears influences the AD haemodynamics [118, 143], finding that large entry and exit tears lead to pressure equalisation between the TL and FL. These studies also found that in the absence of an entry or exit tear pressure will increase in the FL with larger increases seen when there is no exit tear.

For follow up, AD patients generally undergo some form of imaging and a clinician assesses the risk of an undesirable event based on certain indicators such as geometry of the FL relative to the aortic arch, patency of connecting tears, thrombus formation or growth of the AD [7, 39, 38, 117, 142, 140]. These predictors are based on historical observation in a clinical setting and debate remains as to how each of these predictors leads to poorer outcomes. Interpretation of the image data and determination of the best course of treatment is based largely on the clinicians experience and skill in interpreting

the image data. It is hoped the work presented in this thesis will go some way to informing patient stratification and potentially lead to improved methods of diagnosis and treatment planning for AD.

AD represents a significantly challenging disease. The creation of a FL connected to a TL via a number of tears leads to altered haemodynamics unique to each AD patient. Low velocities are associated with thrombus formation, which can stabilise the FL but may also occlude distal tears or side branches and may cause large increases in FL pressure. The FL wall is weaker than the undissected wall, and is therefore susceptible to aortic growth leading to potential rupture which can be a particular concern when the FL experiences high pressures. The FL may also be susceptible to propagation in both the proximal and distal direction along the aorta or into branching vessels. Finally, the onset of AD leads to the creation of a distensible intimal flap with variable structural properties and thickness along its length (Figure 2.5).

This thesis attempts to use a variety of modelling tools and data analyses to address each of these issues. As TAADs are typically treated as medical emergencies with immediate surgical intervention upon presentation, these analyses will be restricted to those ADs which involve the descending aorta only, TBADs, which may be managed for months or even years with pharmacological intervention. It is hoped that the work presented here may lead to a greater understanding of the haemodynamics and mechanics involved in the dissected aorta, and may allow a better insight of the clinical predictors used presently for AD patients, the strains the septum flap undergoes during the cardiac cycle, the impact the AD has on haemodynamics and workload relative to the undissected state, and it is hoped that this may ultimately lead to the development of a workflow to perform systematic CFD analysis for this complex and challenging disease.

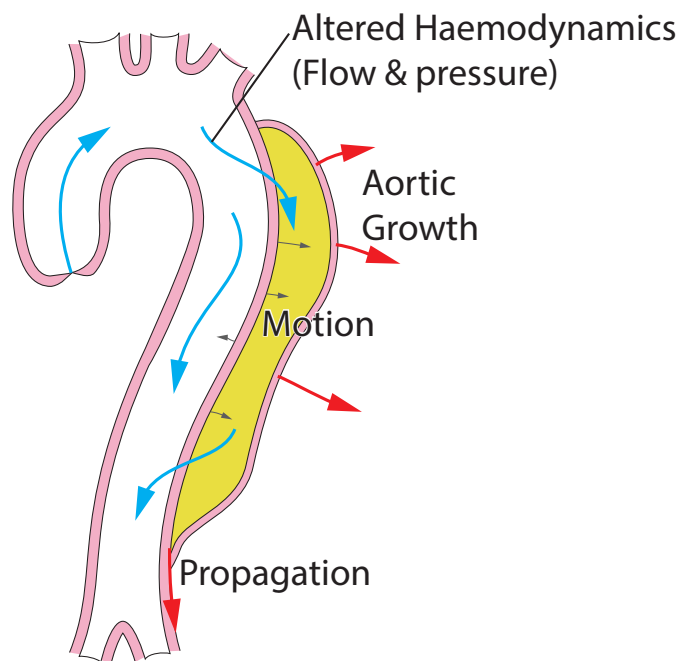


Figure 2.5: Motivation: AD mechanics. When considering the problem of modelling of ADs, there are a number of mechanical complexities which do not exist with the healthy aorta. Firstly, the creation of a new blood flow channel in the FL can lead to significantly altered haemodynamics. Depending on the specific configuration, the FL may experience relatively low velocities which may allow the creation of thrombus, stabilising the FL. Conversely, high pressures can exist and may lead to aortic expansion, a particular concern as the wall of the FL is weakened relative to the undissected aorta and excessive growth may result in FL rupture. The FL is also susceptible to propagation at its leading edge. Finally, the creation of an intimal flap means that there exists a thin, highly distensible structure immersed in the AD flow.

3

METHODS

The methods chapter will discuss in detail data acquisition, the segmentation approach for production of 3D CAD models, the methodology involving the creation of idealised models to study AD, the approach used to study strain in healthy and dissected aortas, and the modelling with 0D analogues of 3D domains.

Contents

3.1	Primary patient specific study	29
3.1.1	Patient Details	29
3.1.2	Imaging	29
3.1.3	Computational fluid dynamics	36
3.2	Computational study of anatomical risk factors	44
3.3	Strain quantification via dual phase black blood MRI	48
3.3.1	Image acquisition	48
3.3.2	Strain Measurements	49
3.3.3	Image analysis	51
3.3.4	Image segmentation	52
3.3.5	Dimensional measures and strain calculations	53
3.4	Impact of septum distensibility on simulated haemodynamics using a LPN	55

3.1 Primary patient specific study: multi-modality image-based computational analysis of haemodynamics in aortic dissection, a patient specific study

3.1.1 Patient Details

A 49-year-old male subject presented with an acute **TBAD** originating 5 mm distal of the left subclavian artery, extending the full length of the descending aorta and terminating 5 mm distal to the left iliac bifurcation. The long axis of the dissection septum progressively rotated approximately 90° clockwise along the length of the descending thoracic aorta, bisecting it largely in the sagittal plane in the abdominal region. A number of vessels branched from the **FL** (left renal artery, inferior mesenteric artery and medial sacral artery), while the remaining branched from the **TL**. It should also be noted that several vessels in the coeliac trunk region (coeliac trunk, superior mesenteric artery) had, due to their proximity to the **AD** flap, a significantly pinched appearance at the branching location from the aorta, resulting in an oval cross-section with the short axis aligned with the transverse plane.

The patient was previously prescribed **antihypertensive** drugs (Amlodipine 10 mg, Candesartan 4 mg) to treat a history of **hypertension** pre the **AD** event. On presentation, the patient was administered additional intravenous antihypertensive medication to acutely control blood pressure.

3.1.2 Imaging

A number of different image datasets were acquired for the patient.

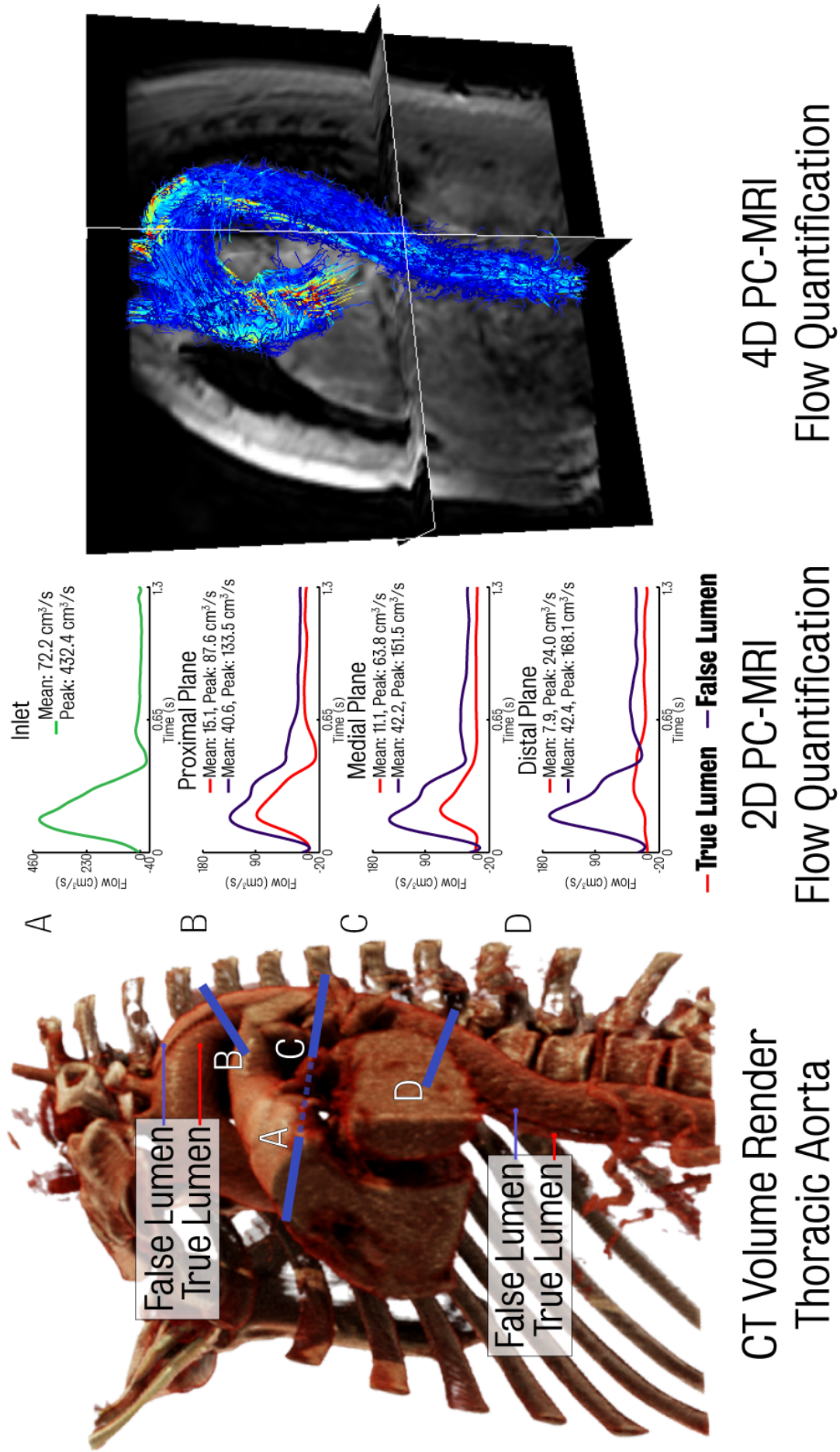


Figure 3.1: Primary patient specific study: Available image data *Left CTA* volume render of the thoracic aorta illustrating the AD septum. *Centre 2D PC-MRI* data at aortic inflow and several locations down the aorta. *Right full aorta 4D PC-MRI* data.

Table 3.1: Primary patient specific study: Scan settings for both thoracic and abdominal CTA scans of an AD subject

Property	Thoracic	Abdominal
FOV (Field of View)	376mm	280 mm
In plane resolution	512×512	512×512
Slice thickness	2 mm	0.9 mm
Tilt	0°	0°
Tube Voltage (KPA)	412 mA	221 mA
Acquisition	Cephalocaudal	Cephalocaudal

Anatomy: CT Data

The patient was scanned within 24 hours of presentation. A 40-row multi-slice scanner (Brilliance 40; Philips Medical Systems, Cleveland, Ohio) was used to image the full aorta in two separate scans acquired using first-pass bolus-tracked contrast-enhanced images during one breath hold: one capturing the thoracic aorta and the second the abdominal aorta (see Figures 3.1, 3.2); 100 mL of iohexol contrast agent (Omnipaque 350; GE Healthcare, Oslo, Norway) was delivered at 4 ml/s using a power injector (Medrad Spectris, Siemens Medical Solutions, Malvern, Pennsylvania). The scan was automatically triggered when the contrast enhancement reached 150 HU. Settings for both the thoracic and abdominal scans are listed in Table 3.1.

Flow data: PC-MRI

In this work, 2D PC-MRI data were used to quantify blood flow at four different locations in the aorta, while 4D PC-MRI data were used to perform a qualitative comparison between imaging and CFD-derived velocity fields. All image data were collected using the methods presented in Clough et al. [20] and are summarised here for completeness.

A thirty-two element coil Achieva 3T scanner (Philips Healthcare, Best, the Netherlands) was used to acquire the images. Image reconstruction was performed using a Philips scanner console and commercially available software [8, 90, 50].

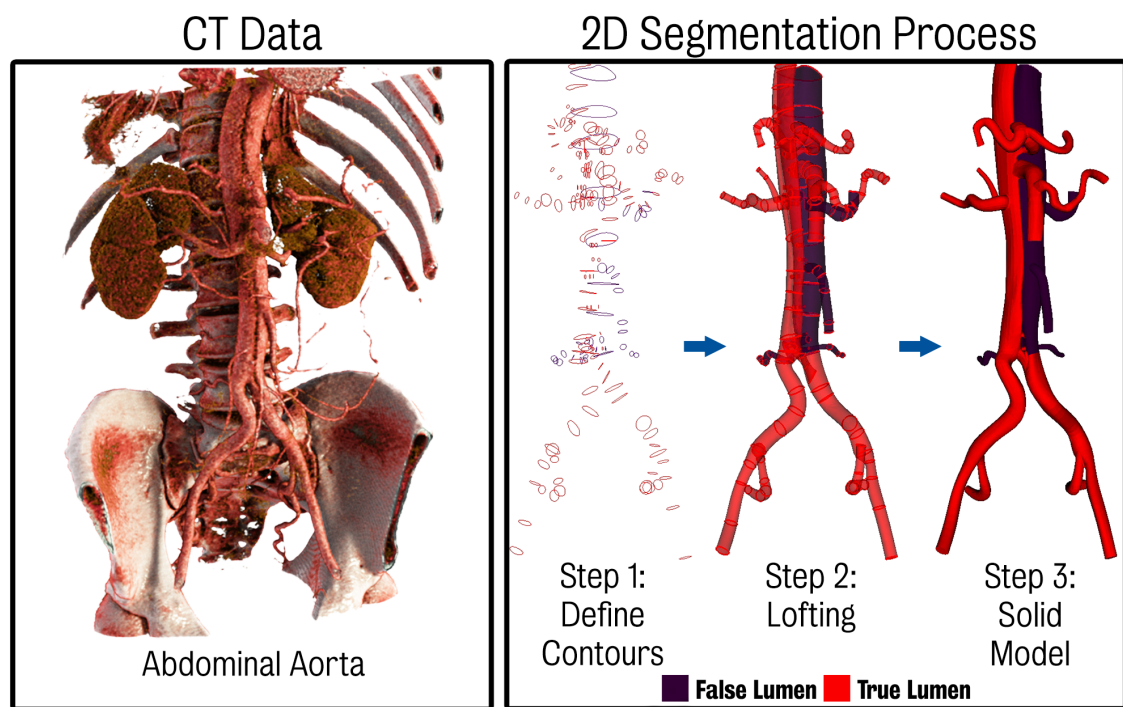


Figure 3.2: Primary patient specific study: Abdominal CT data and AD segmentation process *Left* CTA showing the anatomy of the dissection in the abdominal aorta. The small size and motion of the septum make it difficult to clearly delineate the TL and FL. *Right* 3D solid model creation process using a 2D segmentation approach. In step 1, contours of the lumina are created. These contours are then lofted together (step 2) to create a Non-Uniform Rational Basis Spline Non-Uniform Rational Basis Spline (NURBS) analytical representation of each vessel. Finally, (step 3) the lofted surfaces are joined and blending operations using fixed radius fillets are employed to remove sharp edges between branching vessels. The FL and vessels perfused from the FL are coloured in *purple*, while all other vessels are coloured in *red*.

Table 3.2: Primary patient specific study: Scan settings for 2D PC-MRI scans of an AD subject.

Property	Value
FOV (Field of View)	350×350 mm ²
Voxel size	1.74×1.99 mm ²
Slice thickness	10 mm
Velocity Encoding (VENC)	150 cm s ⁻¹
TR/TE	5.0/3.0 ms
Temporal resolution	52 ms
Number of signal averages	2

Flow-encoded through-plane images were acquired at three positions perpendicular to the longitudinal axis of the aorta. These locations included the ascending aorta just distal to the aortic valve (this plane also acquired flow in the descending aorta at the level of the T-4 vertebra), the descending aorta, 15mm distal to the left subclavian and the descending aorta at the level of the T-7 vertebra. The position of these planes is noted in blue in Figure 3.1. Electrocardiogram (ECG)-gated data were later allotted to 25 cardiac phases (details given in Table 3.2).

Stroke volume and heart rate were found to be 94 ml and heart rate 47 Beats per Minute (BPM), respectively. This corresponds to a cardiac output of 4.4 L min⁻¹. Velocity data were processed using the multi-dimensional MRI phase-contrast flow visualisation program, GTFlow (GyroTools LLC).

Geometric modelling

In order to create a geometric CAD model, the 2D segmentation paradigm originally introduced in Wang et al. [151] was utilised. Paths were defined through roughly the centreline of the vessels to be later included in the model. Then, a 2D segmentation operation (which can be performed automatically or manually) along the paths was performed at a number of discrete locations. This 2D segmentation step provides the contours of TL and FL of the AD. Lastly, lofted surfaces are obtained using NURBS to

produce an analytical and smooth solid model that can then be meshed. The right panel of Figure 3.2 depicts the various steps of this segmentation approach. The FL and vessels perfused from the FL are coloured in purple, while all other vessels including the TL are coloured in red.

Several models were created using this methodology. A baseline dissected model containing the primary entry and exit tears as well as 15 secondary connecting tears were generated from the CTA data. Most of these secondary tears were located in the visceral region. These tears generally form in regions where the septum separates from the wall in the vicinity of a branching vessel, and are believed to be the remnants of the original entry to the branching vessel [157]. A large number of connecting tears may be observed near the coeliac trunk, renal artery, etc. [134, 94, 133]. The size of the main entry and exit tears was 135 and 68 mm², respectively. This corresponds to equivalent diameters of 13 and 9.3 mm, respectively. From this baseline dissected model, an undissected model was created by virtually removing the septum from the dissected model and keeping the outer boundary of its contours, thereby assuming that there are no significant changes in diameter between dissected and undissected models. Both dissected and undissected models have dimensions within the normal anatomical range. The undissected model is therefore representative of a healthy aorta and will be used to investigate the acute haemodynamic changes introduced by the dissection. Both these models are shown in Figure 3.3. Furthermore, to address the difficulty in detecting connecting tears between the lumina, and to investigate their potential impact on the haemodynamics, two additional AD models featuring different numbers of secondary connecting tears were also created. These models will be discussed in more detail in Section 4.1

The models created in this study are arguably the most complex and geometrically sophisticated AD models to date. Many previous studies of AD did not include the branching

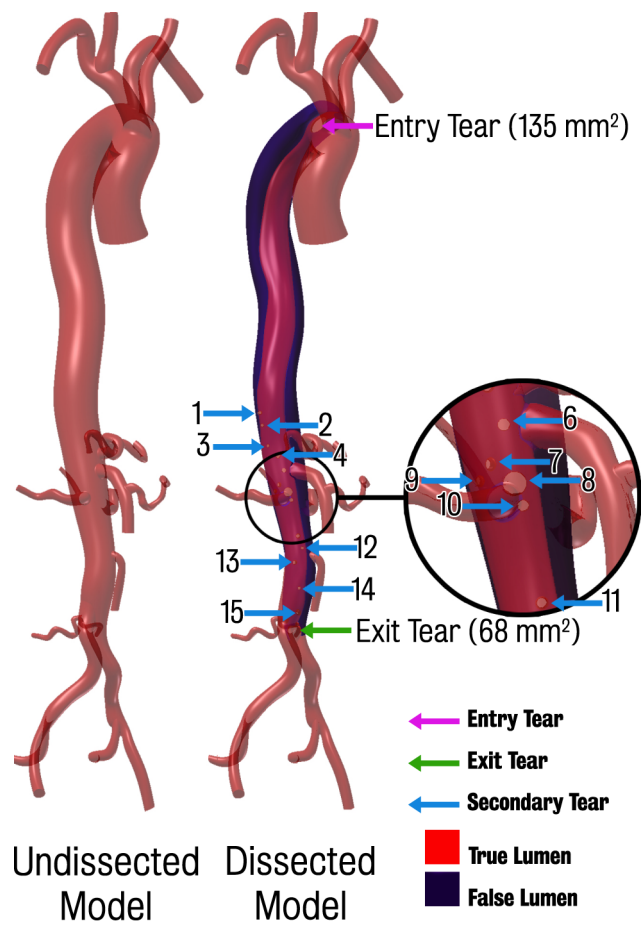


Figure 3.3: Primary patient specific study: Undissected and dissected models *Highlighted* are the entry tear, exit tear and 15 secondary tears.

vessels around the coeliac trunk region [71, 70, 2]. It has however been noted that in the vicinity of branches there exists highly complex flow fields which may have a significant influence on perfusion [124, 144]. Therefore, the models presented here were constructed to preserve as much of the branching vasculature thought necessary for accurate modelling, resulting in 17 outlets in total, including upper branch vessels (left and right subclavian and carotid arteries), visceral vessels (coeliac trunk, superior mesenteric, inferior mesenteric, left and right renal arteries) and iliac vessels (left and right internal and external iliac).

3.1.3 Computational fluid dynamics

Coupled multi-domain method for blood flow simulation

In this section, the coupled multi-domain method for blood flow simulation used for the study is presented. This method uses a stabilised **Finite Element (FE)** formulation to solve the incompressible Navier-Stokes equations in a 3D rigid domain reconstructed from image data, coupled to simpler, reduced order models of the circulation at the inlet and outlet boundaries of the computational domain. It therefore represents a multi-scale (or multi-resolution) approach to blood flow modelling, as flow and pressure are calculated over the entire circulation and not just the image-based 3D portion [150]. The strong form of the Navier Stokes equations in the domain $\Omega \in \mathbb{R}^3$ with the boundary $\Gamma = \partial\Omega = \overline{\Gamma_g} \cup \overline{\Gamma_n}$, $\Gamma_g \cap \Gamma_n = \emptyset$, $\Gamma \in \mathbb{R}^3$ with a time domain $t \in [0, T]$ can be given as

$$\begin{aligned}
 \rho \dot{\mathbf{v}} + \rho \mathbf{v} \cdot \nabla \mathbf{v} &= -\nabla p + \nabla \cdot \boldsymbol{\tau}, (\mathbf{v}, p, \mathbf{x}, t) \in \Omega \times [0, T] \\
 \nabla \cdot \mathbf{v} &= 0, (\mathbf{v}, p, \mathbf{x}, t) \in \Omega \times [0, T] \\
 \mathbf{v} &= \mathbf{g}, (\mathbf{v}, p, \mathbf{x}, t) \in \Gamma_g \times [0, T] \\
 \mathbf{t}_n = \boldsymbol{\sigma} \mathbf{n} &= [-p\mathbf{I} + \boldsymbol{\tau}]\mathbf{n} = \mathbf{h}, (\mathbf{v}, p, \mathbf{x}, t) \in \Gamma_n \times [0, T]
 \end{aligned} \tag{3.1}$$

where ρ is the blood density (set at 1.06 g ml^{-1} for each simulation), \mathbf{v} and p represent the blood velocity and pressure and $\boldsymbol{\tau} = \mu(\nabla\mathbf{v} + (\nabla\mathbf{v})^T)$ is the viscous stress tensor of a Newtonian fluid, where μ is the blood viscosity (set to $4 \times 10^{-3} \text{ Pa s}$). Body forces are set to zero.

Considering appropriate function spaces \mathcal{S} , \mathcal{W} and \mathcal{P} , one can obtain the following weak form of the problem:

$$\begin{aligned} & \int_{\Omega} \{ \mathbf{w} \cdot (\rho \dot{\mathbf{v}} + \rho \mathbf{v} \cdot \nabla \mathbf{v}) + \nabla \mathbf{w} : (-p \mathbf{I} + \boldsymbol{\tau}) - \nabla q \cdot \mathbf{v} \} dV \\ & + \int_{\Gamma_g} q \mathbf{v} \cdot \mathbf{n} dA - \int_{\Gamma_n} \mathbf{w} \cdot \mathbf{t}^h dA + \int_{\Gamma_n} q \mathbf{v} \cdot \mathbf{n} dA + Stab = 0 \end{aligned} \quad (3.2)$$

$$\forall \mathbf{x} \in \Omega, \forall t \in [0, T]$$

where $\mathbf{w} \in \mathcal{W}$ and $q \in \mathcal{P}$ are the weighting functions for the momentum and mass conservation equations, respectively. $u \in \mathcal{S}$ are the trial functions for the velocity field. g is the imposed velocity at Γ_g , and h is a traction prescribed via the 3D-0D domain interface coupling conditions on Γ_n . Figure 3.4 shows a schematic of the boundary conditions utilised in this work. The term *Stab* refers to the stabilisation terms of the [Streamline Upwind Petrov-Galerkin \(SUPG\)](#) formulation [155] utilised in our in-house software CRIMSON [42]. The stabilisation terms are necessary as the code uses linear P1+P1 shape functions for both velocity and pressure, yielding a solution susceptible to spurious oscillations when the advective velocity term dominates. To overcome these oscillations, the [SUPG](#) method adds an amount of artificial diffusion in the direction of flow only [29].

A three-element [Windkessel](#) model was coupled to the outlet face of each of the branches. In this model, the distal vasculature (small arteries and arterioles) is represented via a 0D electric circuit analogue that uses resistors to represent haemodynamic resistance and capacitors to capture the vessel compliance [46, 154, 149]. This simple model is one of

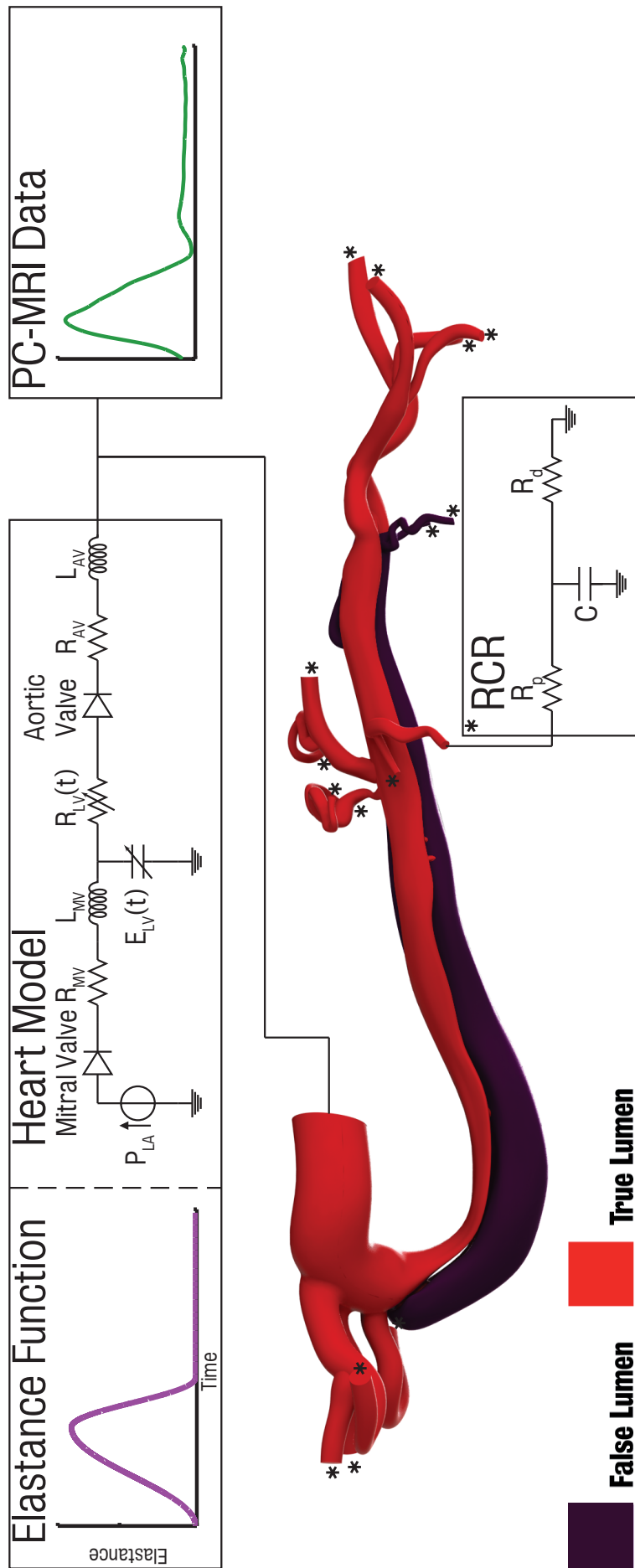


Figure 3.4: Primary investigation: Boundary conditions Schematic showing inlet and outlet boundary conditions used in this work. A three-element Windkessel lumped-parameter model was specified on each outlet face of the arterial model. Inflow conditions were prescribed from either 2D PC-MRI data or via a lumped-parameter heart model. Tuning the elastance function the heart model allows for a close match with the measured 2D PC-MRI flow data

the most commonly used approaches for outflow boundary condition specification in the simulation of haemodynamics [130, 1, 165]. Realistic flow and pressure waveforms are achieved via proper specification of the model parameters. The three-element [Windkessel](#) model relates flow Q and mean pressure via

$$\begin{bmatrix} P_C - P_d \\ P_p - P_C \\ Q_C \\ Q \end{bmatrix} = \begin{bmatrix} R_d Q_d \\ R_p Q_p \\ C \left(\frac{d(P_C - P_{C_g})}{dt} \right) \\ Q_p + Q_d - Q_C \end{bmatrix}$$

where C is the compliance of the distal vasculature, R_p and R_d are the proximal and distal resistances, respectively, P_p and P_d are the proximal and distal reference pressure (ground value in the [Windkessel](#) model), P_C and P_{C_g} are the [Windkessel](#) mid and ground-pressures (note $\frac{P_{C_g}}{dt} = 0$ if P_{C_g} is constant) and Q_d is the flows across the distal resistor while Q_p is the flow across the proximal resistor and is equivalent to the flow between the 3D-0D interface domain. When conditions are cyclical, the mean value of $Q_C = 0$. Stabilisation at the 3D-0D interface is provided by a flux term on outflow/inflow boundary of the 3D domain on an element-by-element basis as described in Hughes and Wells [63]. Boundary condition coupling was implemented in the context of the variational multi-scale approach of the multi-domain method [150, 37]. In this approach, the relationship between the upstream 3D domain and downstream 0D domain is enforced via a Dirichlet to Neumann operator which is computed from the current state of the [LPN](#) at the boundary and can be thought of as defining a relationship between pressure and flow rather than prescribing them at each boundary. These operators are assembled into the discrete matrix system. This system is then solved iteratively until adequate convergence for the coupled problem is achieved (typically 4-6 non-linear iterations per time step).

For cardiovascular modelling, in both the 0D and 3D domains events occur on relatively similar time scales, therefore stiffness is not an issue.

Regarding the inflow conditions, two different approaches were adopted:

1. An inflow waveform was prescribed at the inlet face of the model. The waveform was derived from the [2D PC-MRI](#) data measured just distally to the aortic valve and was mapped to a time-varying parabolic velocity profile.
2. A [LPN](#) model of the left side of the heart tuned to match the flow waveform reconstructed from [Phase Contrast MRI \(PC-MRI\)](#).

A number of reduced-order heart models have been previously proposed [[64](#), [109](#), [45](#), [76](#), [79](#)]. The one presented in this paper is an implementation of that developed by Lau and Figueroa [[82](#)]. This model consists of a constant pressure source (P_{LA}) representing the left atrium, a time-varying capacitor representing the left ventricular elastance ($E_{LV}(t)$) and diodes representing the mitral and aortic valves. The pressure in the left ventricle is calculated as a function of the elastance E_{LV} , left ventricular volume V_{LV} and the unstressed left ventricular volume $V_{u,LV}$,

$$P_{LV}(t) = E_{LV}(t)(V_{LV}(t) - V_{u,LV})$$

The model for the ventricular elastance $E_{LV}(t)$ is based upon trigonometric functions, as detailed in [[112](#)] and also includes a time-varying resistance R_{LV} that accounts for viscous pressure losses. This resistance is proportional to a constant k_{LV} , the left ventricular pressure P_{LV} and the left ventricular flow Q_{LV} :

$$R_{LV}(t) = k_{LV}P_{LV}Q_{LV}$$

The heart model was also the multi-domain method [150]. By tuning the parameters of the heart model, specifically the time to maximum elastance and the maximum elastance value, it is possible to adjust the resulting inflow wave form to produce the desired levels of peak and mean flow. Thus, this approach enables the reproduction a measured flow waveform without imposing it directly. In doing so, and by using standard values for the heart model published in the literature, we have a method that enables the estimation of cardiac workload, which will make it possible to estimate alterations in cardiac stroke work for this patient when changes in afterload resulting from the sudden onset of the dissection morphology occur [82].

Mesh generation

In blood flow modelling, velocity patterns, WSS and pressure gradients can be greatly affected by coarse meshes that ultimately render the blood unphysical due to numerical viscosity [135]. In this work, a two-step strategy was used for the finite element mesh generation. An initial mesh was created for each model using boundary layer and local curvature-based refinement. Simulations were run using the 2D PC-MRI flow data as inflow boundary conditions.

In order to reduce solution error due to low mesh resolution, adaptive meshing was applied. The adaptive meshing algorithm, based on work by Sahni et al. [123], reduces the number of elements in regions where the second derivatives of velocity field are low while introducing more elements in regions where the velocity second derivatives are large. Mesh adaptation is particularly advantageous when studying haemodynamics in complex geometrical domains. This approach allows a more uniform distribution of error in all directions. The final unstructured field-adapted meshes for each model ranged between 2.6 million tetrahedral elements and 0.4 million nodes in the undissected model to 13.2

million tetrahedral elements and 2.4 million nodes in the dissected model. Figure 3.5 shows an adapted mesh where large numbers of small elements are generated in regions with large Hessians of the velocity field. This is particularly evident in the region of many of the connecting tears.

Time integration strategy

The generalised- α method was used to advance the solution in time. This is a second-order accurate method which allows arbitrary user-defined numerical dissipation of unresolved high frequencies [66, 41]. This method was used due to its good stability properties. For this thesis, the spectral radius, $\rho_\infty = 0$. It can be shown that for this value the method is unconditionally stable for linear problems with this value. For a more detailed description of this method the reader is referred to the work of Jansen et al. [66] and Figueroa [41].

Analyses were run using between 2,600 and 10,400 time steps per cycle (time step size between 500 s and 125 μ s for a cardiac cycle of 1.3 s) on 256 cores of a 640 core SGI Altix-UV High Performance Computer (HPC) with Nehalem-EX architecture. Residual control, which limits the sum total of all the individual nodal residuals for the entire mesh, was set to 1×10^{-3} . Each cardiac cycle took approximately between 4 and 18 hours to run. For each case, simulations were run between 3 and 7 cardiac cycles until a cycle-to-cycle periodic solution in flow and pressures was achieved.

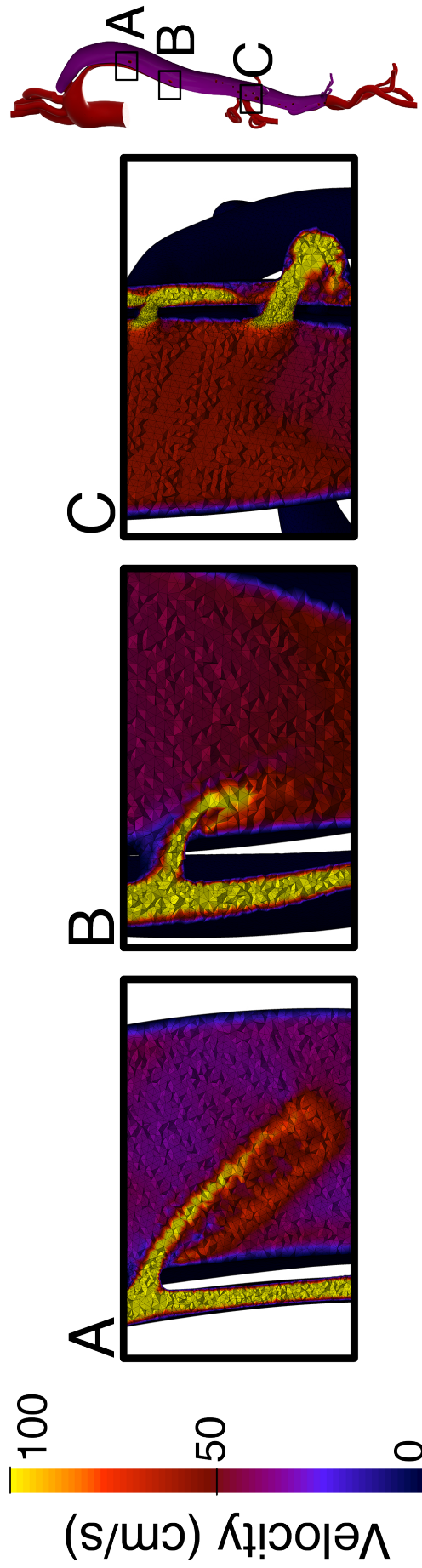


Figure 3.5: Primary patient specific study: Mesh adaptation The figure highlights areas of mesh refinement in regions where the second derivatives of velocity field are high, such as in the vicinity of narrow tears. The refined mesh allows for a more uniform distribution of error in all directions.

3.2 Computational study of anatomical risk factors in idealised models of TBAD

For this study a total of 16 idealised aortic CAD models were made, one representing a normal healthy aorta and fifteen AD models featuring a TL, a FL and a maximum of two connecting tears between the TL and FL. The models included variations in the shape of aortic curvature, FL position relative to the aortic curvature, and number, size and patency of tears relative to a baseline geometry (Figure 3.6). All models were built with TL and FL of consistent lengths and diameters. This approach enabled a controlled comparison among models, since only one geometrical factor was modified at a time. Total aortic length and diameter were 500 mm and 25 mm, respectively. The length of FL and TL was 250 mm and the hydraulic diameter $D_H = 4 \times A/P$ (where $A = \text{Area}$ and $P = \text{wetted perimeter}$) was 30 mm and 9.5 mm, respectively. The flap was designed as 1 mm thick. The stented model had larger TL (25 mm diameter) and narrower FL ($D_H = 15.6$ mm) in the first three quarters of the dissection, where the stent was placed. A graphical description of each model is summarised in Figure 3.6. The baseline model has three curvatures in the sagittal, transverse and coronal planes, mimicking a human aorta [7] and is based on the curvature described by Craiem et al. [22]. The candy-cane model has a single curvature along the axial direction. For the baseline and the candy-cane models the FL was arbitrarily placed at the outer curvature. The curved model has a semi-torus shape with a single 180° planar curvature. Models were created with the FL at both inner and outer sides of the arch. The majority of models had circular tears, with diameters of 4, 10 and 20 mm. A model was created with elliptical tears (large and small axes: 17 mm and 6 mm, respectively), rendering an equivalent cross-sectional area to a 10 mm circular tear. A non-dissected model was also created based on the shape of the baseline model. All models were created with Autodesk Inventor [4].

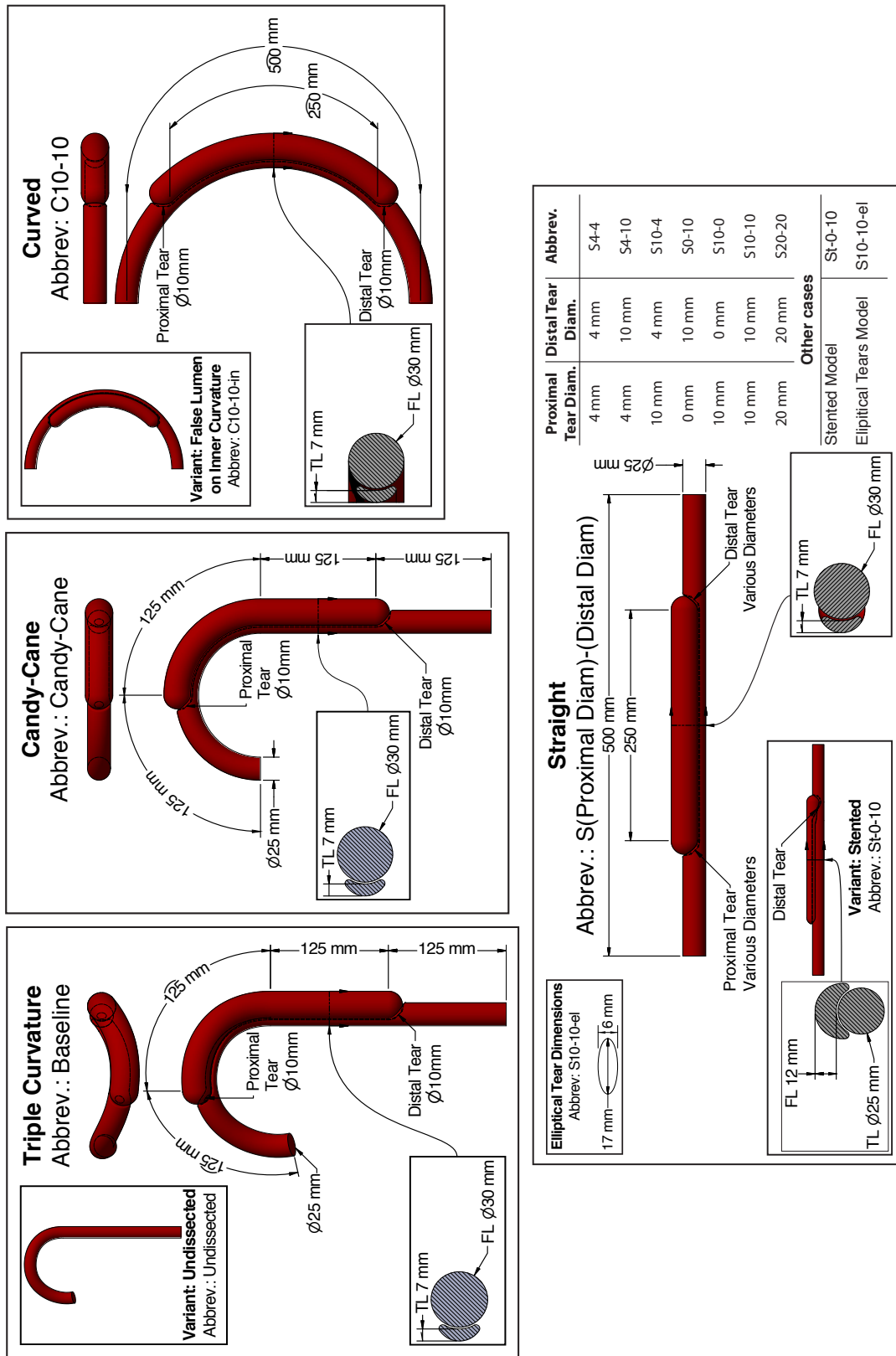


Figure 3.6: Anatomical Risk Factors in Idealised Models study: Idealised models schematic Schematic of the idealised AD models, including shape, FL location relative to the curvature, tear diameter, and abbreviated names. In clockwise order from *Top Left*, the models which will be examined are the triple curvature model, the candy-cane, the curved model, and the straight model. Variants of each model are also shown where applicable.

CFD analysis of haemodynamics was performed using CRIMSON [42] and the coupled multi-domain method as described in 3.1.3. Analyses were performed at the HPC Cluster in the University of Michigan. FE tetrahedral meshes were created and iteratively refined until mesh-independence in the results was reached. The mesh size ranged between 0.12×10^6 (*undissected* model) and 3.8×10^6 (*S4-4* model) elements. The vessel walls, including the flap were modelled as rigid. Blood was treated as a Newtonian and incompressible fluid with a dynamic viscosity of 4 mPa s and a density of 1.06 g ml^{-1} . All analyses were initialised with a global pressure value of 80 mmHg and velocity was set to zero throughout the domain. A pulsatile flow (mean 4 L min^{-1} , 46 BPM) was prescribed at the inlet and is a modified version of the flow wave form used for the AD patient of the primary patient specific study.

At each outlet, a pressure waveform was implicitly imposed by a three-element Windkessel RCR LPN model. To derive initial Windkessel parameters an approach based on that of Xiao et al. [164] was used. A first approximate value of total resistance for the entire domain was calculated from Equation 3.3 where \bar{P} and P_g represent the mean and distal ground pressure respectively and Q_{in} represents the total cardiac outflow. The sum total cross-sectional areas for all the outlets $A_{T_{out}}$ was calculated and the total resistance was distributed based on the ratio of each outlets cross-sectional area $A_{j_{out}}$ via Equation 3.4 (subscript j represents the vessel outlet). An initial ratio of proximal to distal resistance, $R_{j_p} : R_{j_d}$ was assumed to be 10 : 90 for each RCR.

$$R_T = \frac{\bar{P} - P_g}{Q_{in}} \quad (3.3)$$

$$R_j = R_T \frac{A_{j_{out}}}{A_{T_{out}}} \quad (3.4)$$

The initial value of total compliance $C_T = \frac{dV}{dP}$ of the system was estimated from the maximum ($Q_{max_{in}}$) and minimum ($Q_{min_{in}}$) cardiac outflow, the time between $Q_{max_{in}}$ and $Q_{min_{in}}$ (Δt) and the target systolic (P_S) and diastolic (P_D) aortic pressures via Equation 3.5. The compliance for each RCR was then distributed via Equation 3.6.

$$C_T = \frac{Q_{max} - Q_{min}}{P_s - P_d} \Delta t \quad (3.5)$$

$$C_i = C_T \frac{A_{j_{out}}}{A_{T_{out}}} \left(\frac{R_{j_p} + R_{j_d}}{R_{j_d}} \right) \quad (3.6)$$

Simulations were then run, analysed and compared to both the target data and typical flow and pressure waveforms [101]. The values of resistance, the ratio of resistances ($R_{j_p} : R_{j_d}$) and compliance were then individually tuned better match these data and simulations were rerun. This iterative process was repeated until simulations matched .

Once determined, boundary conditions remained constant for all cases. Simulations were run for several cardiac cycles until periodic solutions were achieved. The sum total of residual error for the entire mesh was limited to 1×10^{-3} . Only results obtained in the last cycle are reported.

For each model, pulse pressure, mean pressure and mean flow were measured at five different locations, namely inlet and outlet, and three dissection sites 120 mm apart from each other. We refer to these sites as prox. (5 mm downstream to the proximal tear), mid. (at the mid point of the dissection) and dist. (5 mm upstream of the distal tear). Furthermore, peak tear velocity was also measured as well as velocity in the middle of TL and FL.

Table 3.3: Strain quantification study: Subject details Subject 1-5 were volunteers. Subjects 6 and 7 were AD patients with a repaired acute TAAD and residual TBAD

Subject number	Age	Sex	Smoker	Clinical History
1	32	F	N	-
2	30	M	N	-
3	29	M	N	-
4	24	M	Y	-
5	23	F	Y	-
6	50y		Y	TAAD operated on with residual TBAD component.
7	42y		Y	TAAD operated on with residual TBAD component and suspected connective tissue disorder.

3.3 Strain quantification via dual phase black blood MRI in healthy and aortic dissection subjects

3.3.1 Image acquisition

Image acquisition in cardiovascular MRI generally occurs in diastole where there is less cardiac motion and blood flow related artefacts. For the purpose of this study, to evaluate aortic motion and changes during the cardiac cycle, images were obtained in systole and diastole.

Five healthy volunteers and two patients who had undergone repair of acute TAAD (but were left with a residual TBAD) were included in this study. Table 3.3 shows the demographics of the study population.

All subjects were scanned in the Achieva 3T scanner (Philips Healthcare, Best, The Netherlands) with a 32 element coil at the Rayne Institute, King's College London. All subjects provided written consent.

Imaging parameters at 3T for both systolic and diastolic sequences include: TR/TE A = 5.0/2.3 ms, acquisition duration = 100 ms, T₂prep echo time = 70ms, FOV = 264 × 380 × 46 mm³, Δx = 1.6 × 1.6 × 1.6 mm³, α = 20° for the first acquisition and 5°

for the PSIR reference acquisition, SENSE factor = 2 (anterior-posterior). A pencil beam navigator was used for respiratory gating, with a 5 mm gating window. A cine phase contrast scan was performed in order to determine the blood flow in the ascending aorta just distal to the aortic valve and to determine the ECG-trigger durations to obtain systolic and diastolic images. Data acquisition was performed in systole and diastole in all subjects (n=7). Images were reconstructed on the Philips scanner console using commercially available software.

3.3.2 Strain Measurements

Strain is the quantification of deformation of a material from a reference configuration to a new configuration when exposed to a force. The aorta, sometimes referred to as the 5th chamber of the heart, is a highly compliant vessel. During the normal cardiac cycle the aorta is subject not only to internal pressure forces causing cross-sectional strain, but also a longitudinal strain along the axis of the aorta due to the contraction of the heart [108, 47].

Arteries comprise of a complex composite material whose main structural passive components are elastin and collagen. Elastin is a particularly inert substance with a half life measured in years and undergoes substantial fatigue via the cyclical strains of normal cardiac function. Normal ageing leads to intimal thickening, lengthening of the aorta, particularly in the thoracic region, as well as increased tortuosity and stiffening [108, 22, 62, 125].

A number of studies have tried to quantify strain in the aorta using 2D imaging, typically using MRI [152, 60, 30, 62, 31, 99] and ultrasound [11, 65] measurements. Other studies have measured stress strain relationships *ex vivo* [145] but a limited number have tried to quantify the longitudinal and cross-sectional strain *in vivo*.

Muhs et al. [98] used dynamic cine-CT and measured the vessel maximum and minimal dimensions at a fixed distance from branching locations. Choi et al. [17] created segmentations based on 3D MRI to compute geometric deformations in the aorta which occur between foetal and supine positions. Morrison et al. [97] used 4D cardiac-gated CT data with the aim of quantifying longitudinal and circumferential strains and also measured vessel dimensions at branching locations.

The key difference between the work of Morrison et al. and Muhs et al. to other approaches is that deformations are calculated using a Lagrangian rather than Eulerian reference frame. Figure 3.7 describes the differences between these two methodologies highlighting the issues with Eulerian methods.

Methods which use a static 2D plane (Eulerian methods) disregard out of plane motions. However, it is known that the aorta can undergo significant longitudinal displacements, particularly at the aortic root [108, 47]. As such, quantities which are reported as strains by studies using such Eulerian methods may in fact be reporting normal changes in geometry, such as the result of tapering of the vessel along its length, or a disease such as an aneurysm or coarctation resulting in a sudden local change in the vessels cross-sectional area. Strain may therefore be under or over reported and the reliability of strain reported by such studies is questionable. Further, the portion of vessel wall observed in systole may have significantly different stiffness properties than the portion observed in diastole and may therefore exhibit very different behaviour in response to local stresses.

Lagrangian approaches rely on identifying material points which can be tracked regardless of the direction and degree of displacement and generally demand the acquisition of 3D image data. As material points remain fixed relative to the aorta throughout the cardiac cycle, such methods avoid issues such as changes in observed cross-sectional area or stiffness due to out of plane motion. Therefore only such methods can give an accurate

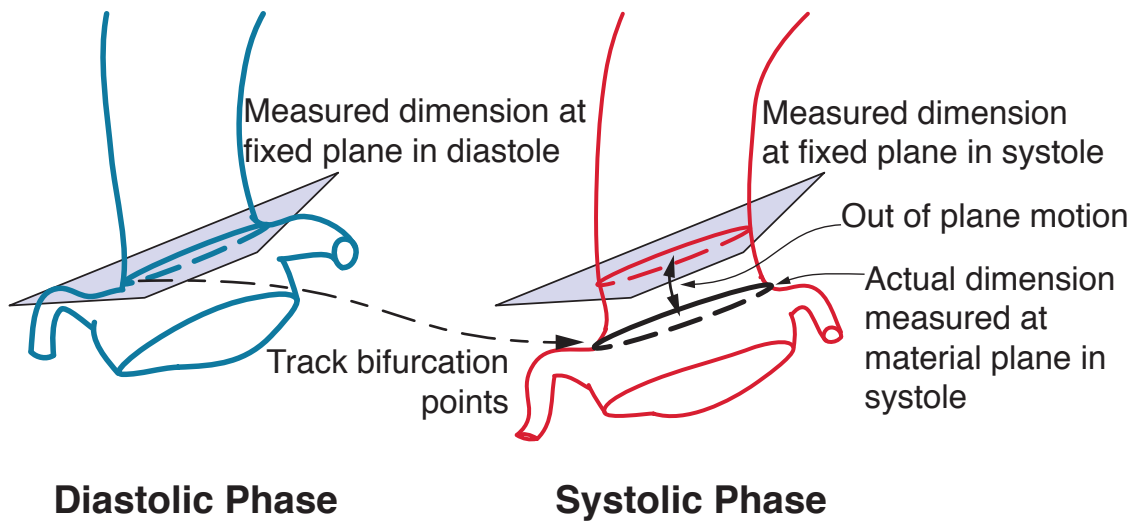


Figure 3.7: Strain quantification study: Lagrangian and Eulerian measurements in the aorta. The figure shows the ascending aorta in diastole (*left*) and systole (*right*). Typically, Eulerian methods use a 2D section which remains fixed in space throughout the cardiac cycle. If out of plane motions are present Eulerian methods are incapable of measuring strain at the same material point. In order to accurately measure strain in the cardiac cycle it is necessary to account for this out of plane displacement and measure strain at the same material plane throughout the cardiac cycle using a so called Lagrangian method. Branching locations are ideal for the identification of such material points. These in turn can then be used to define material planes.

description of strain as they account for both displacement and deformation.

Both publications by Morrison et al. and Muhs et al. used CT which imparts radiation. The study presented here uses MRI data to build 3D segmentations of the thoracic aorta and interrogates these to determine *Longitudinal Strain* (E_{Long}), *Circumferential Strain* (E_{Cir}), and *Volumetric Strain* (E_{Vol}). We applied these techniques to both healthy subjects and AD patients. Unlike CT, MRI has the advantage that it imparts no ionising radiation to the patient.

3.3.3 Image analysis

The primary advantage to measuring deformations using a 3D image volume is that it allows for the use of a Lagrangian frame which can account for complex motions with longitudinal and radial components. As shall be shown in the results, these displacements

can be significant, particularly in the ascending aorta where the vessel is subject to a substantial force due to the contraction of the heart.

In order to track the motion the same material points on the vessel must be determined in both the systolic and diastolic phases. By determining such points, deformations and strains can be accurately calculated. The branching points of fluctuating vessels were identified as material points as they can be clearly distinguished throughout the cardiac cycle. The vessel centreline was constructed in the segmentation and simulation software CRIMSON [42]. The plane defined by the material point and the normal of the centreline relative to each material point was assumed to bisect the vessel wall orthogonally and describe the same material plane throughout the cardiac cycle. The location of these planes will be discussed further in the result section (Section 4.3).

3.3.4 Image segmentation

A novel aspect to this work was to measure the systolic and diastolic E_{Vol} in various sections of the aorta *in vivo*. In order to compute this a segmentation of the vasculature was created. The approach utilised is the same as that for the primary patient specific study. The segmentation was performed with our in house software package CRIMSON [42].

The intensity of the MRI image was inhomogeneous along the length of the vessels and the intensity varied depending on the phase acquired. A useful feature of the CRIMSON package is the image reslice is represented by both the intensity image and by the gradient image (see Figure 3.8). The gradient image highlights regions where there are large variations in the image intensity and allows features such as the vessel wall, where there is a transition from the low intensity pixels representing the blood to the high intensity pixels of the surrounding tissues, to be observed more consistently.

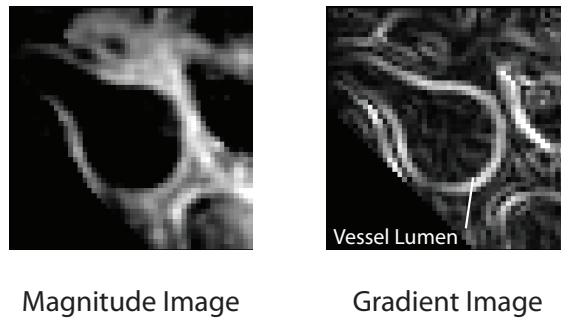


Figure 3.8: Strain quantification study: Magnitude and gradient image The magnitude image is susceptible to variation in intensity and windowing may be necessary. Regardless of the windowing used, the gradient image clearly and consistently highlights the vessel wall (indicated), where there is a transition from the dark blood to the bright tissue and avoids issues with intensity inhomogeneities.

3.3.5 Dimensional measures and strain calculations

CRIMSON [42] was used to compute the circumference of each contour at each material point location in both systole and diastole.

For the centreline and volumetric calculations, the aorta segmentation was meshed without the visceral branches. The aorta was then divided into three parts representing the **Aortic Arch (AA)**, **Ascending Aorta (AAo)** and **Descending Aorta (DA)**. This was performed by first defining a cutting plane using the centre-point and normal of the image reslice at each relevant branching point determined using CRIMSON, these cutting planes were then used to split the model in a commercial **CAD** package [4] and each section was exported as a separate **CAD** model. The volume of each exported segment was calculated. To compute the centreline for each segment, the segments were then meshed and imported into VMTK [163] which allows the calculation of centrelines via the generation of a Voronoi diagram between two points in the mesh [3]. This method of calculating centerlines is well established and can be thought of as the centerline described by the centroids of the series the largest spheres which can be fit inside the volume between each point. For the cases involving **AD** each corresponding section of the **TL** and **FL** were treated separately.

As strain is measured *in vivo*, the calculations of strain do not use the unloaded configuration as the reference configuration, but rather use the state in diastole where the vasculature experiences diastolic pressure and pre-stretch which exists in all blood vessels [48, 14]. A formulation based on the Green-Lagrange strain was used to calculate for E_{Long} and E_{Cir} , as it is independent of rotations and suitable for finite (large) strains,

$$E_{Cir} = \frac{l_{Cir_S}^2 - l_{Cir_D}^2}{2l_{Cir_D}^2} \quad (3.7)$$

$$E_{Long} = \frac{l_{Long_S}^2 - l_{Long_D}^2}{2l_{Long_D}^2} \quad (3.8)$$

where E represents strain, the subscripts S refer to the deformed length (i.e. in systole) and D to the reference length (i.e. in diastole).

For E_{Vol} the volumetric strain formula was used

$$E_{Vol} = \frac{\Delta V}{V_D} \quad (3.9)$$

where $\Delta V = V_S - V_D$. Each strain is visually described in figure 3.9.

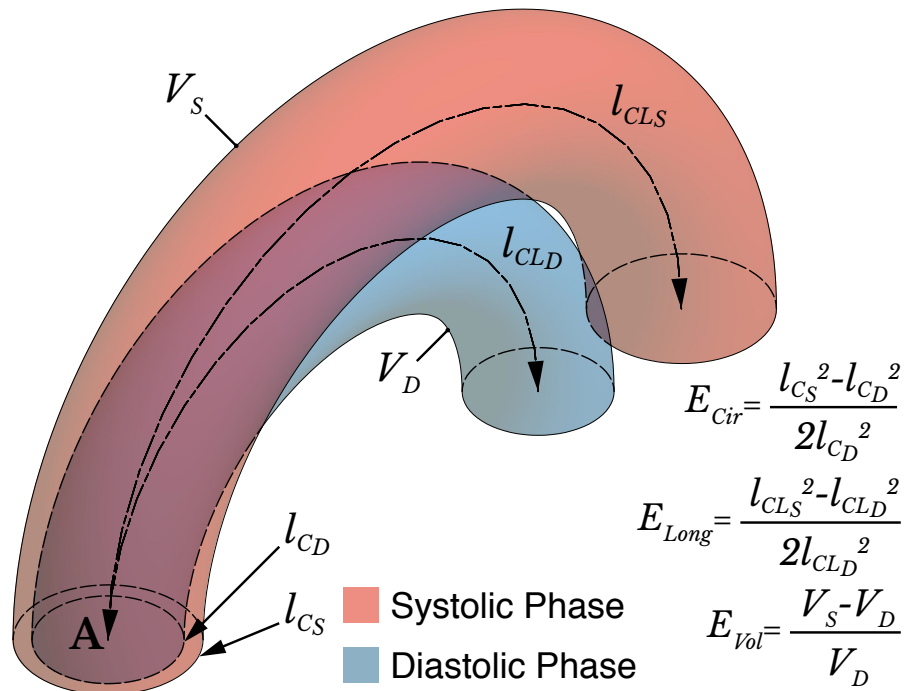


Figure 3.9: Strain quantification study: Measures of strain. The image compares an idealised vessel at diastole (*blue*) and systole (*red*) undergoing expansion and elongation. The vessel is rigidly attached at point A. Highlighted are the circumferential length in systole (L_{CS}) and diastole (L_{CD}) at the cross-section corresponding to point A, the centreline length in systole (L_{CLS}) and diastole (L_{CLD}) and the volume in systole (V_S) and diastole (V_D).

3.4 Impact of septum distensibility on simulated haemodynamics using a LPN

The results of the strain qualification study (Section 4.3) will show that the aorta undergoes significant deformation and that in cases of AD there exists a complex interaction between the TL and FL through the thin septum flap which can undergo relatively large deformations. While every effort was made in the primary patient specific study to segment the AD geometry and reproduce the observed haemodynamics as faithfully as possible, a key element missing in the CFD simulations is these deformations. Presently our simulation software CRIMSON [42] is not capable of modelling the Fluid Structure Interaction (FSI) between the vessel wall and blood, however LPNs may provide a relatively computationally inexpensive way of modelling compliance in the lumina.

As mentioned previously, electrical analogues can be used to represent the vascular system, the [Windkessel RCR](#) models being an example of this. Electrical resistors can be used to model vascular resistance, inductors to model fluid inertia, diodes to model valves and capacitors to model vessel compliance.

A circuit was designed based on the the work previously performed by Rudenick et al. [119] and shall be discussed in more detail in Section 4.4. The circuit was constructed as a Netlist i.e. a list containing all components in the circuit detailing their type, value and connecting pins of each component, in a similar method to that described by Arthurs et al. [159]. At the inlet, the flow profile acquired via [2D PC-MRI](#) for the primary patient specific study (described in Section 3.1.2) was applied.

The resulting set of [Ordinary Differential Equations \(ODEs\)](#) was solved implicitly using the backward Euler method in MATLAB [92]. The simulations were run until a periodic solution was found for both velocity and pressure.

4

RESULTS

This chapter is subdivided into four sections, each will include a full and thorough analysis of all the results acquired for each individual study, starting with the primary patient specific study, followed by the idealised study, then the strain quantification study and finally the OD study. A discussion of the results will be presented in Chapter 5.

Contents

4.1	Primary patient specific study	59
4.1.1	Investigation 1: Haemodynamic alterations in AD	59
4.1.2	Investigation 2: Analysis of the impact of the flap on left ventricular function	70
4.1.3	Investigation 3: Sensitivity study of the impact of secondary entry tears	72
4.2	Computational study of anatomical risk factors	78
4.2.1	Haemodynamic alterations in undissected and dissected aortic models	79
4.2.2	Impact of curvature	82
4.2.3	Impact of FL location relative to aortic curvature	82
4.2.4	Impact of tear size - proximal and distal tears of equal size	84
4.2.5	Impact of the tear size - proximal and distal tear of different sizes .	86
4.2.6	Impact of tear shape	90
4.2.7	Impact of tear patency	90
4.3	Strain quantification via dual phase black blood MRI	93

4.3.1	Measurement locations	93
4.3.2	Healthy subjects	94
4.3.3	Aortic dissection patients	97
4.4	Impact of septum distensibility on simulated haemodynamics using a LPN	101

4.1 Primary patient specific study: Multi-modality image-based computational analysis of haemodynamics in aortic dissection, a patient specific study

The following subsections give the results for the primary patient specific study. The study endeavours to study the haemodynamic impact of different [AD](#) morphometric parameters and includes three investigations:

1. **Haemodynamic alterations in aortic dissection:** An analysis of the haemodynamic changes introduced by the dissection septum in the descending aorta. The results will compare the haemodynamics between the healthy aortic model (created by virtually removing the septum) and the diseased [AD](#) model. The results will consider alterations in pressure, flow, and [WSS](#).
2. **Analysis of the impact of the flap on left ventricular function** The results will show the estimation of the additional stroke work imposed by the [AD](#) using the [LPN](#) heart model.
3. **Sensitivity study of the impact of secondary entry tears** The impact of secondary tears on [AD](#) haemodynamics will be assessed.

4.1.1 Investigation 1: Haemodynamic alterations in AD

The following section shall present the undissected geometry results and then shall compare these to those of the [AD](#) model. For both models, we assumed cardiac output was unaffected by the onset of [AD](#), and the same flow wave form was applied at the inlet. We also assumed that [AD](#) did not affect distal vasculature, represented by the [RCRs](#) at the outlets. The [RCRs](#) were manually tuned using the [AD](#) model to match the [2D PC-MRI](#)

Table 4.1: Primary patient specific study: RCR parameters for investigation 1 RCR parameters for the undissected and AD geometries.

Artery	Abbreviation	R_p $\text{g mm}^{-4} \text{s}^{-1}$	C $\text{mm}^4 \text{s}^2 \text{g}^{-1}$	R_d $\text{g mm}^{-4} \text{s}^{-1}$
Right Common Carotid	RCCA	0.80	6.10	4.53
Right Subclavian	RSCA	0.13	7.64	1.8
Left Common Carotid	LCCA	0.78	6.14	4.40
Left Subclavian	LSCA	0.12	7.87	1.72
Hepatic	Hepatic	0.24	1.15	4.06
Splenic	Splenic	0.14	2.04	2.30
Medial Coeliac	M Coeliac	0.23	1.18	3.95
Superior Mesenteric	SMA	0.13	3.87	1.15
Right Renal 1	R Renal 1	0.48	2.37	1.94
Right Renal 2	R Renal 2	1.11	1.19	4.45
Left Renal	L Renal	0.32	3.34	1.30
Inferior Mesenteric	IMA	0.68	0.73	6.13
Medial Sacral 1	M Sacral 1	0.54	0.52	9.04
Medial Sacral 2	M Sacral 2	0.78	0.36	13.12
Left Internal Iliac	L Int Iliac	0.10	0.15	3.87
Right Internal Iliac	R Int Iliac	0.13	0.15	5.15
Left External Iliac	L Ext Iliac	0.06	0.49	2.49
Right External Iliac	R Ext Iliac	0.06	0.55	2.18

flows in the DA for a total mean flow (both TL and FL) of between 55.6 and 50.3 cm³ s⁻¹. As will be shown, the AD RCR parameters gave typical flow and pressure waveforms when applied to the undissected model. The same RCR parameters were therefore used for both AD and undissected cases [165].

Baseline haemodynamics in the undissected aorta

The undissected aorta model was created from the AD image data by virtually removing the septum for the aortic contours. As no patient-specific data were available for the undissected state, the same flow data derived from the AD 2D PC-MRI study were applied at the inlet. The parameters of each three-element RCR Windkessel model, derived from tuning of the AD model to match 2D PC-MRI data and also applied to the undissected model, are given in Table 4.1.

Figure 4.1 shows pressure and flow wave forms at selected outlets as well as visualisations

of pressure and flow in the aorta at peak systole. The results show physiologically-realistic ranges for flow, pressure and flow splits between different vascular regions [165].

Dissected aorta

Flow through the **AD** model was investigated using the same inlet and outlet boundary conditions as in the preceding analysis. Figure 4.2 shows haemodynamics in the dissected aorta at peak systole. Significant changes are apparent relative to the results depicted in Figure 4.1. In terms of pressure at the different branches, there is a clear increase in pulse pressure at the aortic inflow and the upper branches. The systolic and diastolic **LCCA** pressure are 146/75 mmHg for the undissected case and 159/71 mmHg for the dissected case. The mean pressure for the ascending vessels remains relatively constant. Flow is increased to these branches. Specifically, flow to the **LCCA** is increased by 14.8% in the dissected case. The vessels in the distal **DA** experienced drops in both mean and pulse pressure. For instance, the right external iliac had a mean pressure of 94 mmHg and systolic and diastolic pressures of 151/76 mmHg in the undissected case, whereas the mean, systolic and diastolic pressures for the dissected case are 90 and 147/72 mmHg. Several other outlets experienced changes in pressure and flow, for example, in the **SMA** mean pressure dropped by 6.5% and mean flow by 5.3%. Flow to the vessels branching from the coeliac trunk dropped by a total of 13.5 % and pressure by 13.6 %.

Locally, there are significant alterations in haemodynamics, particularly around the entry tear, **TL** and coeliac trunk regions. Some of these changes are highlighted in Figure 4.3. The spatial distribution of pressure in the dissected model at peak systole around the entry tear ranges between 58.6 and 161.0 mmHg. This range was much smaller in the corresponding region of the undissected model: 92.2-148.0 mmHg. The peak systolic pressure gradient along the length of the **TL** is larger than that seen in the corresponding

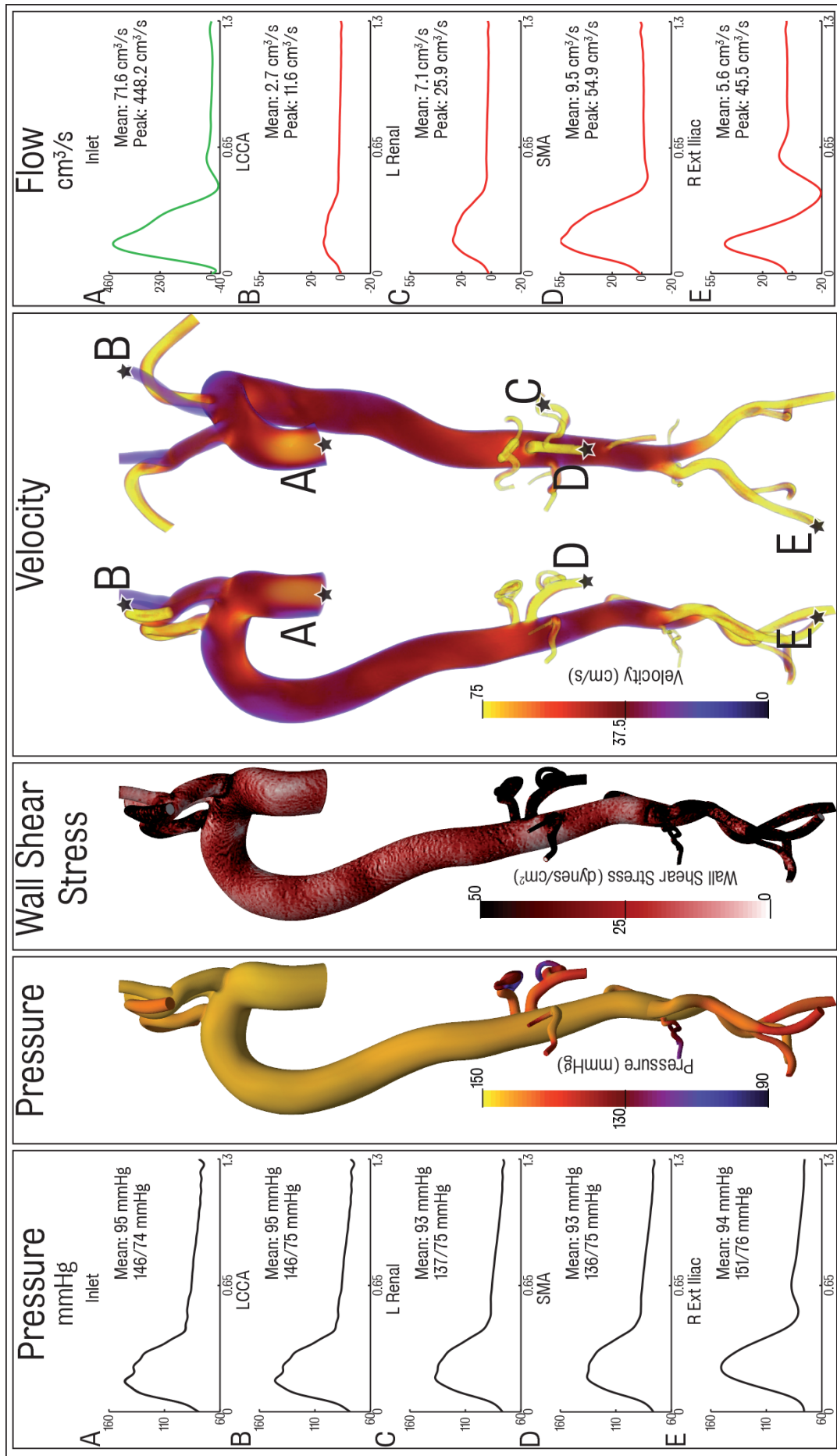


Figure 4.1: Primary patient specific study: Undissected model results Visualisations of pressure, WSS and velocity at the inlet, LCCA, L. Renal, Superior Mesenteric Artery (SMA) and R. Ext Iliac are also shown.

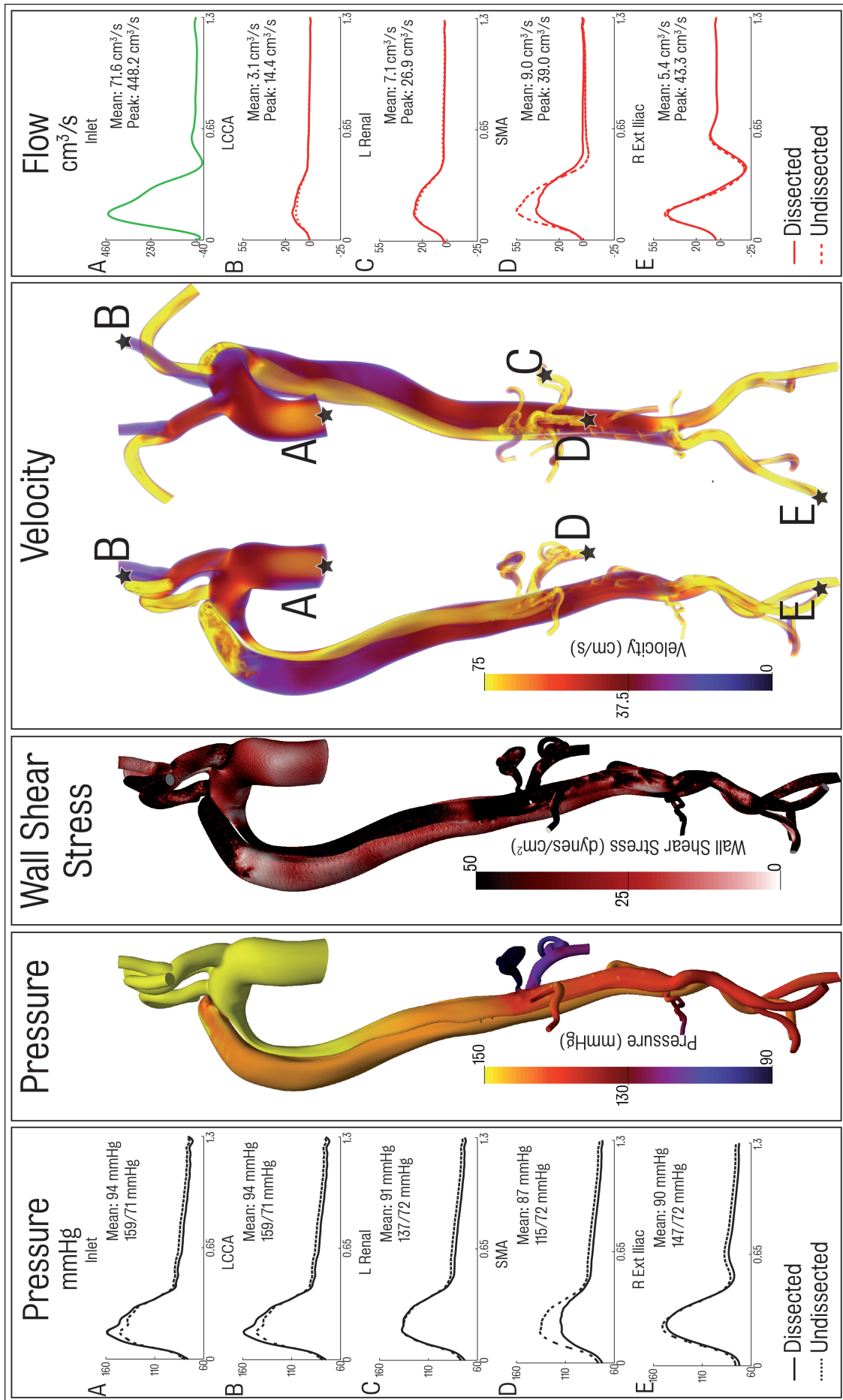


Figure 4-2: Primary patient specific study: Baseline dissected model results Visualisations of pressure, WSS and velocity for the baseline dissected model at peak systole. Shown also are comparative pressure and flow waveform plots at the inlet, LCCA, L Renal, SMA and R Ext Iliac for both the undissected and dissected models

location of the undissected aorta: from 160 mmHg at the entry tear to 135 mmHg at the exit tear in the dissected model. Correspondingly, the undissected model has a pressure gradient of 5 mmHg in the DA with pressures in the range of 145-140 mmHg. Pressure in the proximal portion of the dissection is generally higher in the TL than in the FL. The reverse trend is observed in the distal portion. This pattern has also been noted in other studies [144, 2]. An area of marked increased pressure (over 160 mmHg) is observed where flow through the entry tear impinges on the wall of the FL. This localised region of high blood pressure on the structurally compromised FL could lead to future enlargement and potential rupture [142, 15].

The AD case shows large TL peak velocities in the range of 70 cm s^{-1} in the coeliac trunk region where there is a large flow demand. Distal to the coeliac trunk region, there is a significant drop in peak velocities. The computed values of 35 cm s^{-1} are comparable with those seen in the undissected case.

Highly complex FL flow patterns are observed in the entry tear region. A dramatic increase in Time Averaged Wall Shear Stress (TAWSS) from approximately 5 dynes cm^{-2} in the undissected case to over $100 \text{ dynes cm}^{-2}$ in the dissected case is observed. A more moderate increase in TL TAWSS is observed in the coeliac trunk region, going from 5 to 10 dynes cm^{-2} in the undissected case to over 20 dynes cm^{-2} in the dissected case.

Comparison between computed and measured flows in the descending aorta

In this section, we compare the computed flows in the TL and FL with those measured using 2D PC-MRI at three different locations in the descending thoracic aorta. For clarity, these shall be referred to as proximal, medial and distal locations. Figure 4.4 shows quantitative comparisons of 2D PC-MRI and simulation data at each location and

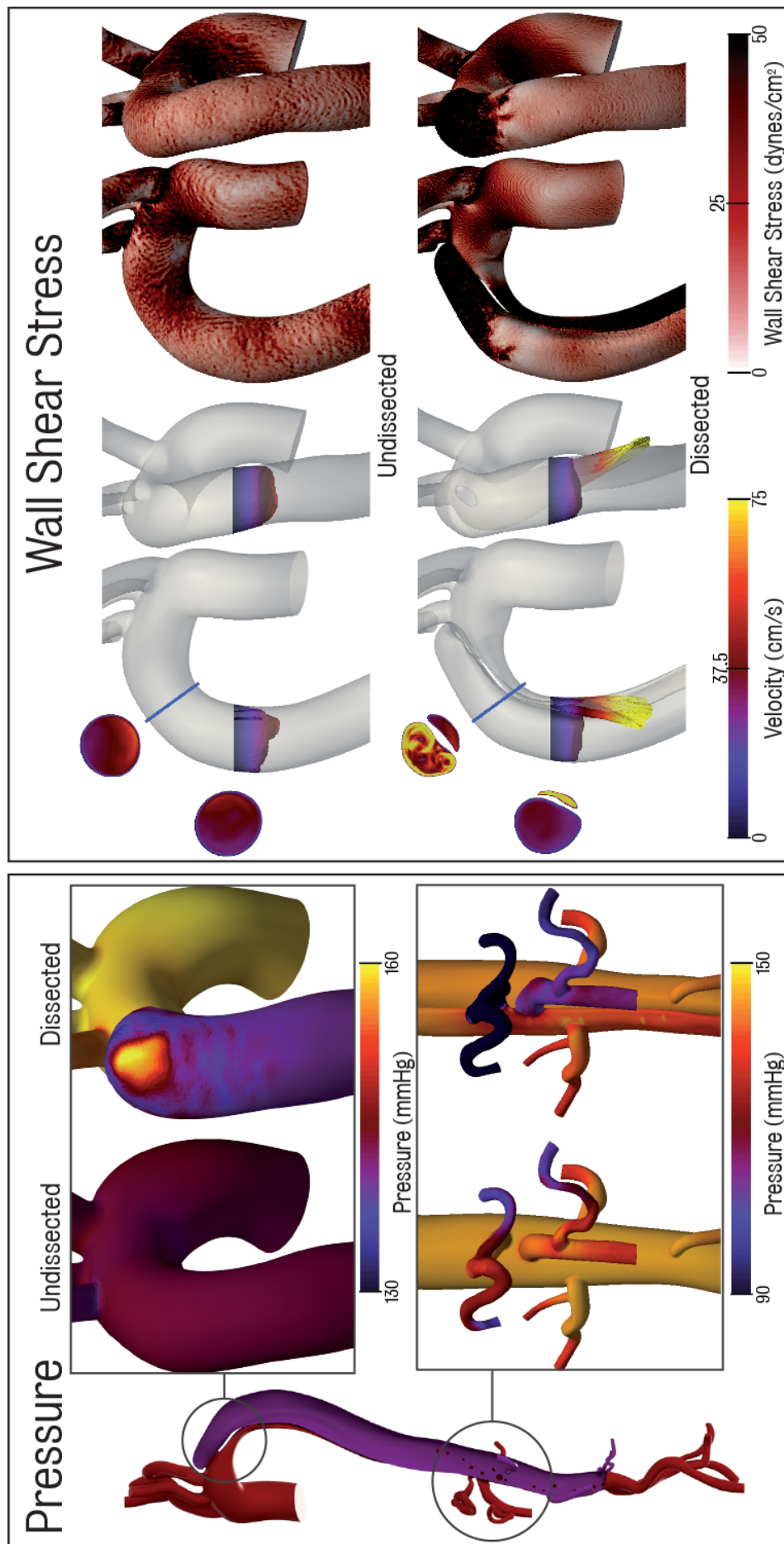


Figure 4.3: Primary patient specific study: Regions affected due to the presence of AD Localised regions of haemodynamic change in the presence of dissection comparing pressure and WSS at peak systole between the dissected and undissected models

Figure 4.5 shows a comparison of the spatial distribution of velocity for PC-MRI and simulation data at each location. The 2D PC-MRI data in this figure displays evidence of more complex flows in the FL at the proximal location as observed in the CFD analysis. There is good agreement in mean flows in TL and FL between simulation and imaging data. The PC-MRI gives a total flow (e.g. sum of TL and FL flow) at each location of 55.6, 53.8 and 50.3 cm³ s⁻¹ respectively. The computation predicts a uniform value for the total flow of 51.4 cm³ s⁻¹ at each location, resulting in relative errors between measurement and simulation of 7.6, 4.5 and +2.2 %, respectively. It is important to note that this good agreement in total mean flow between data and simulations was not imposed in any way, but rather the result of properly tuned outflow boundary conditions in the remaining branches of the model as these dictated the flow splits to the different branches, as well as a realistic reconstruction of the aortic anatomy. On average, the FL carried 79 % of the total descending aortic flow according to the PC-MRI, whereas in the simulation this value was 76 %.

Examining each lumen individually, PC-MRI FL mean flows at each location are 40.6, 42.5 and 42.4 cm³ s⁻¹, whereas the simulations produce a nearly uniform mean value of 38.7 cm³ s⁻¹ at all three locations, resulting in relative errors of 4.7, 8.9 and 8.7 %, respectively. Considering the TL, PC-MRI mean flows are 15.1, 11.1 and 7.9 cm³ s⁻¹ at each of the measurement locations, while the computations show a constant value of 12.7 cm³ s⁻¹ for all three locations and relative errors of 15.9, +14.4 and +60.8 %, respectively. The larger relative errors in TL flow can be explained by the smaller mean values recorded at this location. On average, PC-MRI data show the TL carries 21 % of total flow, whereas in the simulation this value is 25 %.

The Velocity Encoding (VENC) is a prescribed parameter for PC-MRI which is set prior to image acquisition and places an upper limit on the range of velocities which can be

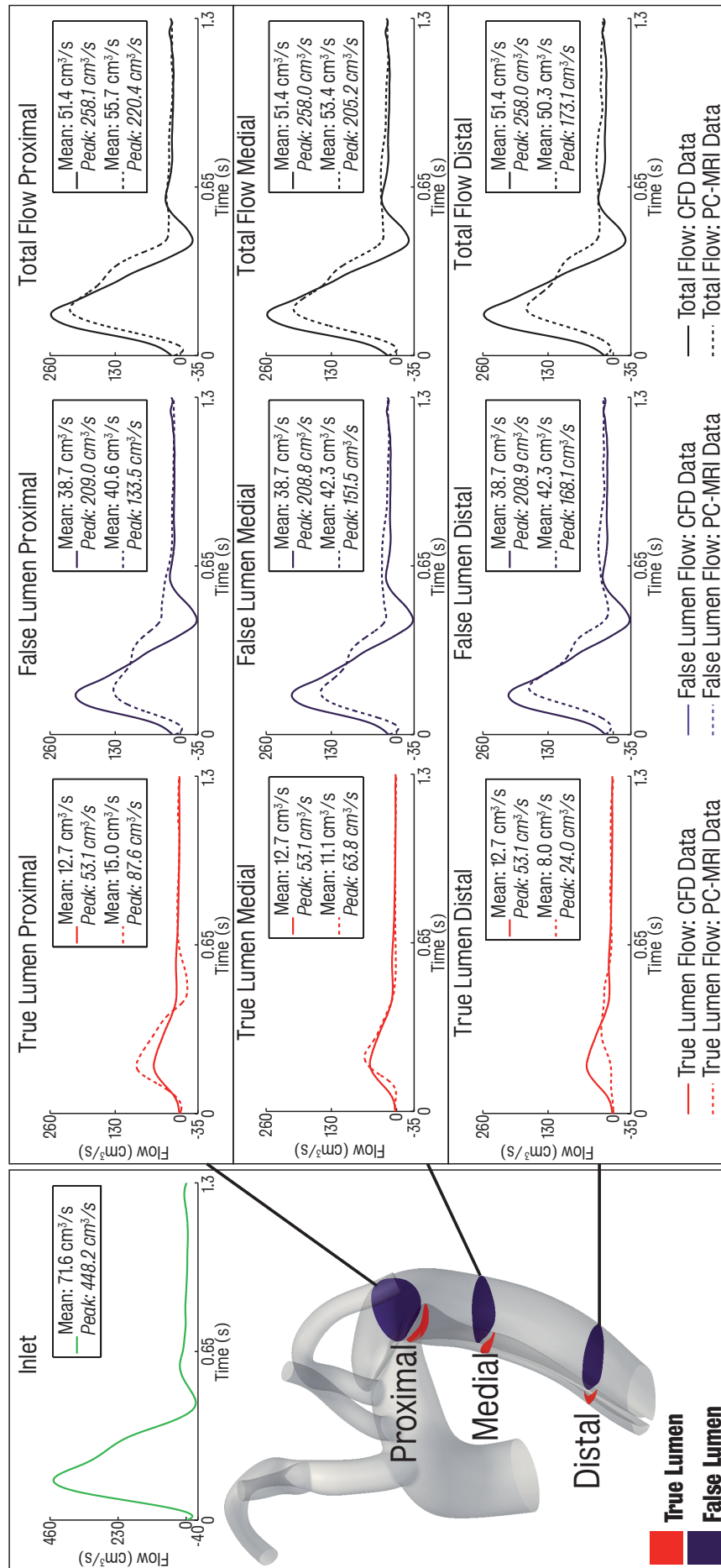


Figure 4.4: Primary patient specific study: 2D PC-MRI versus CFD results Comparison between PC-MRI and CFD simulation flow data for the TL, FL and total flow. TL is shown in red, FL in purple and total flow in black. CFD data are shown by the solid lines, while 2D PC-MRI data are presented in the dashed lines

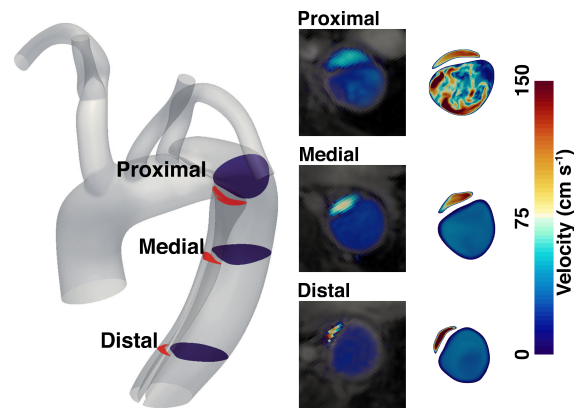


Figure 4.5: Primary patient specific study: 2D PC-MRI versus CFD velocity results at peak systole. The figure compares the spatial distribution of velocity between 2D PC-MRI and CFD simulation data at each of the measured locations at peak systole shown with the same scale. As the simulations were rigid, systolic velocities observed in the CFD simulation tended to be higher than in the 2D PC-MRI data. In both the CFD and 2D PC-MRI the largest velocities were observed in the TL.

acquired. The $VENC$ must be carefully chosen, as too low a value will cause aliasing while if the $VENC$ is too large it may lead to a high degree of noise and an inability to detect lower values of velocity. For the present study, PC-MRI data were acquired with single $VENC$, but as peak velocities were significantly lower in the FL than in the TL (in the order of 50 % less), TL and FL flows may have differed somewhat from what was recorded.

Overall, the small differences in flow between the three locations are to be expected due to the close proximity of the different slices (11 cm between proximal and distal slices) and the apparent lack of secondary connecting tears or branching vessels between the proximal and distal slices. The increase in measured FL flow from the proximal to the distal location (40.6 vs. 42.3 $\text{cm}^3 \text{s}^{-1}$) could suggest the presence of a connecting tear. However, this could not be located in the 4D PC-MRI. In the simulation data, the lack of connecting tears results in identical flows at each location due to the rigid wall and blood incompressibility assumptions. In Section 4.1.3, we study the impact that additional connecting tears between lumina may have in the aortic haemodynamics.

Despite the mean flows being relatively well matched between PC-MRI and simulated

data, larger discrepancies exist when considering the systolic and diastolic range at each location. In the **TL** at two of the three locations, the peak-to-peak range of flows from the simulated data underestimated that of the **PC-MRI** data, while in all three **FL** locations the amplitude of the simulated waveforms is larger than that of the **PC-MRI** data. **PC-MRI** data for the **TL** have a systolic/diastolic range of 13.8/87.6, 0.8/63.4 and 0.6/24.0 $\text{cm}^3 \text{s}^{-1}$ at the respective locations, while the simulated data at the same locations have a range of 1.9/53.1, 1.9/53.1 and 1.9/53.1 $\text{cm}^3 \text{s}^{-1}$. In the **FL**, the **PC-MRI** data have a range of 133.5/10.3, 151.5/14.9 and 168.1/10.1 $\text{cm}^3 \text{s}^{-1}$ at the respective locations, while the corresponding simulated data show ranges of 209.0/32.7, 208.8/32.8 and 208.9/32.8 $\text{cm}^3 \text{s}^{-1}$. These discrepancies may be explained by the lack of compliance in the rigid 3D aortic model. In reality, the vessel walls are compliant and the septum is seen to deform significantly, especially in an acute setting. The arterial compliance enables the vessel to accommodate part of the blood volume during systole, reducing the peak flow rates through a given section. In early diastole, the stored blood volume is released, increasing flow during diastole. A rigid 3D model cannot capture this effect however, and the only compliance in the computational model is provided by the capacitor component in the 0D **Windkessel** model coupled to each outlet. While the mean inflow over the cycle will be balanced by the sum of mean outflows, aortic compliance enables blood volume to be stored at peak systole and then be released later in diastole. Therefore, this overestimation in the peak-to-peak range of flow of the simulated data is expected if the domain is modelled as rigid.

4.1.2 Investigation 2: Analysis of the impact of the flap on left ventricular function

In this investigation, a lumped-parameter heart model was coupled to the inlet face of the AD and undissected models to examine changes in stroke work induced by the AD. Via the definition of an elastance function, the heart model enables the quantification of left ventricular volume and pressure throughout the cardiac cycle. From these data, a Pressure-Volume (PV) loop can be generated to quantify the cardiac workload. The cardiac output, measured with MRI in the dissected aorta, was assumed to be identical for both dissected and undissected cases. This is a reasonable first approximation, as the heart is known to adjust to changes in afterload to maintain a relatively constant output that satisfies the metabolic demands [82]. The outflow boundary conditions were kept unchanged. The elastance function characterising the performance of the heart model was adjusted in both cases to match the measured flow waveform at the level of the aortic root. This iterative process sought to match mean cardiac output, systolic cardiac output, cardiac cycle and length of systolic phase. The adjusted parameters were maximum elastance, time to maximum elastance and time to relaxation (Table 4.2). The table shows the maximum elastance increased from $0.4 \text{ g mm}^{-4} \text{ s}^{-2}$ to $0.46 \text{ g mm}^{-4} \text{ s}^{-2}$ when the AD is introduced, indicating the heart must perform more work when in the presence of an AD to maintain the same level of flow. Iterations on maximum elastance and time to maximum elastance parameters stopped when the obtained maximum and mean cardiac output were within 5 % of the measured PC-MRI values.

The left panel of Figure 4.6 shows a good match in the waveforms generated via the 0D heart model and the physiological PC-MRI data. The heart model waveforms for both dissected and undissected cases lack the slight early diastolic back flow observed in the PC-MRI data. This is a direct consequence of the way the aortic valve is modelled in the

Table 4.2: Primary patient specific study: Heart model parameters
Tuned parameters of the heart model for the dissected and undissected models.
Values marked with an * were taken from Lau and Figueroa [82].

	Dissected Model	Undissected Model
Period (s)	1.3	1.3
End diastolic volume (mm ³) *	130,000	130,000
Unstressed volume (mm ³) *	0.0	0.0
Preload [g mm ⁻¹ s ⁻²] *	533.320	533.320
Time to maximum elastance [s]	0.410	0.420
Time to relaxation [s]	0.205	0.210
Maximum elastance [g mm ⁻⁴ s ⁻²]	0.460	0.400
Minimum elastance [g mm ⁻⁴ s ⁻²] *	4.102×10^{-3}	4.102×10^{-3}
Aortic valve resistance [g mm ⁻⁴ s ⁻²] *	1.0×10^{-5}	1.0×10^{-5}
Aortic valve inductance [g mm ⁻⁴] *	1.0×10^{-5}	1.0×10^{-5}
Ventricular resistance [g mm ⁻⁴ s ⁻²] *	5.0×10^{-7}	5.0×10^{-7}
Mitral valve resistance g mm ⁻⁴ s ⁻²] *	3.9453×10^{-7}	3.9453×10^{-7}
Mitral valve inductance [g mm ⁻⁴] *	1.334×10^{-5}	1.334×10^{-5}

0D heart model (see Figure 3.4): the diode representing the function of the aortic valve closes instantly as soon an adverse pressure gradient between the left ventricle and the aorta is detected. This effectively precludes back flow when using the heart model.

The right panel of Figure 4.6 shows the PV loops for both AD and undissected cases. The four distinct phases of the cardiac cycle (ventricular filling, isovolumetric contraction, ejection and isovolumetric relaxation) as well as the aortic valve opening and closing can be observed in the diagrams. The estimated left ventricular work load, quantified by the area enclosed by the plot, shows a significant increase (13.7 %) in the AD case work (1.9 kJ), relative to the work performed by the heart in the undissected anatomy (1.7 kJ). The increased in work is the result of an increase in maximum elastance during peak systole due to the higher afterload in the dissected case. The presence of the septum therefore makes the heart work harder to produce the same cardiac output as in the undissected case.

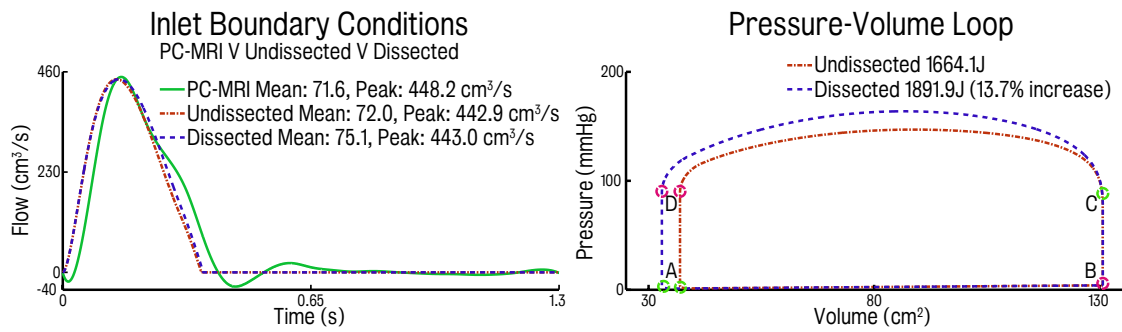


Figure 4.6: Primary patient specific study: Inflow waveforms and PV loops *Left* inflow waveforms obtained with PC-MRI and heart model. *Right* PV loops generated via using the heart model for both the undissected and dissected simulations. The PV loops illustrate the mitral valve opening (A), the diastolic ventricular filling (A-B), mitral valve closing (B), isovolumetric contraction (B-C), aortic valve opening (C), ejection (C-D), aortic valve closing (D), followed by isovolumetric relaxation (D-A). The area enclosed by the PV loop represents the left ventricular stroke work. There is an increase in the stroke work of 13.7 % in the presence of dissection.

4.1.3 Investigation 3: Sensitivity study of the impact of secondary entry tears

While the location of some of the tears appeared to be clear in the CTA (see Figure 4.7, left), the tear location could not be confirmed by the 4D PC-MRI data, as there was no distinct change in the velocity field that would indicate a connection between the TL and FL (see Figure 4.7, centre and right panels). These panels also show a comparison between CFD and 4D PC-MRI streamlines at peak systole and mid-diastole. Good qualitative agreement between patterns in the velocity field in data and simulation can be observed: for example, high velocities around the main entry tear and in the TL are apparent in both imaging and simulation data. An important question therefore remains, do secondary tears have a significant impact on AD haemodynamics and is there a better agreement between clinical data (e.g. MR-derived flow) and CFD results when secondary tears are included?

An investigation was thus designed to investigate the influence of secondary tears on AD haemodynamics. Two modifications of the 17 tear baseline dissected model were constructed. The first is a maximal tears model in which two additional tears in the

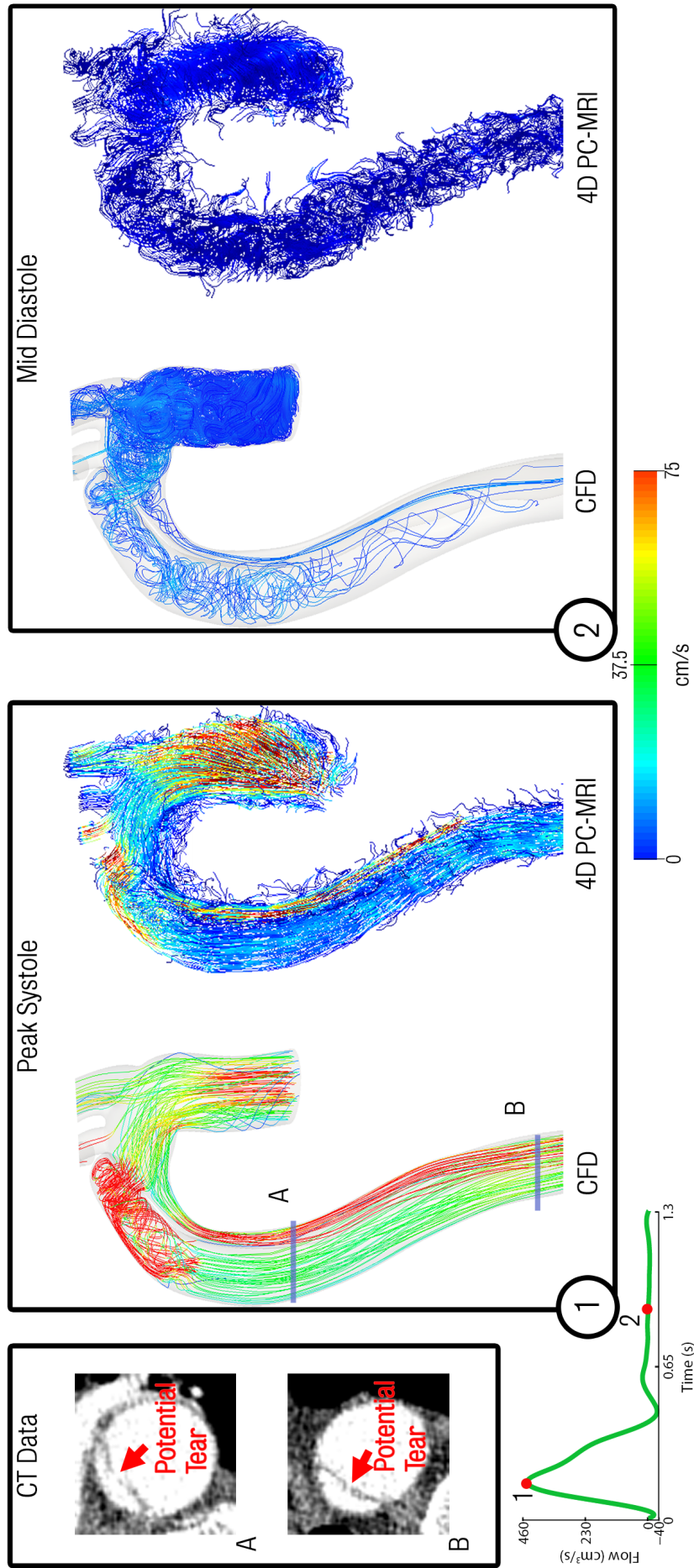


Figure 4.7: Primary patient specific study: CFD V 4D PC-MRI Comparison of CFD data and acquired 4D PC-MRI flow data at peak systole and mid-diastole. Also shown are the CT image data at two locations showing suspected secondary tears which were not apparent on the 4D PC-MRI data

Table 4.3: Primary patient specific study: Mesh sizes Final mesh sizes for each dissected model

Model	Mesh size($\times 10^6$)
Baseline dissected	1.8 nodes/11.8 elements
Maximal tears	2.4 nodes/13.2 elements
Minimal tears	1.8 nodes/11.5 elements

DA were included. These tears, while evident on the CT data, were not seen in the 4D PC-MRI data. The second is a minimal tears model containing only the primary entry and exit tears (see Figure 4.8). The final adapted finite element mesh sizes for all three models are given in Table 4.3.

Comparisons between the 2D PC-MRI data acquired and CFD results at each of the three locations (proximal, medial and distal) for the three dissection models are shown in the top panel of Figure 4.9. The computed total flow (defined as the sum of TL and FL flow) shows a good comparison with the 2D PC-MRI data for all three models, with mean simulation errors ranging from 3 % (maximal tears) to 1.4 % (minimal tears). However, when comparing flow through each individual lumen, the minimal tears case shows larger errors than the baseline and maximal tears models: 122.6 % mean error in the TL and 34.7 % error in the FL. The baseline and maximal tears models show similar results, and match the 2D PC-MRI data more closely.

The bottom panel of Figure 4.9 shows a comparison of flow and pressure waveforms in the region proximal to the coeliac trunk for each of the models. Note that no patient-specific data were acquired in this region, and this comparison is presented to highlight the differences between each simulation. The results show that the baseline dissected and maximal tears cases are relatively comparable, whereas the pressure and flow waveforms in the minimal tears case are significantly different. These differences are more pronounced in TL, where large changes in peak (+81.4 %) and mean (+87.3 %) flow and peak pressure (17.8 %) are observed relative the baseline dissected case. Tears in the

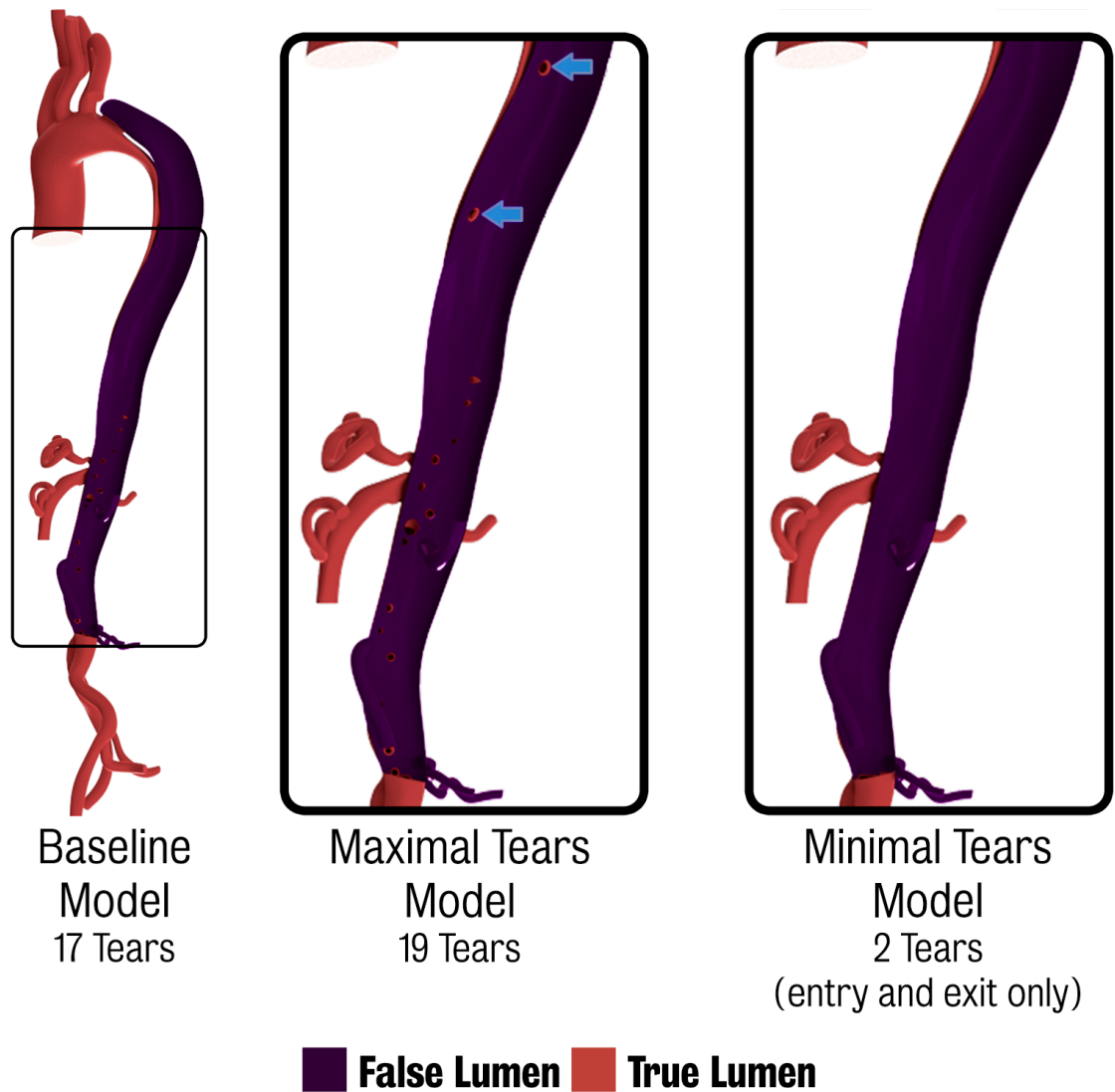
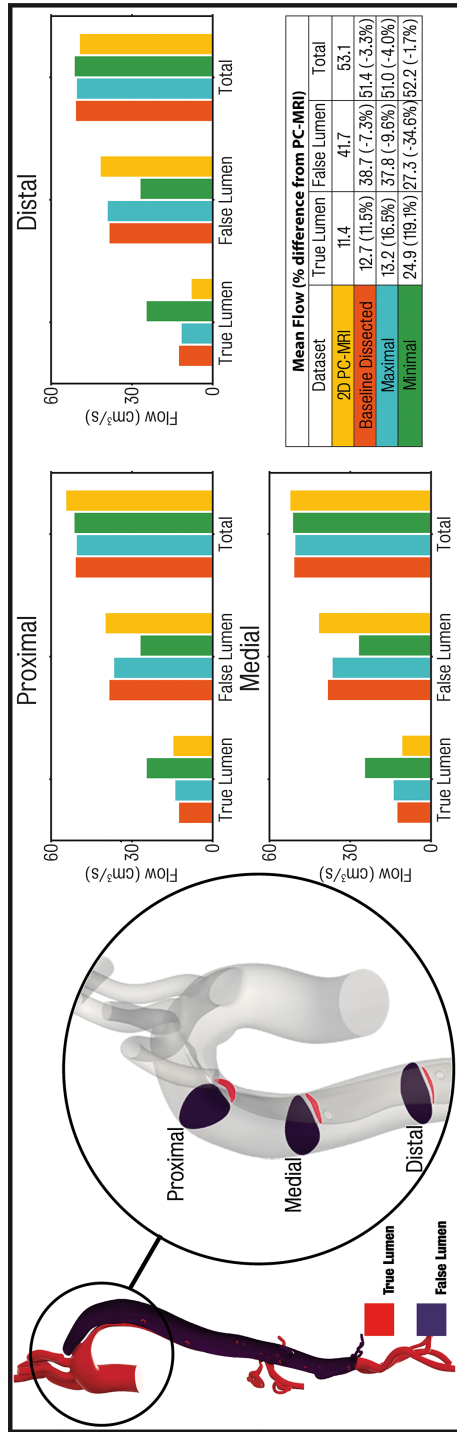


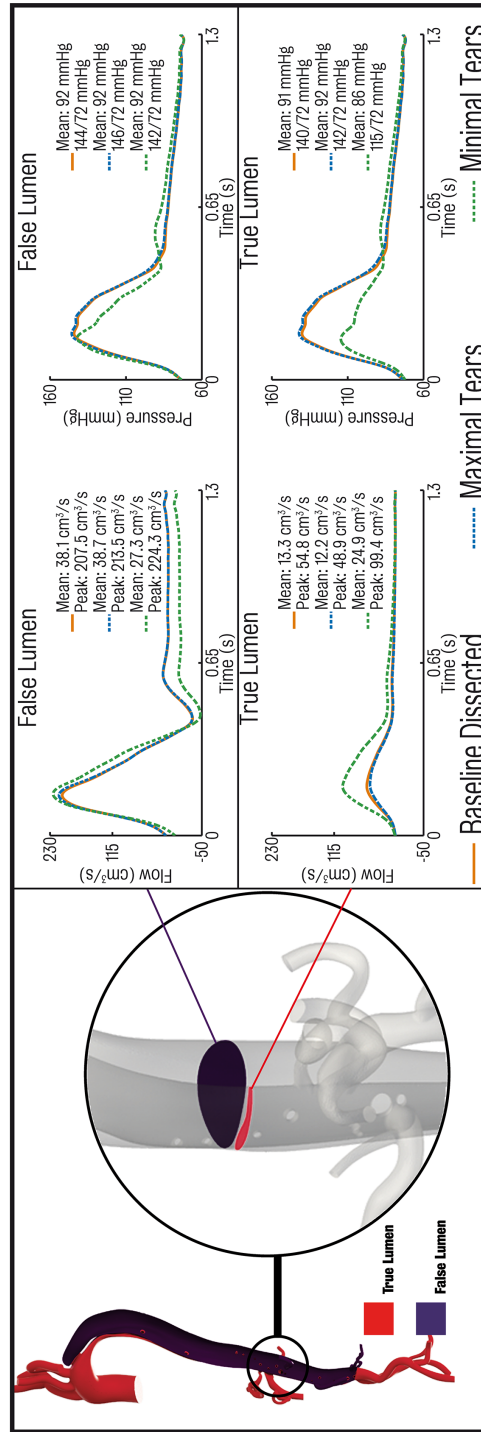
Figure 4.8: Primary patient specific study: Effect of tear patency on TL and FL flow and pressure *Left* baseline dissected model featuring a total of 17 tears. *Centre* maximal tears model with two additional tears in the descending aorta evident in the CT data but not in 4D PC-MRI. *Right* minimal tears model where all but the primary entry and exit tears were removed.

septum allow pressure between the TL and FL to equalise. In the minimal tears case there are no tears locally and the TL is solely responsible for supplying the total demand of the side branches which results in an increased flow demand in the TL. From Poiseuille's law, the effective cross-sectional area communicating blood to the TL decreases due to the absence of the communicating tears resulting in a pressure drop.

These results suggest that in this case some tears do indeed exit in the trunk region given that the minimal tears case shows results clearly different from the baseline and maximal tears, and with higher errors compared to the 2D PC-MRI data. The issue however still remains, as these small secondary tears in a thin and highly distensible dissection flap prove to be very difficult to image.



Mean flows at 2D PC-MRI Locations



Flow and pressure waveforms at celiac trunk region

Figure 4.9: Primary patient specific study: Effect of altering number of secondary patent tears *Top* comparison of computed mean flows and 2D PC-MRI data for the proximal, medial and distal locations of the descending thoracic aorta. The table gives average values of error over the three locations. *Bottom* computed pressure and flow waveforms for each of the three dissection models at a location just proximal to the coeliac trunk

4.2 Computational study of anatomical risk factors in idealised models of TBAD

The results of the primary patient specific study show that geometrical features can have a significant impact on AD haemodynamics. In order to assess the degree of influence of individual features, this series uses a series of idealised CAD models of TBAD which vary a number of geometrical features in a highly controlled manner to assess the impact each feature has on AD haemodynamics.

We first compared haemodynamics in a normal (i.e. undissected) and a dissected aorta. Then we investigated the impact of curvature by comparing different curved models (baseline, candy-cane and curved) with a straight AD model. We then analysed the impact of FL location relative to the aortic curvature (inner or outer) in the curved models. Next, the impact of tear diameter was investigated. Three different tear diameters were considered: 4, 10 and 20 mm, and five models were created: S_4-4 , S_{10-10} , S_{20-20} , S_4-10 , S_{10-4} . Tear shape was also analysed in two models comparing circular versus elliptical tears: S_{10-10} and $S_{10-10-el}$. Finally, the impact of tear patency (e.g. occlusion of proximal and distal tears) and proximal stenting was examined.

Each study shall be summarised with a figure structured as follows: A schematic of the CAD models under investigation shall be shown with each of the 5 locations of interest (inlet, proximal of AD, middle of AD and distal of AD, and outlet) marked with the letters A-E. Panels will provide plots of pressure against time and bar plots of Mean Pressure (MP), given in mmHg at each location. The TL and FL are presented separately in the AD.

4.2.1 Haemodynamic alterations in undissected and dissected aortic models

Pressure

Inlet Pulse Pressure (PP) and MP increased by 61% and 5%, respectively, in the baseline dissected model compared with the undissected (Figure 4.10). The TL experienced larger gradients in PP (63% drop) and MP (5% drop) compared to the undissected model (41% drop in PP and nearly constant MP along the length of the FL). Conversely, the FL showed relatively constant values of PP and MP along its length. Interestingly, these values are higher than in the undissected case: the difference in PP between the FL and the undissected case varies between 7 mmHg at the proximal location and 24 mmHg at the distal location. The difference in MP between the FL and the undissected case is nearly constant, around 2 mmHg.

Mean flow and velocity

A 78/22 % flow split between TL and FL was found in the baseline dissected model (Table 4.4). Mid-TL and FL velocities were respectively 2.7 times faster and 4.3 times slower in the dissected model compared to the undissected model. Large peak systolic velocities were observed at the proximal and distal tears (Table 4.5).

In summary, dissection resulted in increased inlet pulse and mean pressure, and large PP and MP gradients down the TL. These alterations can be explained by the increased resistance introduced by the flap and energy losses due to the complex flow around the tears.

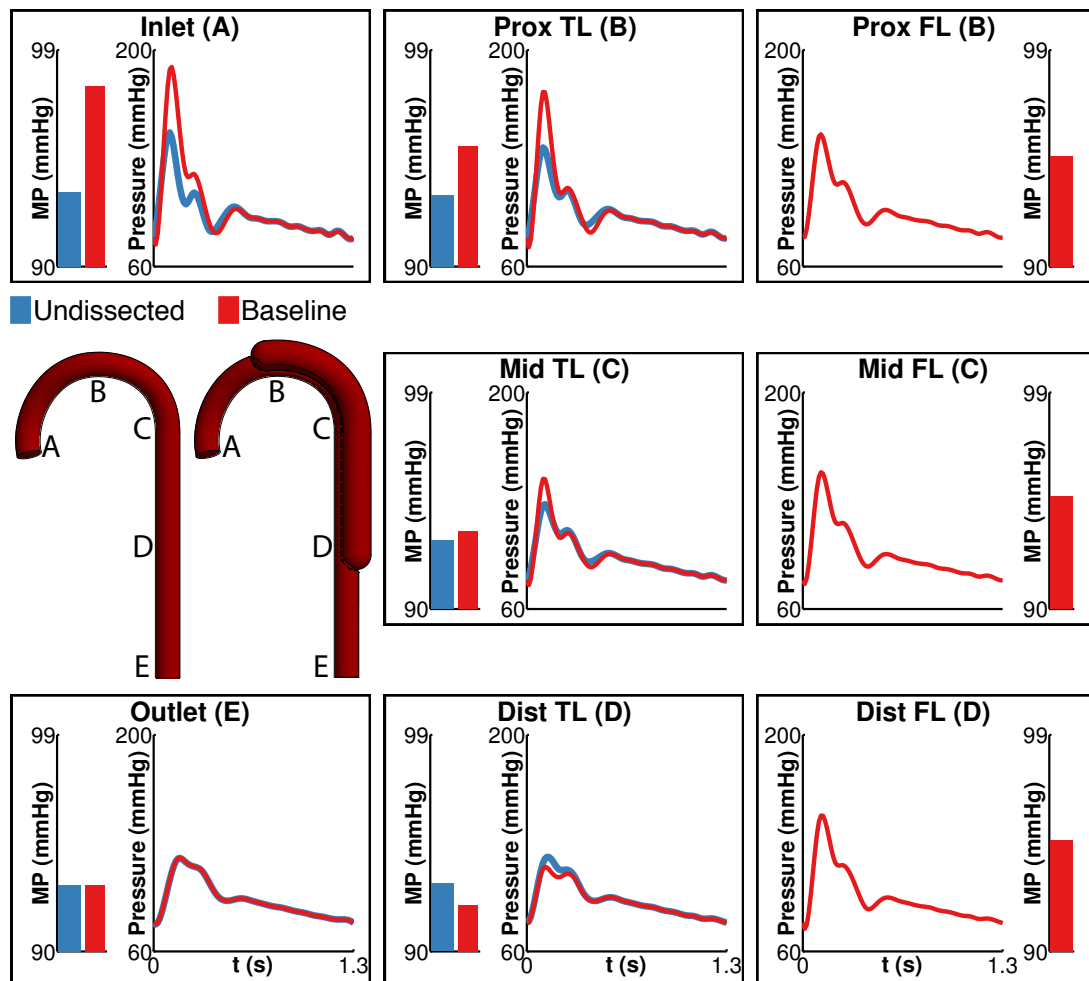


Figure 4.10: Anatomical risk factors in idealised models study: Pressure alterations in undissected and dissected aortic models *Left-middle* Schematic of the undissected and baseline dissected models. The proximal and distal tear of the baseline model are 10 mm diameter. Plots of pressure against time and MP (mmHg) along the TL and FL and at the inlet and outlet are shown in the panels. The designations A-E correspond to the location under consideration.

Table 4.4: Anatomical risk factors in idealised models study: Mean flows ($\text{cm}^3 \text{s}^{-1}$) at the inlet (inflow), in the **TL** Q_m ($\text{cm}^3 \text{s}^{-1}$) and **FL** Q_m ($\text{cm}^3 \text{s}^{-1}$), at the outlet. Percentages (%) referred to fraction of total flow in the dissection.

Models	Inflow ($\text{cm}^3 \text{s}^{-1}$)	TL Q_m ($\text{cm}^3 \text{s}^{-1}$)	FL Q_m ($\text{cm}^3 \text{s}^{-1}$)	Outflow ($\text{cm}^3 \text{s}^{-1}$)
<i>Normal</i>	64.5	-	-	64.5
<i>Baseline</i>	64.2	50.7 (79%)	13.5 (21%)	64.2
<i>Candy-cane</i>	64.2	50.8 (79%)	13.4 (21%)	64.2
<i>C4-4</i>	64.2	60.7 (94%)	3.5 (6%)	64.2
<i>C4-4-in</i>	64.2	60.9 (95%)	3.4 (5%)	64.2
<i>C10-10</i>	64.2	51.4 (80%)	12.8 (20%)	64.2
<i>C10-10-in</i>	64.2	52.6 (82%)	11.7 (18%)	64.2
<i>S4-4</i>	64.2	61.0 (95%)	3.2 (5%)	64.2
<i>S10-4</i>	64.2	59.7 (93%)	4.6 (7%)	64.2
<i>S4-10</i>	64.2	59.9 (93%)	4.3 (7%)	64.2
<i>S10-10</i>	64.2	52.2 (81%)	12.0 (19%)	64.2
<i>S10-10-el</i>	64.2	52.8 (82%)	11.4 (18%)	64.2
<i>S10-0</i>	64.2	64.2 (100%)	0 (0%)	64.2
<i>S0-10</i>	64.2	64.2 (100%)	0 (0%)	64.2
<i>St-0-10</i>	64.2	64.2 (100%)	0 (0%)	64.2
<i>S20-20</i>	64.2	20.9 (33%)	43.3 (67%)	64.2

Table 4.5: Anatomical risk factors in idealised models study: Peak velocities (cm s^{-1}) at proximal and distal tears and in the middle of the **TL** (Mid-TL) and the **FL** (Mid-FL).

Models	Proximal Tear	Distal Tear	Mid-TL	Mid-FL
<i>Normal</i>	101	-	-	101
<i>Baseline</i>	217	214	272	23
<i>Candy-cane</i>	225	223	267	28
<i>C4-4</i>	298	299	376	7
<i>C4-4-in</i>	308	307	392	6
<i>C10-10</i>	225	225	272	30
<i>C10-10-in</i>	235	235	281	26
<i>S4-4</i>	302	300	391	6
<i>S10-4</i>	67	421	380	7
<i>S4-10</i>	420	67	381	7
<i>S10-10</i>	228	227	283	36
<i>S10-10-el</i>	222	217	276	30
<i>S10-0</i>	0	-	416	0
<i>S0-10</i>	-	0	417	0
<i>St-0-10</i>	-	0	90	0
<i>S20-20</i>	105	105	87	48

4.2.2 Impact of curvature

We investigated the haemodynamic differences between baseline, candy-cane, curved and straight dissection models (Figure 4.11) with the goal of assessing the impact of curvature. All models had 10 mm diameter proximal and distal tears and the curved models had a **FL** located on the outer curvature.

Pressure

All models showed similar **PP** and **MP** in both **TL** and **FL**. Differences in inlet **PP** and **MP** between the straight and the baseline cases were 4 % for **PP** and 0.4 % for **MP** (Figure 4.11).

Mean flow and velocity

A 80/20 % flow split between **TL** and **FL** was found in all models (Table 4.4). Mid-**TL** velocities were similar in all cases: range 267-283 cm s⁻¹. Mid **FL** velocities were smaller and similar in range among all cases: range 23-36 cm s⁻¹. The straight case showed the largest **TL** and **FL** velocities. Large peak systolic velocities were observed at proximal and distal tears (Table 4.5).

In summary, curvature did not have a significant impact on **PP**, **MP** or ratio of flows between **TL** and **FL**.

4.2.3 Impact of **FL** location relative to aortic curvature

We next assessed the impact of **FL** location relative to the arch. We compared two models: *C10-10-in*, in which the **FL** is on the inner curvature, and *C10-10* in which the **FL** is on the outer curvature. Both models had 10-mm diameter proximal and distal

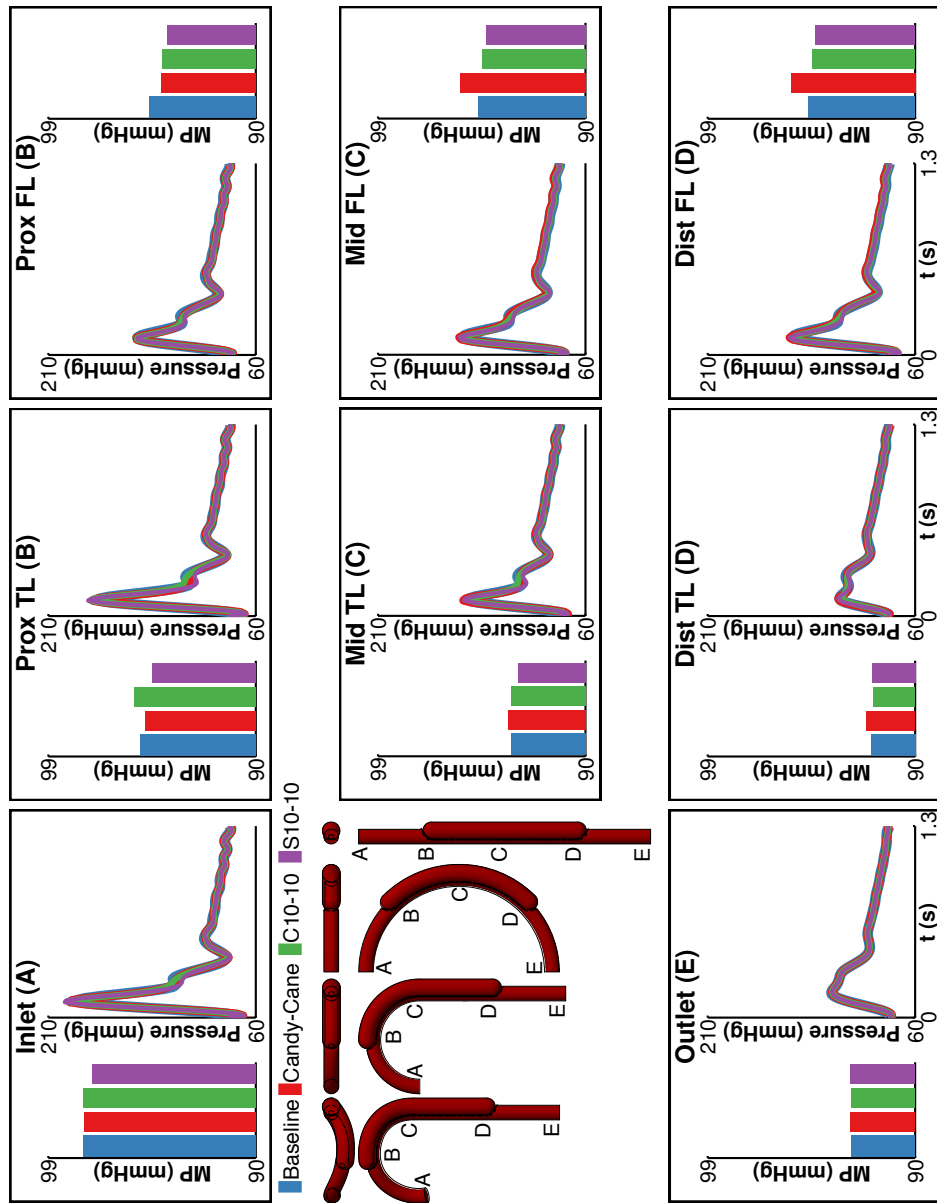


Figure 4.11: Anatomical risk factors in idealised models study: Impact of curvature *Left-middle* Schematic of the baseline, candy-cane, *C10-10* and *S10-10* models. Numerical annotations on models indicate tear size (mm). Plots of pressure against time and MP (mmHg) along the TL and FL and at the inlet and outlet are shown in the panels. The designations A-E correspond to the location under consideration.

tears.

Pressure

Both models showed similar **PP** and **MP** trends in **TL** and **FL** (Figure 4.12). The *C10-10-in* model showed larger inlet pulse (7.5 %) and **MP** (0.4 %) compared to the *C10-10* model. *C10-10-in* showed slightly larger gradients in **TL PP** (67 % drop) relative to *C10-10* (65 % drop). The *C10-10-in FL* showed a 4% higher **PP** and virtually identical **MP**.

Mean flow and velocities

A 80/20 % flow split between **TL** and **FL** was found in both models (Table 4.4). Mid-**TL** and **FL** velocities were 4 % faster and 15 % slower respectively in the *C10-10-in* model. Peak systolic tear velocities were 4 % larger in the *C10-10-in* model (Table 4.5).

In summary, **FL** location in the aortic curvature did not have a large significant impact on the haemodynamics. There was however a trend of larger **PP**, **MP** and tear velocities when the **FL** was located at the inner curvature. Similar patterns were found for models with 4 mm connecting tears.

4.2.4 Impact of tear size - proximal and distal tears of equal size

We investigated circular tears with diameters of 4, 10, and 20 mm both proximally and distally with the straight dissection geometry.

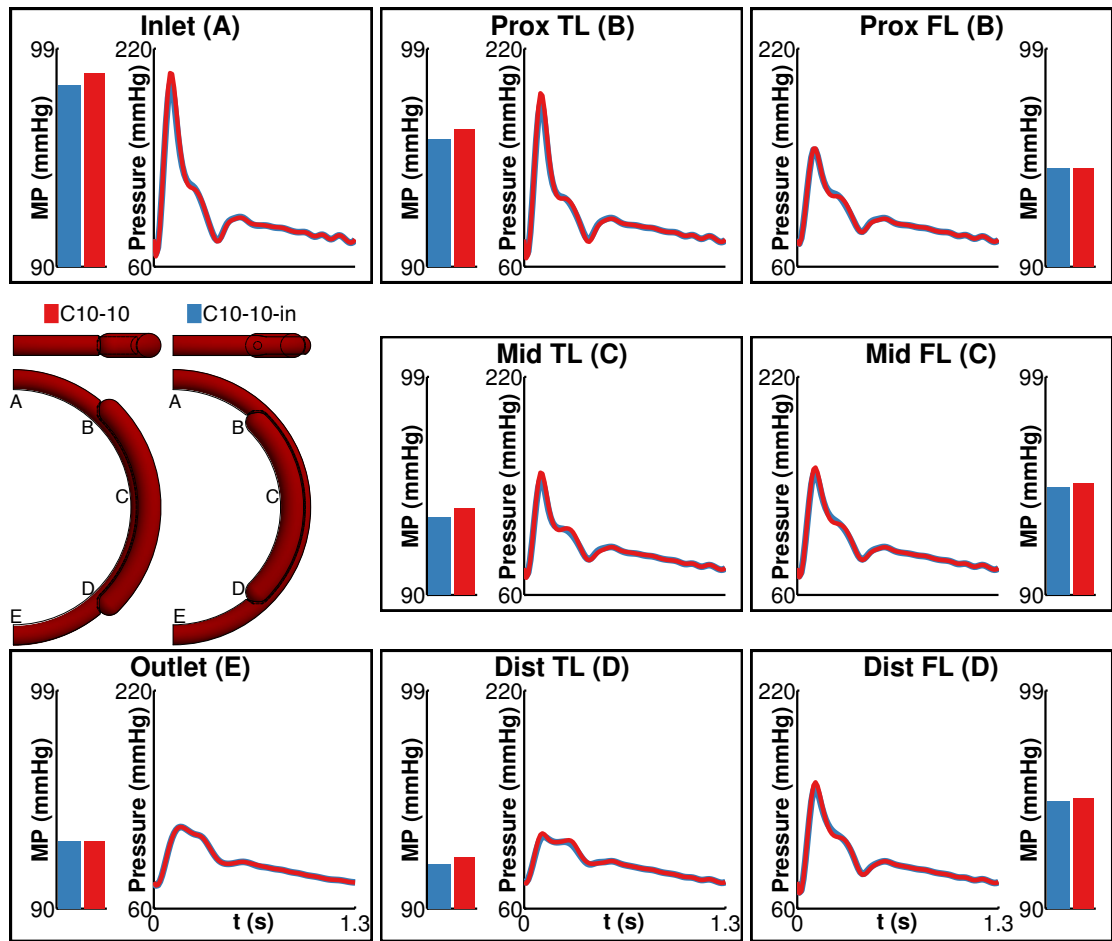


Figure 4.12: Anatomical risk factors in idealised models study: Impact of FL location relative to aortic curvature *Left-middle* Schematic of the *C10-10-in* and *C10-10* models. Numerical annotations on models indicate tear size (mm). Plots of pressure against time and MP (mmHg) along the TL and FL and at the inlet and outlet are shown in the panels. The designations A-E correspond to the location under consideration.

Pressure

Inlet **PP** and **MP** were greatly affected by tear diameter. Compared to the 20 mm tear model, the 4 mm model had larger inlet **PP** (176 %) and **MP** (7 %) (Figure 4.13). The **MP** and **PP** gradient in the **FL** was smaller than in the **TL** for all models. The 4 mm tear case had the largest **PP** and **MP** in the **FL**.

Mean flow and velocities

Flow splits between **TL** and **FL** were greatly affected by tear size: 95/5 %, 81/19 % and 33/67 % **TL FL** ratios were obtained for the 4, 10, and 20 mm tear models, respectively (Table 4.4). Mid-**FL** velocities were largest in the 20 mm tear model. Conversely, the 4 mm tear model showed the largest **TL** velocities. The 20 mm tear model showed the smallest peak systolic tear velocities (3 times slower than the 4 mm tear model) (Table 4.5).

In summary, large tear size decreased haemodynamic differences between **TL** and **FL**, and resulted in smaller inlet **MP** and **PP**.

4.2.5 Impact of the tear size - proximal and distal tear of different sizes

We investigated haemodynamics in four straight models with combinations of different proximal and distal tear sizes of 4 and 10 mm. These models are referred to as: *S4-4*, *S4-10*, *S10-4* and *S10-10*.

Pressure

We adopted the *S10-10* and *S4-4* models as references and we investigated the impact of increasing or decreasing proximal and distal tear sizes (Figure 4.14).

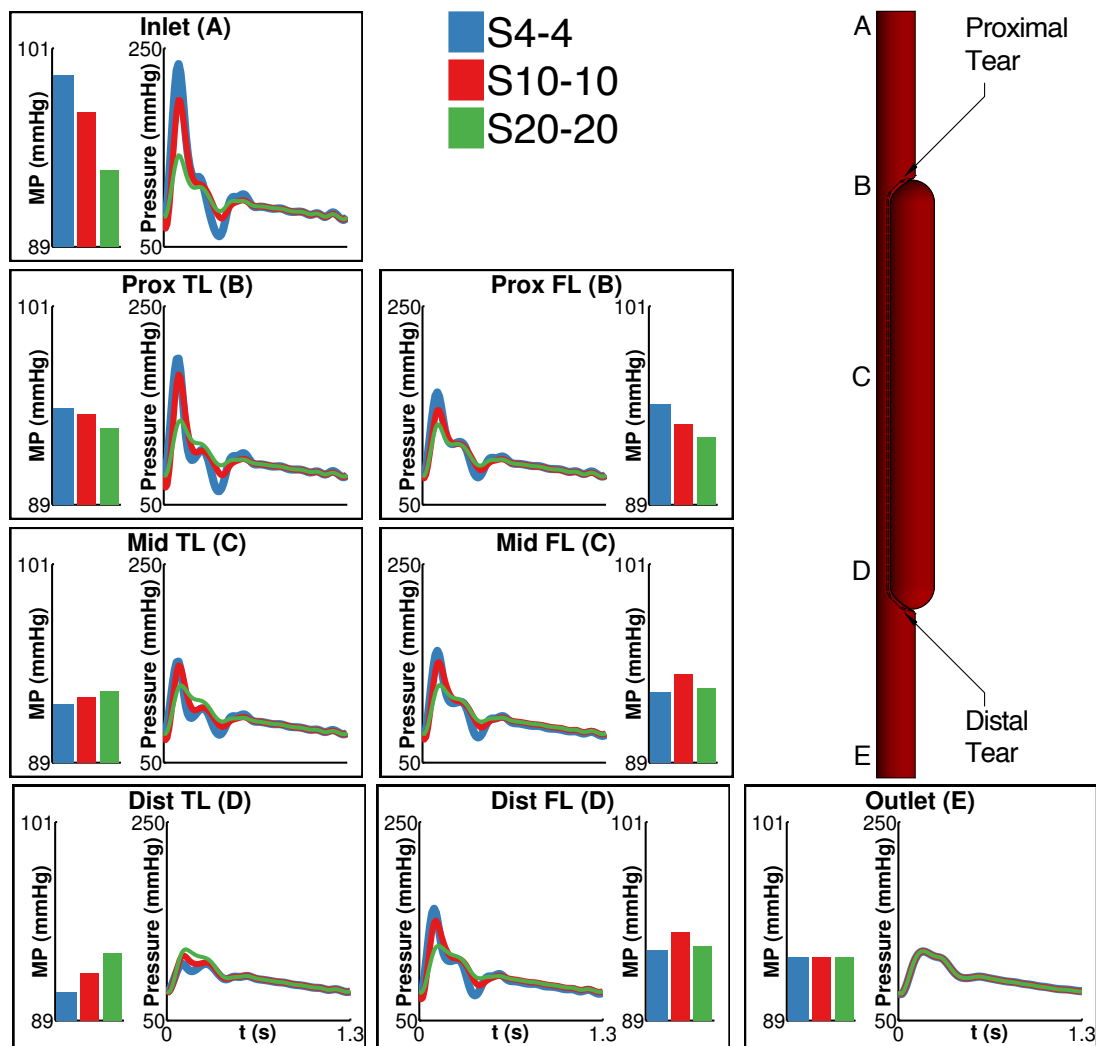


Figure 4.13: Anatomical risk factors in idealised models study: Impact of tear size - proximal and distal tears of equal size *Top-right* Schematic of the S_{4-4} , S_{10-10} and S_{20-20} models. Numerical annotations on models indicate tear size (mm). Plots of pressure against time and MP (mmHg) along the TL and FL and at the inlet and outlet are shown in the panels. The designations A-E correspond to the location under consideration.

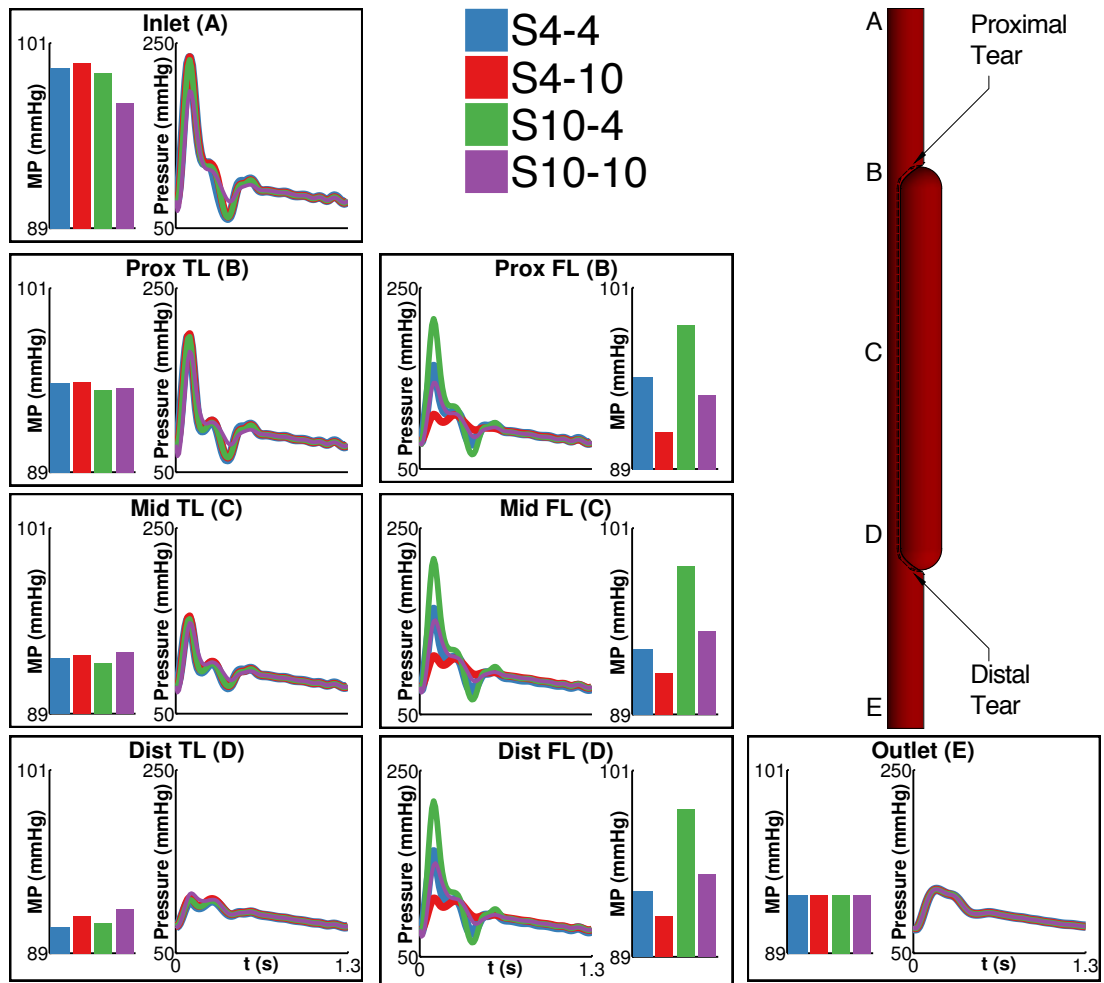


Figure 4.14: Anatomical risk factors in idealised models study: Impact of tear size - proximal and distal tears of different sizes *Top-right* Schematic of the $S4-4$, $S4-10$, $S10-4$ and $S10-10$ models. Numerical annotations on models indicate tear size (mm). Plots of pressure against time and MP (mmHg) along the TL and FL and at the inlet and outlet are shown in the panels. The designations A-E correspond to the location under consideration.

4.2.5.0.4 Changes relative to the *S10-10*

Introducing a single smaller 4 mm tear changed the haemodynamics noticeably: Inlet and TL PP and MP increased. The FL experienced large increases in PP and MP when the size of the distal tear was reduced (*S10-4*). Conversely, FL PP and MP decreased when the proximal tear size was reduced (*S4-10*).

4.2.5.0.5 Changes relative to the *S4-4*

Changing the size of either the proximal or the distal tear did not modify the inlet and TL MP or PP noticeably. However, FL alterations were noticeable; increasing the size of the proximal tear (*S10-4*) increased PP and MP. Conversely, increasing the size of the distal tear (*S4-10*) decreased FL PP and MP.

Mean flow and velocities

TL and FL flow splits were different between all models: the *S10-4* and *S4-10* had identical splits (93/7 %), the *S4-4* had a split of 95/5 %, and the *S10-10* of 81/19 % (Table 4.4). Mid-TL velocities were highest in the *S4-4* model (391 cm s⁻¹), followed by *S4-10* and *S10-4* (381 and 380 cm s⁻¹, respectively). The *S10-10* model showed the smallest TL velocities (283 cm s⁻¹). Large peak systolic velocities were observed at the small tear of the *S10-4* and *S4-10* models (1.4 times faster than the *S4-4* model, Table 4.5).

In summary, larger exit tears decreased FL PP and MP whereas smaller exit tears increased FL PP and MP. Conversely, larger entry tears increased FL PP and MP whereas smaller entry tears decreased FL PP and MP. Large tears tended to decrease tear velocity whereas small tears increased it.

4.2.6 Impact of tear shape

We investigated two models with identical tear areas (0.78 mm^2) but different cross-sectional shapes: Circular with 10 mm diameter versus elliptical with small and large axes of 6 and 17 mm, respectively (Figure 4.15). Results showed negligible differences in pressure, flow and velocity.

4.2.7 Impact of tear patency

We next investigated the impact of tear patency in four models: patent tears *S10-10*, distal tear occlusion (*S10-0*), proximal tear occlusion (*S0-10*) and stented proximal tear (*St-0-10*) (Figure 4.16).

Pressure

Inlet **PP** was highest in models with one occluded tear (*S10-0* or *S0-10*), where the entire flow is forced through the narrow **TL**. The stented model showed the smallest inlet **PP** and **MP**, indicating that occlusion of proximal tear and **TL** expansion produce favourable haemodynamics. Remarkable differences were observed in **FL** pressures. The *S10-0* model showed the largest **PP** and **MP** (167 and 101 mmHg, respectively). The stented model showed the smallest **PP** (31 mmHg) and **MP** (91 mmHg). The stented model also showed a different pressure gradient in **TL MP**: a plateau is apparent in the proximal section of the **TL**, where the lumen size is constant, followed by a modest gradient where the lumen gets narrower distal to the stent.

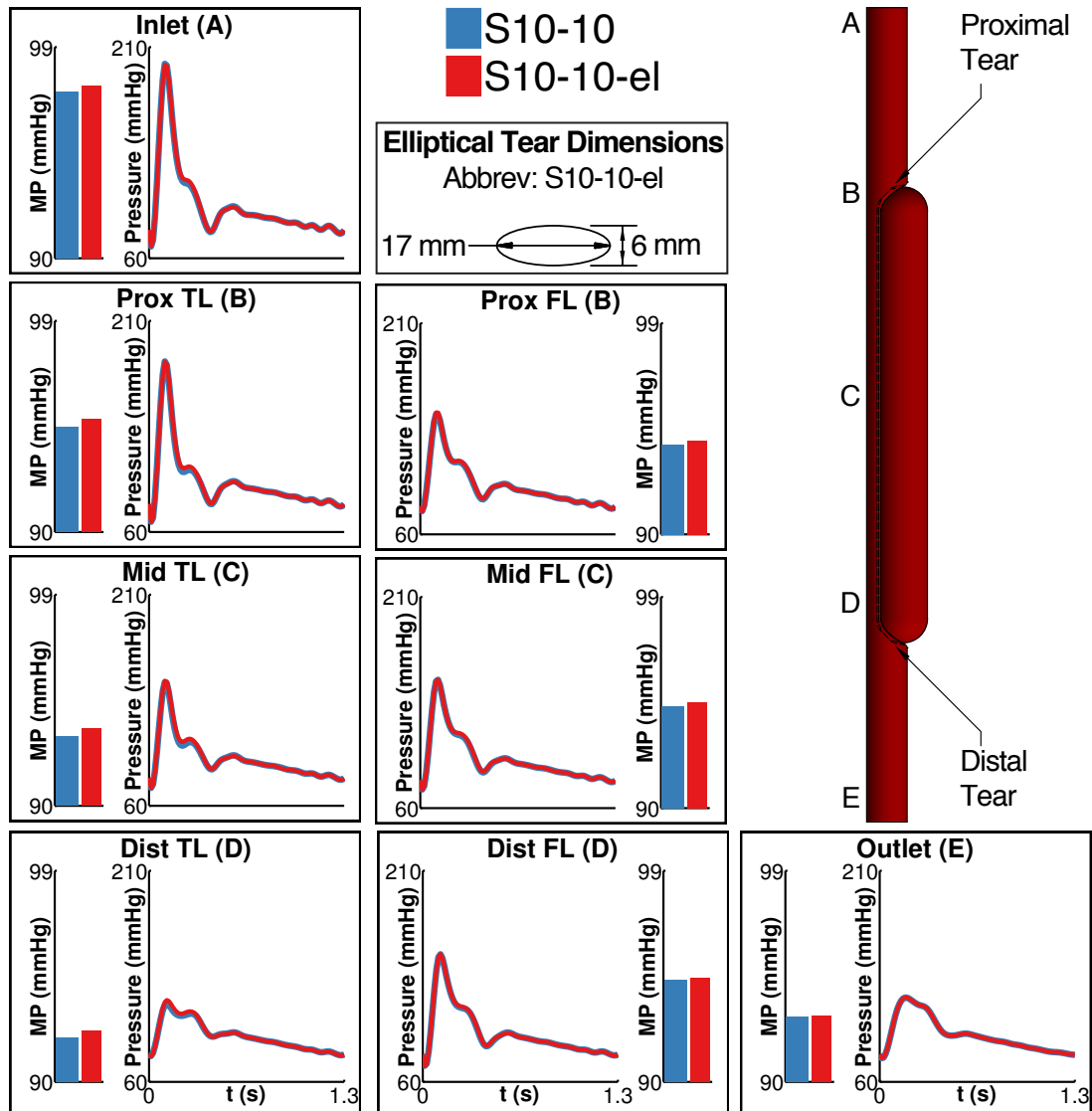


Figure 4.15: Anatomical risk factors in idealised models study: Impact of tear shape *Top-right* Schematic of the *S10-10* straight model with circular tears and *S10-10-el* model with elliptical tears. Numerical annotations on models indicate tear size (mm). Plots of pressure against time and MP (mmHg) along the TL and FL and at the inlet and outlet are shown in the panels. The designations A-E correspond to the location under consideration.

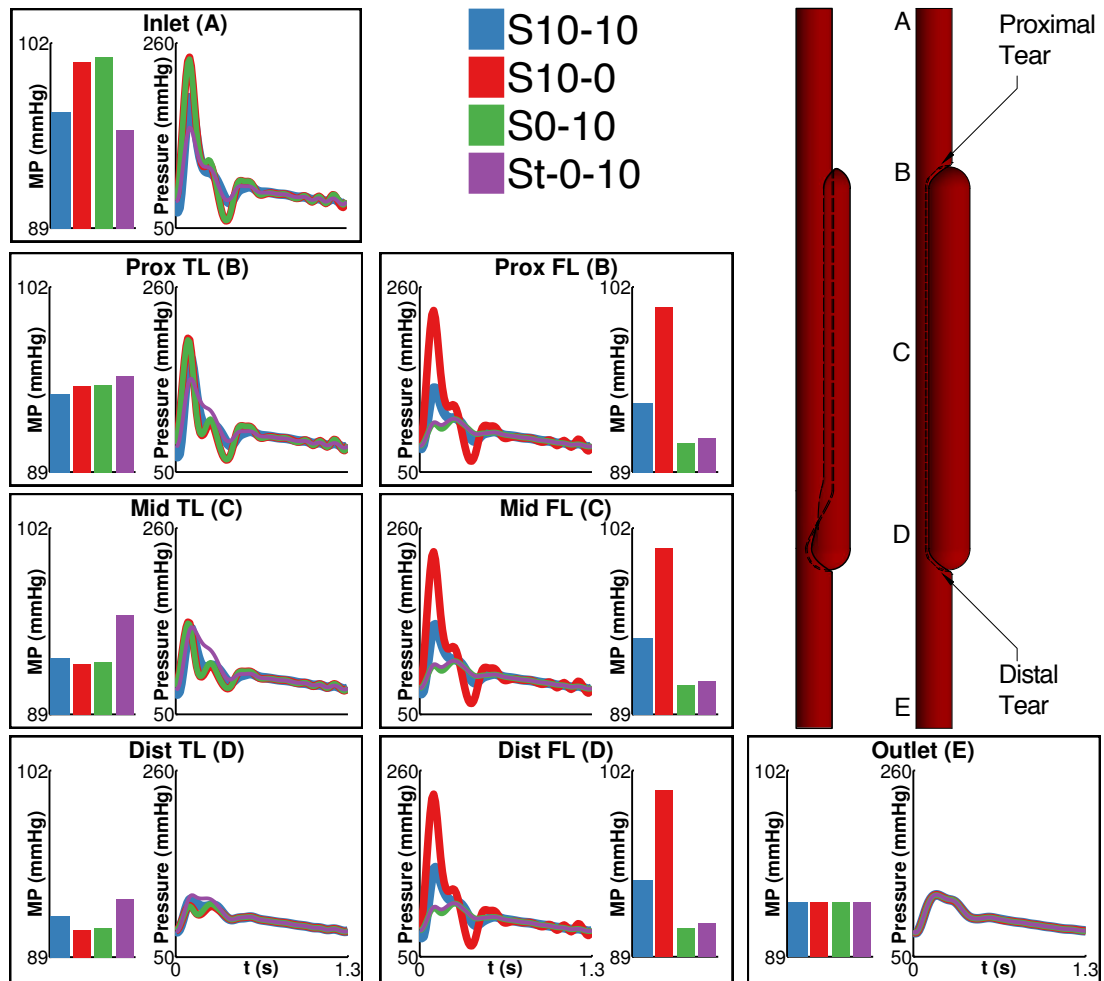


Figure 4.16: Anatomical risk factors in idealised models study: Impact of tear patency *Top-right* schematic of the *S0-10*, *S10-0*, *St-0-10* (Stented) and *S10-10* straight models. Numerical annotations on models indicate tear size (mm). Plots of pressure against time and MP (mmHg) along the TL and FL and at the inlet and outlet are shown in the panels. The designations A-E correspond to the location under consideration.

Mean flow and velocities

All models with an occluded tear showed near zero FL flow (Table 4.4). Models *S0-10* and *S10-0* showed faster mid TL velocity whereas the stented model presented slower mid TL velocity, compared with the *S10-10* (Table 4.5).

In summary, proximal tear occlusion via stenting decreased PP, MP, flow and velocity. Narrowed TL and occlusion of one tear increased PP and velocity in the TL. Distal tear occlusion increased FL PP and MP, and TL velocity.

4.3 Strain quantification via dual phase black blood MRI in healthy and aortic dissection subjects

This section shall firstly give the measured strains for the healthy volunteers and will then present the results for the AD patients. In each case three measures of strain will be examined. Circumferential Strain (E_{Cir}) considers the circumference of the vessel wall measured at each of the seven bifurcation points identified, Longitudinal Strain (E_{Long}) considers the change in the vessel centreline length for the AAo, AA and DA, and Volumetric Strain (E_{Vol}) considers the volume of the AAo, AA and DA (see Figure 4.17 for more information on these locations). E_{Cir} and E_{Long} were calculated using equations 3.7 and 3.7 respectively based on the Green-Lagrange strain formula and E_{Vol} was calculated via the volumetric strain equation 3.9.

4.3.1 Measurement locations

The following key branching points were identified for the systolic and diastolic data sets: distal to the Left Coronary Artery (LCoA), Proximal to the Innominate Artery (InoA)

(PInoA), distal to the Left Subclavian Artery (LSCA), and 5th Intercostal Artery (IcoA). These planes were selected as they were both easily identifiable on the image data and they allowed the consideration of specific portions of the aorta, namely that of the the Ascending Aorta (AAo) (the portion of the aorta from the plane distal to the LCoA to PInoA), Aortic Arch (AA), the portion of the aorta from PInoA to the plane distal to the LSCA) and the descending aorta Descending Aorta (DA), the portion of the aorta from the plane distal to the LSCA to the 5th IcoA).

Other branching points and corresponding planes were also identified where possible. These were Distal to the InoA (DInoA), distal to the LCCA and proximal to the 1st IcoA. One of the volunteers and AD patients had a bovine aortic arch whereby the InoA and the LCCA share a common origin. The DInoA could therefore not be identified in these two subjects. A schematic showing the defined planes and regions is shown in Figure 4.17. In the cases of dissection, the TL and FL were considered separately.

4.3.2 Healthy subjects

E_{Cir} , E_{Long} , and E_{Vol} were calculated in a number of key locations using the fixed material points identified where the branching vessels furcate. Figure 4.18 shows the measurements collected for a single volunteer. *Left* shows the diastolic and systolic aortic configurations and gives the volume and corresponding centreline length values for each section. *Right* shows the gradient image reslice acquired via black blood MRI at each identified branching location and corresponding contour and contour circumference. The calculated percentage strains for each measure of strain (E_{Cir} , E_{Long} and E_{Vol}) are given. A similar distribution of strains was observed for the remaining healthy subjects. Top of Figure 4.19 shows the mean E_{Vol} for this population. The largest strains (+29.0 %) were seen in the AA followed by the AAo (+24.8 %) and E_{Vol} was lowest in the DA (+16.7

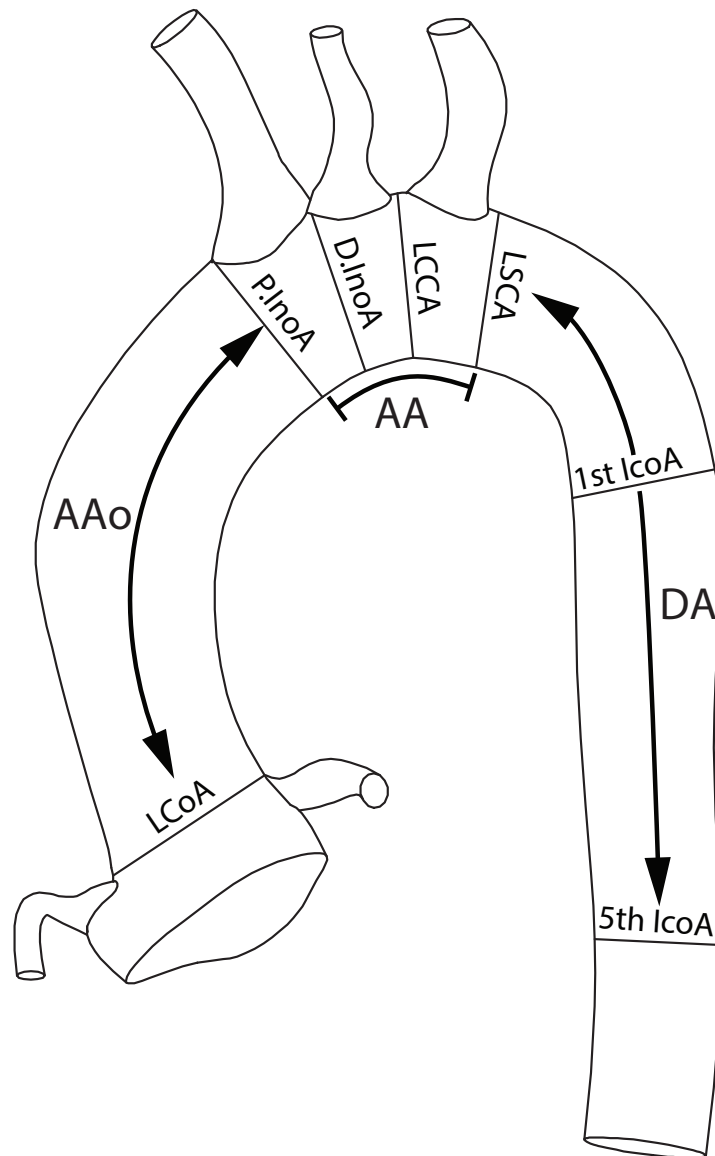


Figure 4.17: Strain quantification study: Selected material planes in the aorta. For each subject the LCoA, P.inoA, D.inoA, LCCA, LSCA, and 1st and 5th ICoA were identified. The AAO was defined as the region between LCoA and P.inoA, AA between P.inoA and LSCA and DA between LSCA and the 5th ICoA.

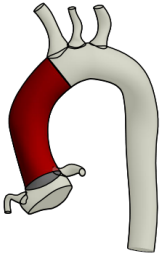
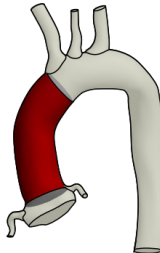
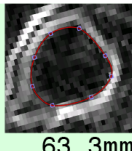
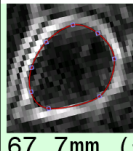
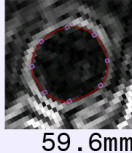
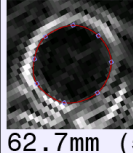
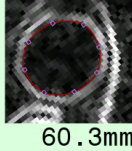
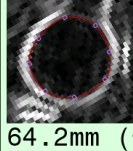
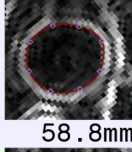
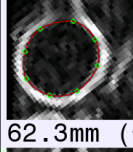
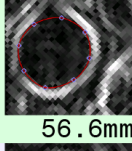
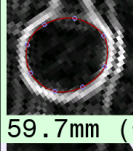
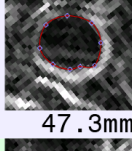
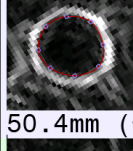
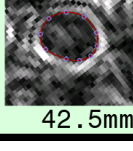
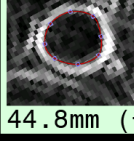
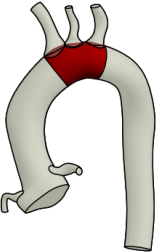
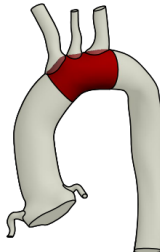
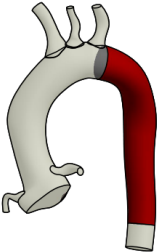
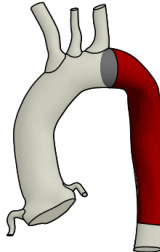
Diastole	Systole	Diastole	Systole
 <p>AAo Vol 15.6ml CL 59.4mm</p>	 <p>AAo Vol 17.5ml (+12.1%) CL 59.2mm (-0.3%)</p>	<p>LCoA</p>  <p>63.3mm</p>  <p>67.7mm (+7.2%)</p>	
		<p>P.InoA</p>  <p>59.6mm</p>  <p>62.7mm (5.3%)</p>	
		<p>D.InoA</p>  <p>60.3mm</p>  <p>64.2mm (+6.7%)</p>	
		<p>LCCA</p>  <p>58.8mm</p>  <p>62.3mm (+6.2%)</p>	
		<p>LSCA</p>  <p>56.6mm</p>  <p>59.7mm (+5.8%)</p>	
		<p>1st IcoA</p>  <p>47.3mm</p>  <p>50.4mm (+6.8%)</p>	
		<p>5th IcoA</p>  <p>42.5mm</p>  <p>44.8mm (+5.7%)</p>	
 <p>AA Vol 6.1ml CL 23.7mm</p>	 <p>AA Vol 7.8ml (+27.5%) CL 28.2mm (+20.5%)</p>		
 <p>DA Vol 16.0ml CL 95.6mm</p>	 <p>DA Vol 17.0ml (+6.2%) CL 93.8mm (-1.9%)</p>		

Figure 4.18: Strain quantification study: Typical aortic strain measures in a healthy volunteer. *Left:* Segmentations and the calculated volume (*Vol*) and centreline length (*CL*) and corresponding strains in systole for the AAo, AA and DA. *Right:* Gradient image reslice at furcation points showing vessel contour, circumference and E_{Cir} .

%).

When considering E_{Long} (centre of Figure 4.19), the largest strain value of +13.2 % was observed in the AA while the AAo and DA saw a E_{Long} of +4.2 % and -1.2 % respectively. Mean E_{Cir} (bottom of Figure 4.19) was generally smaller at distal locations. The highest mean value (+10.4 %) was observed in the LCoA and the lowest at the 5th ICoA (+6.3 %). Average values for the AA ranged between +9.0 % and +8.3 %.

4.3.3 Aortic dissection patients

As each AD is unique, this section will consider the strains for each AD patient individually.

AD patient A

The geometry and results for patient A are shown in Figure 4.20. Volumetric and longitudinal deformations are detailed on the left panels while the right panel show the vessel lumen and circumference at each branching location in systole and diastole. Values of strain are given in a percentage value.

Patient A presented with a repaired TAAD with residual TBAD component and experienced E_{Vol} of +32.7 % in the AAo, +11.2 % in the TL and +7.6 % in the FL in the AA, and a relatively large strain of +44.2 % in the TL of the DA and a compressive (negative) strain of -7.4 % in the FL.

E_{Long} in the AAo (+13.6 %) was larger than that the mean strain observed in the healthy subjects. A compressive E_{Long} was observed in the AA (-5.1 % in the TL and -5.7 % in the FL). In the DA, the FL experienced a tensile (positive) E_{Long} (+11.0 %) while the TL experienced a compressive strain (-1.2 %).

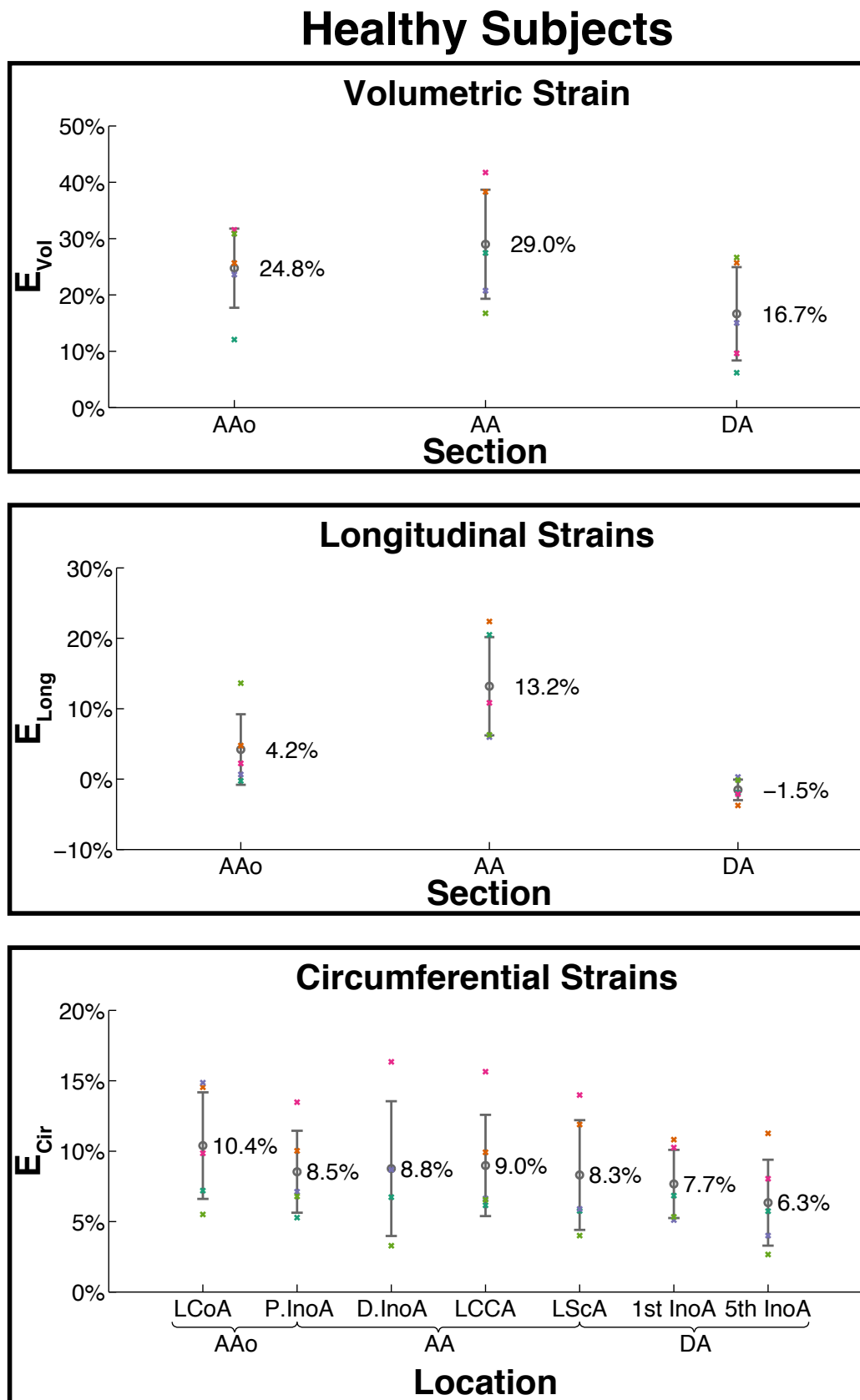


Figure 4.19: Strain quantification study: Healthy subject strains. Top: Volumetric Strain (E_{Vol}), centre: Longitudinal Strain (E_{Long}), Bottom: Circumferential Strain (E_{Cir}). Grey bars show the standard deviation, mean values are indicated by the grey circles. Individual data are indicated by the coloured 'x's. (n=5).

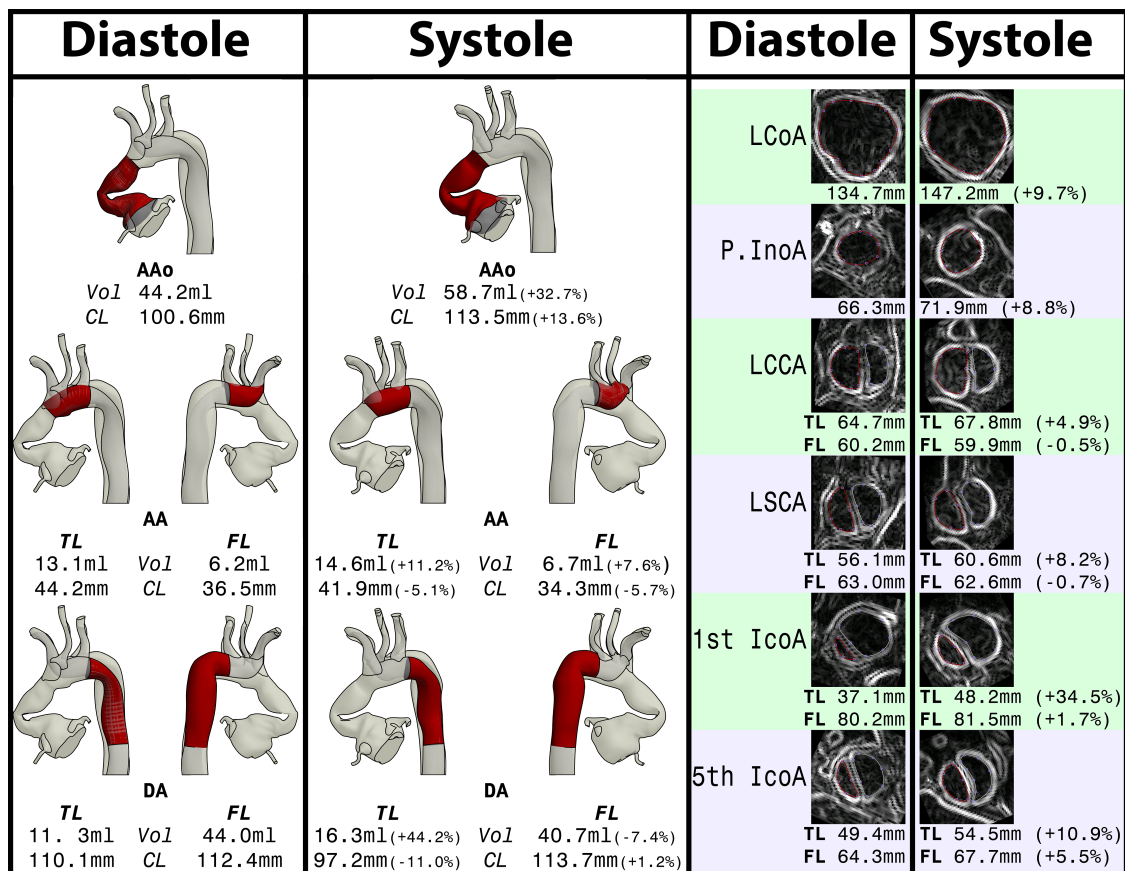


Figure 4.20: Strain quantification study: Aortic strain in dissected patient A. *Left:* Segmentations and the calculated volume (*Vol*) and centreline length (*CL*) and corresponding strains in systole for the **AAo**, **AA** and **DA**. *Right:* Gradient image reslice at furcation points showing vessel contour, circumference and E_{Cir} . Calculations are shown for **TL** and **FL** separately.

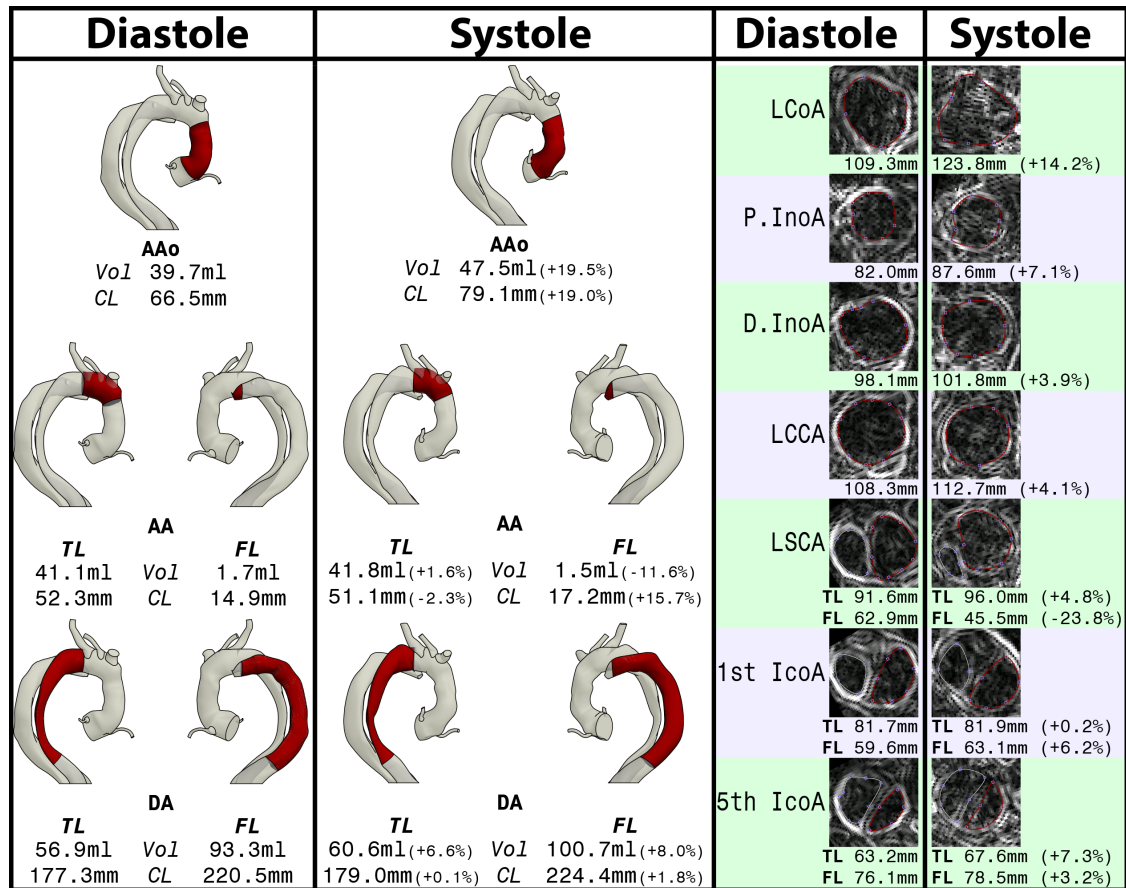


Figure 4.21: Strain quantification study: Aortic strain in dissected patient B. Vol) and centreline length (CL) and corresponding strains in systole for the AAo, AA and DA. Right: Gradient image reslice at furcation points showing vessel contour, circumference and E_{Cir} . Calculations are shown for TL and FL separately.

E_{Cir} was found to be within the same range as the healthy subjects in the AAo. In the dissected regions of the AA and DA large E_{Cir} were observed, particularly at the 1st IcoA where TL strain was found to be +35.5 %.

AD patient B

The geometry and results for patient B are shown in Figure 4.21. Volumetric and longitudinal deformations are detailed on the left while the right shows the vessel lumen and gives the circumference at each branching location in systole and diastole. Values of strain are given in a percentage value.

Patient B presented with a repaired TAAD with residual TBAD component and suspec-

ted connective tissue disorder and, similar to patient A, also demonstrated significantly greater E_{Vol} in **AAo** (+19.5 %) than in **AA**, where a tensile strain was seen in the **TL** (+1.6 %) and a compressive strain in the **FL** (-11.6 %). E_{Vol} in the **DA** was positive (**TL**: +6.6 % **FL**: +8.0).

The E_{Long} in the **AAo** was +19.0 %. In the **AA**, a compressive E_{Long} was seen in the **TL** (-2.3 %) and a tensile strain in the **FL** (+15.7 %) (although it should be noted this section of **FL** only represents 3.5 % of the total **AA** volume in systole). In the **DA** the **TL** E_{Long} was negligible (+0.1 %) while the **FL** saw +1.8 % strain.

E_{Cir} observed in the **AA** at **DInoA** (3.9 %) and **LCCA** (4.1 %) are significantly lower than those seen in the **AAo** at **LCoA** (14.2 %) and **PInoA** (7.1 %). The **TL** expansion in systole was seen to have a significant influence on the **FL**, causing it to collapse in places such as at the **LSCA** where a large compressive E_{Cir} (-23.8 %) was observed in the **FL**.

4.4 Impact of septum distensibility on simulated haemodynamics using a LPN

In each of the **CFD** simulations presented thus far compliance has not been simulated in the 3D domain. It is thought that this explains the discrepancies seen in the results of the primary patient specific study when comparing the peak-to-peak values of flow between the simulation and **2D PC-MRI** data. To try and assess the effect of compliance in the **AD**, equivalent **LPN** models of the 3D domain were created with lumina of different stiffness, one very stiff, and the other with compliance values comparable to aortic tissue. This section presents the results of these simulations and compares them to the equivalent 3D patient specific model and **PC-MRI** flow data.

Figure 4.22 shows the **LPN** circuit constructed to model the **AD** of the primary patient

specific study. It consists of RCR Windkessels representing the head and neck vessels and the abdominal and iliac vessels. The properties of each RCR were calculated to achieve similar flow and pressure wave forms as seen in the 3D patient specific study.

In the LPN, each lumina was modelled as a 0D circuit with a hydraulic resistance, R_{Lumen} , fluid inertia, L_{Lumen} , and compliance C_{Lumen} to represent the luminal and septum distension. The values for these components were estimated from the the AD CAD model from the primary patient specific study with following set of equations:

$$R_{Lumen} = \frac{8\mu l\pi}{a^2} \quad (4.1)$$

$$L_{Lumen} = \frac{\rho l}{a} \quad (4.2)$$

$$C_{Lumen} = \frac{3\pi r^3}{2Eh} \quad (4.3)$$

where a , the cross-sectional area of the lumen was estimated by taking the mean areas of the contours used to create each lumen (as described in Section 3.1.2). l , the length of each lumen, was estimated by interpolating a cubic spline using the centroids of each contour. Values for viscosity μ and density ρ were the same as those for the patient specific simulation (i.e 4 mPa s and 1.06 g ml⁻³ respectively). The resistance for the entry and exit tears $R_{Tear} = 8\mu h\pi/a^2$ was also calculated where h is the septum thickness. The compliance was varied by altering the Young's modulus, E in equation 4.3. To simulate the stiff condition E was set to 400×10^{11} Pa, a Young's modulus higher than diamond, and 400×10^3 Pa for the compliant case which is a typical value for aortic tissue [164].

Figure 4.23 shows the results for both stiff and compliant 0D simulations. The dashed blue line shows the 0D results of the stiff lumina ($E = 400 \times 10^{11}$ Pa) and the solid black lines shows the 0D results when a physiological stiffness is applied to the lumina

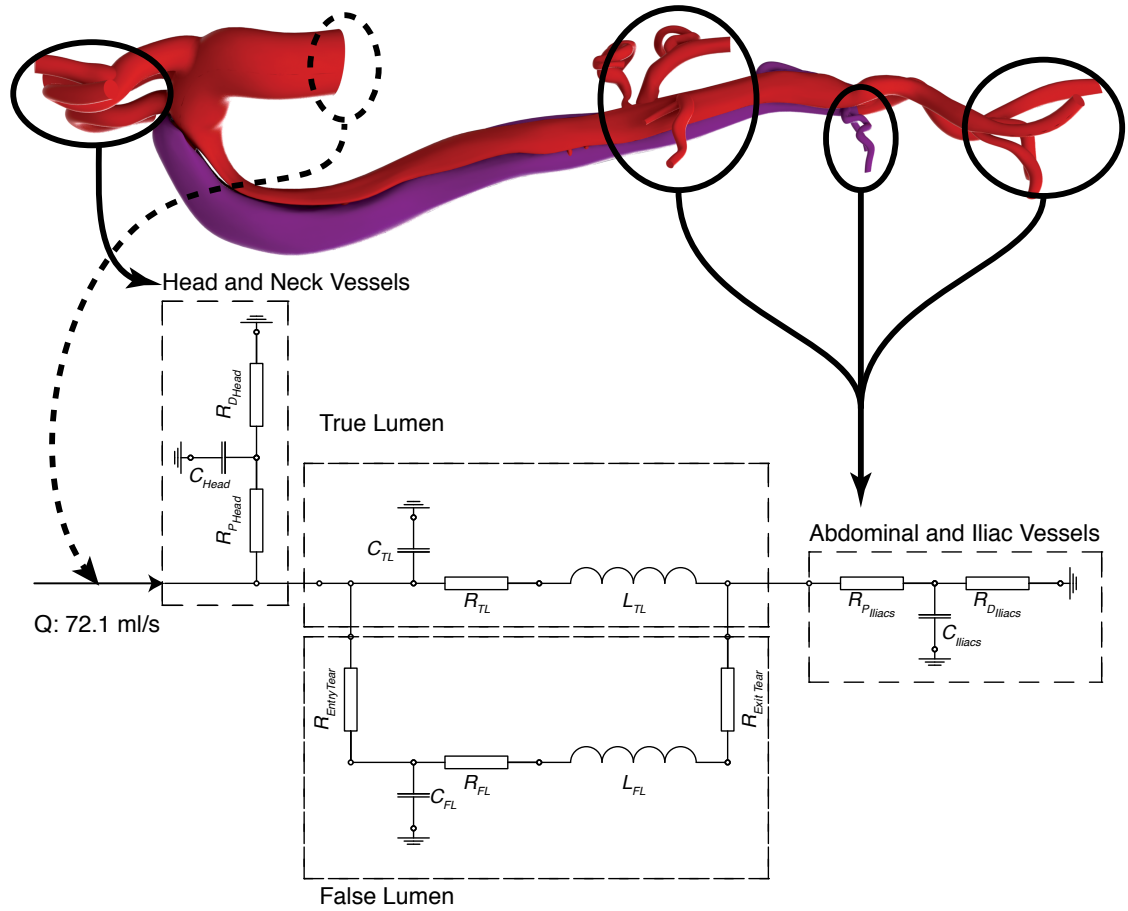


Figure 4.22: 0D AD Study: 0D AD Circuit 0D circuit representing the patient specific AD. The AD is separated into the TL and FL. RCR models are included to represent the head and neck vessels and to represent the the abdominal and iliac vessels. Each of the components is described in more detail in Table 4.6.

Table 4.6: 0D AD Study: Component description

Component	Location	Value
$R_{P_{Head}}$	Head and neck vessels	$281.7 \text{ g cm}^{-4} \text{ s}^{-1}$
C_{Head}	Head and neck vessels	$3.0 \times 10^{-4} \text{ cm}^4 \text{ s}^2 \text{ g}^{-1}$
$R_{D_{Head}}$	Head and neck vessels	$5352.4 \text{ g cm}^{-4} \text{ s}^{-1}$
$R_{P_{iliacs}}$	Abdominal and iliac vessels	$134.2 \text{ g cm}^{-4} \text{ s}^{-1}$
C_{iliacs}	Abdominal and iliac vessels	$6.3 \times 10^{-4} \text{ cm}^4 \text{ s}^2 \text{ g}^{-1}$
$R_{D_{iliacs}}$	Abdominal and iliac vessels	$2550.3 \text{ g cm}^{-4} \text{ s}^{-1}$
R_{TL}	True lumen	$29.4 \text{ g cm}^{-4} \text{ s}^{-1}$
L_{TL}	True lumen	35.1 g cm^{-4}
C_{TL}	True lumen	6.3×10^{-5} or $6.3 \times 10^{-13} \text{ cm}^4 \text{ s}^2 \text{ g}^{-1}$
R_{FL}	False lumen	$1.5 \text{ g cm}^{-4} \text{ s}^{-1}$
L_{FL}	False lumen	8.2 g cm^{-4}
$R_{EntryTear}$	False lumen	$4.4 \text{ g cm}^{-4} \text{ s}^{-1}$
$R_{ExitTear}$	False lumen	$17.4 \text{ g cm}^{-4} \text{ s}^{-1}$
C_{FL}	False lumen	6.5×10^{-4} or $6.5 \times 10^{-13} \text{ cm}^4 \text{ s}^2 \text{ g}^{-1}$

($E = 400 \times 10^3$ Pa).

The simulated 0D TL and FL results were compared to both the rigid 3D simulation pressure and flow results (dash-dot pink line) and the 2D PC-MRI flow data (dotted orange line) acquired in the descending thoracic aorta from the primary patient specific study (see Section 4.1) upon which the 0D study is based. As the 0D model only includes the primary entry and exit tears, the 3D CFD results shown here are from the minimal tears data set which does not include any secondary tears.

Decreasing the stiffness of the lumina (increasing compliance) led to a drop in the peak-to-peak range (PPr) of both flow and pressure but had little effect on mean values. In the TL the flow PPr dropped from 65.7 to 42.6 ml s⁻¹ (35.1% drop) and the pressure PPr dropped from 51.0 to 31.5 mmHg (38.2 % drop). The FL demonstrated a drop in flow PPr from 284.7 to 169.3 ml s⁻¹ (40.5 % drop) and pressure from 51.5 to 31.8 mmHg (38.2 % drop). At the outlets the increased compliance affected the flow and pressure waveforms, decreasing the PPr, and reducing the MP, but the mean flow to each outlet remained relatively unaffected.

Comparing the 0D simulation results to the rigid 3D CFD simulation, while it is not possible to replicate the complex pressure and flow patterns of such a geometry in a 0D setting, similar mean flows were obtained in the ascending vessels (3D:20 ml s⁻¹, 0D:23 ml s⁻¹) and the abdominal and descending vessels (3D:52 ml s⁻¹, 0D:49 ml s⁻¹). Comparable mean flow distributions are also seen for the TL (3D:25 ml s⁻¹, 0D:22 ml s⁻¹) and FL (3D:27 ml s⁻¹, 0D:27 ml s⁻¹). The 3D simulation displayed a PPr of flow of 96.9 ml s⁻¹ in the TL and 270.9 ml s⁻¹ in the FL. Of the two 0D cases run, the case with high stiffness (low compliance) was found to have a better comparison with the rigid 3D simulation, showing flow PPrs of 65.7 ml s⁻¹ in the TL (-32.1 %) and 270.9 ml s⁻¹ in the FL (+5.1 %). The pressure observed in the TL and FL had comparable mean values in

all simulations, with the largest differences between the 3D simulation and the compliant 0D simulation being 3.9 % (seen in the TL). The PPr of pressure of the 3D simulation was closer the stiff 0D simulation than compliant 0D simulation.

The 0D simulation results were also compared to the 2D PC-MRI data. The distribution of mean flows to the TL (8.0 ml) and FL (45.5 ml) was not as comparable to that of the 0D or 3D simulations. One reason for this may be that the 3D and 0D simulations did not include any secondary connecting tears which have been seen (Figure 4.9) to have a significant influence on the haemodynamics of the dissection. Considering flow PPr, the 2D PC-MRI data were found to have a PPr of 23.3 ml s^{-1} in the TL and 152.2 ml s^{-1} in the FL. Of the two 0D cases run, the case with low stiffness (high compliance) was found to have a better comparison with the 2D PC-MRI data, showing PPr of flow of 42.6 ml s^{-1} in the TL (+82.8 %) and 169.3 ml s^{-1} in the FL (+11.2 %).

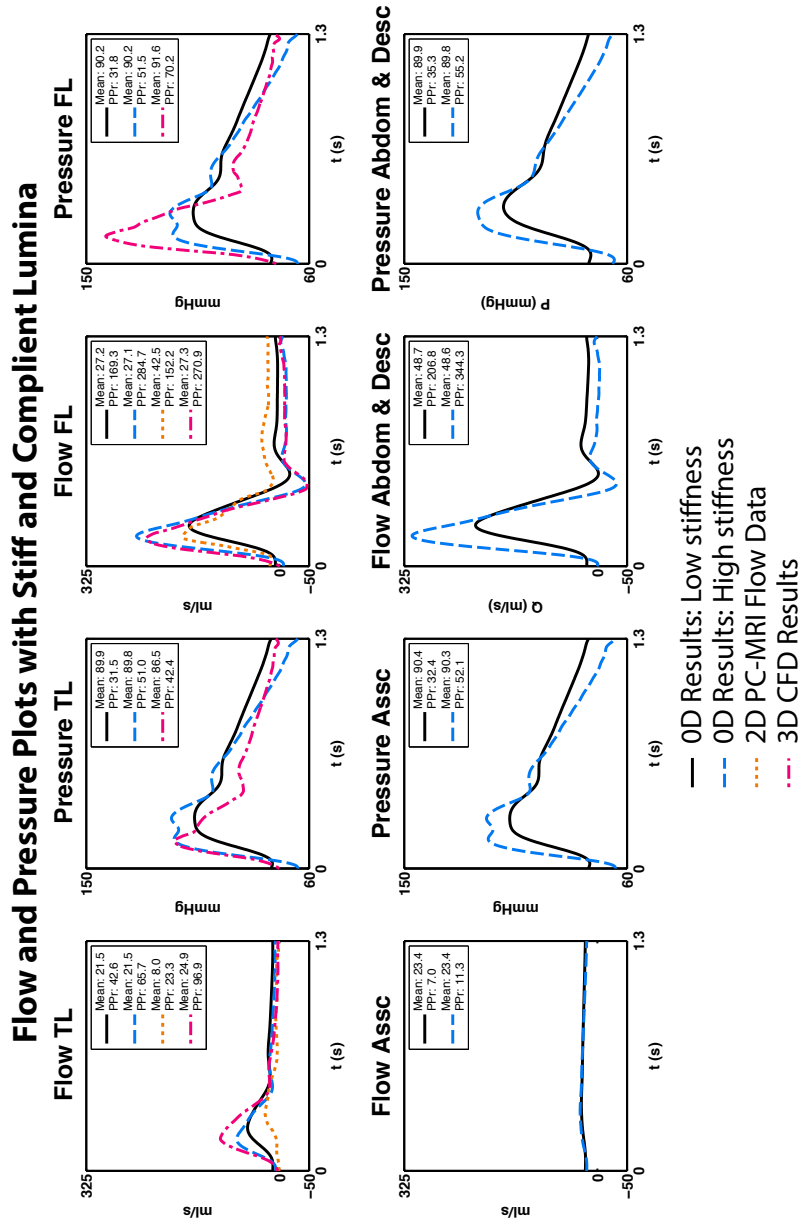


Figure 4.23: Impact of septum distensibility on simulated haemodynamics: pressures and flows to the ascending vessels, the abdominal and descending vessels and in the TL and FL. Shown in solid black are the results of the 0D simulation with low luminal stiffness (Young's modulus, $E = 400 \times 10^3$ Pa), dashed blue lines are the 0D results with high luminal stiffness ($E = 400 \times 10^{11}$ Pa), dashed pink the 3D CFD results in the DA and in dotted orange are the 2D PC-MRI data (note, no patient specific pressure data exists). Mean and peak-to-peak range (PPr) values are also given.

5

DISCUSSION

Here, a full discussion and interpretation of the results of the previous chapter will be presented. The chapter is subdivided into four sections, each corresponding to the individual studies.

Contents

5.1	Primary patient specific study	108
5.2	Computational Study of Anatomical Risk Factors	113
5.3	Strain quantification via dual phase black blood MRI	117
5.4	Impact of septum distensibility on simulated haemodynamics using a LPN	122
5.5	Potential of AD modelling	123

5.1 Primary patient specific study: Multi-modality image-based computational analysis of haemodynamics in aortic dissection

In this study, we used multiple sources of medical image data (CT; 2D PC-MRI velocity data in the TL and FL and ascending aorta; and 4D PC-MRI in the thoracic aorta) to inform our computational analysis of AD. The combination of highly resolved CT and 2D PC-MRI data has allowed, for the first time, the creation of a highly detailed, multi-branched geometric model of the dissected morphology featuring 17 branches. The 2D PC-MRI flow data were used to tune both the inflow and outflow reduced-order models coupled to the 3D domain, and to validate the simulation results.

Building a geometric model of the aortic vasculature involves segmenting the image data to obtain the volume of interest where the blood flow simulation is to be performed. There are several powerful 3D automatic and semiautomatic segmentation tools such as Seg3D [18], MITK [160] and ITK-Snap [166] to name a few which can perform this task with relatively little effort from the user. However, automatic segmentation may be difficult to apply on images with low resolution or poor signal-to-noise ratio, circumstances unfortunately present in AD imaging. Indeed, the relative thinness and motion of the septum often make it difficult to delineate the boundaries between TL and FL. It was found that, after trying several different tools, automatic 3D segmentation methods produced numerous artefacts in the form of "bleeds" between the two lumina (see Figure 5.1). A considerable amount of time was spent trying to manually correct these artefacts, a non-practical task as it was significantly more time-consuming than the initial segmentation process itself. It was therefore concluded that in cases of AD, a 2D segmentation approach is preferable. This segmentation approach, although requiring a larger degree

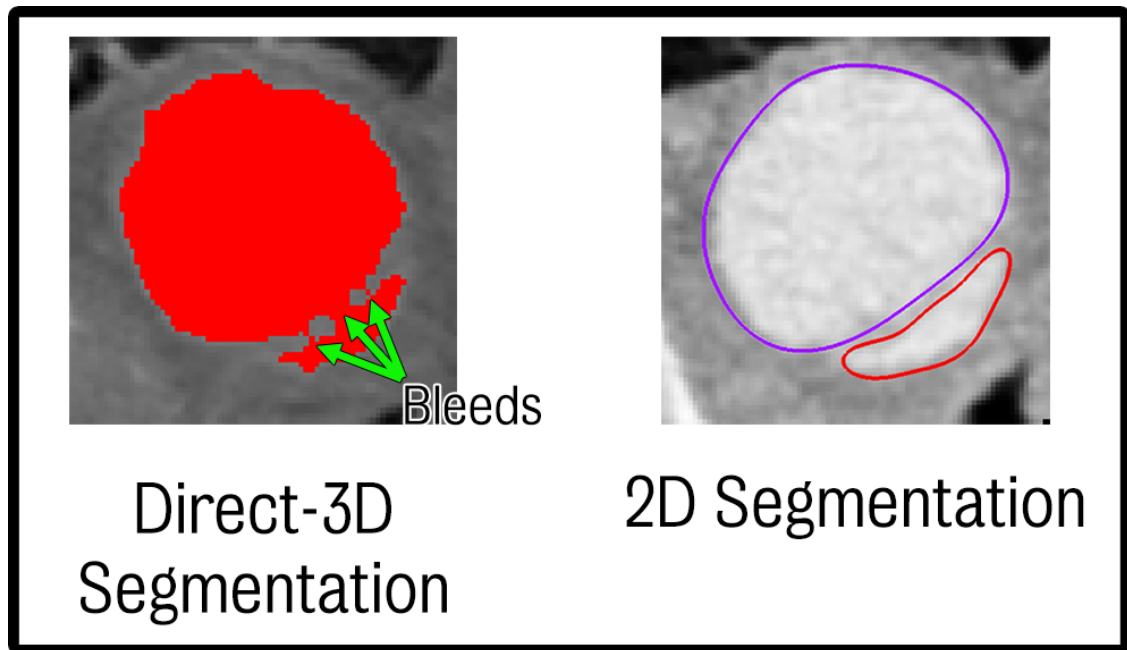


Figure 5.1: Primary patient specific study: Example of direct 3D segmentation (*left*) illustrating typical "bleeds" between the TL and FL through the relatively thin and poorly defined septum. For comparison, a typical 2D segmentation in the same plane is shown (*right*) where contours may be automatically create and corrected manually if necessary.

of user intervention (i.e. it is less automatic), is more robust in situations of poorly defined features in the image data as the lofting method interpolates the surface between each contour which may be defined at locations where said features are clearly visible and also allows for human judgement to be employed in regions where features may be obscure.

Previous CFD studies in AD have been somewhat limited due to the assumptions adopted to determine inflow and outflow boundary conditions. For instance, most studies have used flow data acquired from healthy subjects [144, 15, 2]. AD patients are often prescribed antihypertensive therapies such as beta blockers and morphine sulphate and this may have associated issues. The therapies seek to maintain normal blood pressure, thereby reducing aortic wall stress in dissection patients [34, 36, 103, 93, 21]. However, cardiac output is often also reduced via reduction in left ventricular contractility. Therefore, assuming healthy inflow conditions may overestimate actual inflow conditions in AD patients [15]. This study has used patient-specific data at a number of locations to

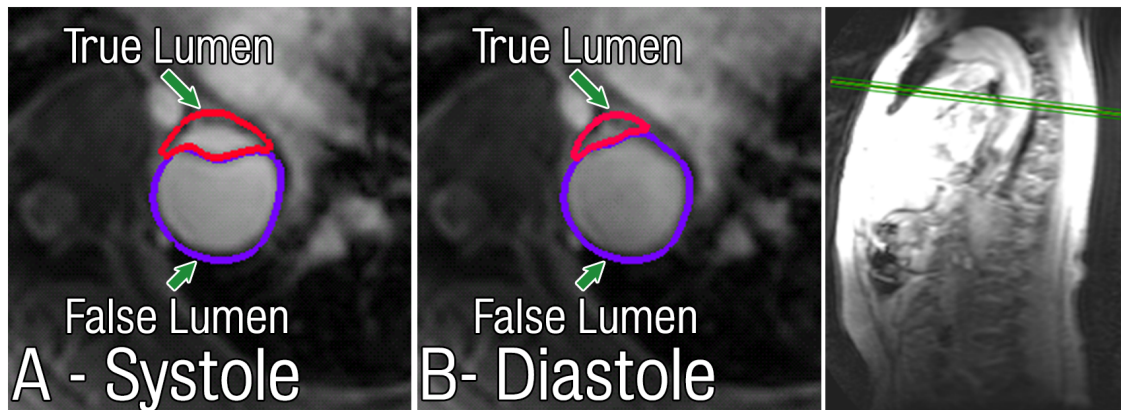


Figure 5.2: Primary patient specific study: 2D PC-MRI showing distention of the AD flap between peak systole (A) and mid-diastole (B).

inform and validate the model. Similarly, with regard to outflow boundary conditions, most studies have either imposed pressure and/or velocities acquired from healthy subjects or have applied zero pressure conditions [144, 70, 15]. In this study, we have used tuned lumped-parameter Windkessel models to represent the resistance and compliance of the distal vasculature.

We performed three investigations with two main overriding objectives: i) to validate our computational results against subject-specific flow data, and ii) to obtain a deeper understanding on the alterations in aortic haemodynamics induced by the AD.

In the first investigation, a comparison between haemodynamics in a subject-specific AD model and a hypothetical baseline normal (undissected) aorta was performed. The undissected model was created by virtually removing the intimal flap of the dissected aorta, assuming that no remodelling (e.g. FL expansion) had occurred due to the acute nature of the AD. Assuming identical cardiac output for both the dissected and undissected models, our results show significant differences between the models and give an estimation of the haemodynamic changes that occurred for this patient with the onset of the AD. There is an increase in the ascending aortic PP in the dissected model (159/71 mmHg, PP 88 mmHg) compared to the undissected model (146/74 mmHg, PP 72 mmHg). These differences are consistent with the larger afterload induced by the dissection septum com-

pared to the baseline model. In the dissected case, the **TL** exhibits a much larger pressure gradient in the descending aorta when compared to the undissected model, particularly in the region proximal to the coeliac trunk.

This larger pressure gradient is associated with higher peak velocities and larger **WSS**. The section distal to the coeliac trunk region shows a drop in both the **TL** pressure gradient, **MP**, and reduced peak velocity and **WSS**. Local regions of high velocities and **WSS** are observed where flow through connecting tears impinge on the **TL** wall. Flow through the main entry tear creates a jet that impinges on the **FL** wall, creating a region of highly complex flow, increased pressure and **WSS**. As Tolenaar et al. [138] hypothesised, this region of high pressure in the **FL** is likely to be associated with aortic growth. The **FL** carries a greater proportion of descending aortic flow and is significantly larger than the **TL**. The **FL** exhibits a more homogeneous pressure gradient along its length, with lower velocities and lower **WSS** than the **TL**. High values of **WSS** have long been associated with remodelling due to activation of **MMP** and growth factors due to release of nitric oxide from endothelial cells [96, 28, 84]. While the case presented here is an that of an acute **AD** and as such will exhibit no endothelial cells on the wall of the **FL**, it is known that the **FL** can endothelialise over time [85, 156]. Therefore high values of **WSS** may indicate regions of concern which may be susceptible to remodelling in chronic **AD** patients.

In a second investigation, we examined the changes in left ventricular workload in **AD**. This was done via a 0D lumped-parameter heart model coupled to the image-based aortic model. Using this approach, left ventricular function can be obtained from the interactions between the heart model and the afterload provided by the aorta and the 0D models of the distal circulation. Left ventricular volume and pressure can be recorded, and a **PV** loop obtained. The intimal flap and more complex flow patterns in the aorta

result in higher energy losses and an effective increase in the hydraulic resistance felt by the heart. The heart model was tuned using values derived from Lau and Figueroa [82] to match the acquired 2D PC-MRI flow data and then adjusted to produce the same cardiac output as in the undissected case. Our results showed that there is an increase in left ventricular stroke work of 13.7 % in the dissected case compared to the undissected case for the same cardiac output. This is therefore an important consideration to observe in the management of chronic dissection patients, where conservative medical management is often adopted as a long-term strategy.

Previous aortic dissection CFD studies have typically used models consisting of a single entry and/or exit tear [71, 120, 68, 70, 59]. The effect of varying size and location of entry and exit tears in AD has been studied [142, 70, 117], and observational studies have examined the correlation of the number of communication tears and rate of growth of dissection [139]. Generally, the relatively small secondary tears have not been included in CFD studies of dissection. For the third study, we have tried, for the first time, to quantify the effect of secondary tears and found that these play a significant role in dissection haemodynamics. In our study, while the size of the individual tears was not altered, the number of connecting tears in both the proximal and distal parts of the dissection was. In other words, the total cross-sectional area available for communication between lumina changes as a result of the increase in the number of communicating tears. Our results showed that multiple tears along the length of the AD result in an equalisation of pressure between the lumina. An increase in FL flow was observed when more communicating tears are present. This would seem to be consistent with other clinical and experimental studies which have suggested that these secondary tears have a significant impact on the haemodynamics. Tolenaar et al. [139] showed that patients with a single entry tear had significantly poorer outcomes than those with multiple tears while Rudenick et al. [117] showed that small connecting tears resulted in a larger pressure difference between

the lumina with higher pressures observed in the TL, while larger tears resulted in an equalisation of pressure between the lumina. Rudenick's study also showed that the TL receives a larger proportion of flow in the case of smaller tears. Berguer et al. [7] showed that the pressure differential between the TL and FL is inversely proportional to the cross-sectional area of the exit tear. From the maximal tears results, it would also appear the inclusion of the two tears in the thoracic aorta had little effect on the pressures or flows in the lumina relative to the baseline case, and it may therefore not be necessary to include all connecting tears to ensure relatively accurate modelling of the AD haemodynamics.

We have also shown that the number of connecting tears can result in significant changes in both pressure and flow particularly in the TL when all secondary tears are occluded. This may be due to the high flow demand of the branching vessels around the coeliac trunk: secondary tears may facilitate the required flow to satisfy this demand. In the absence of secondary tears, this demand must be satisfied by the TL entirely. It is however clear that these tears are small in size and therefore difficult to identify with current imaging technology.

5.2 Computational Study of Anatomical Risk Factors in Idealised Models of TBAD

TBAD presents with large anatomical variability: lengths, TL and FL area ratios, number of tears, etc. AD haemodynamics are the result of the complex interplay between these anatomical features. Computational modelling is a powerful technique that can help elucidate the role of each factor. We used CFD tools to investigate haemodynamics in 15 idealised AD models with different curvatures, tear size, number of tears and tear patency.

In all cases, we applied identical boundary conditions, with a flow waveform explicitly applied at the inlet, and an implicitly derived pressure via a 0D Windkessel model at the outlet for which the parameters remained consistent for all simulations. This approach enabled a systematic comparison of the influence of geometry on haemodynamics between models.

Our findings revealed that curvature and tear shape had little impact on the haemodynamics. Hence, we performed most of our analyses in straight models with circular tears.

FL growth and aortic rupture is one of the major complications of TBAD. Pressure has been hypothesised to be a determinant of FL growth. It is likely that both changes in glsMP and PP play a significant role in this process [142]. From Laplaces law (wall stress (σ) = Pressure (P) x Radius (R) / wall thickness (h)), an increase in FL MP and the reduction in FL wall thickness, along with a FL radius potentially larger than the undissected radius, following AD increases wall stress relative to its pre-dissection value (Figure 5.3). As wall stress increases, FL diameter and risk of rupture also increase. Therefore, gains in FL MP directly impact FL wall stress, diameter enlargement and risk of rupture.

Recent animal studies have identified the strong role of PP in aortic remodeling [32, 33], specifically wall thickening, stiffening and loss of axial tension. It is in light of these recent findings that we systematically reported PP in our results. In general, we have seen that PP is more greatly affected by dissection than MP (Figure 4.10). Increases in MP and PP are directly attributable to the septum flap, which increases the resistance to flow substantially particularly in peak systole.

TL and FL flow splits and tear velocity are greatly affected by tear size. Small tears decreased FL flow and velocity. The opposite trend was found for large tears. These

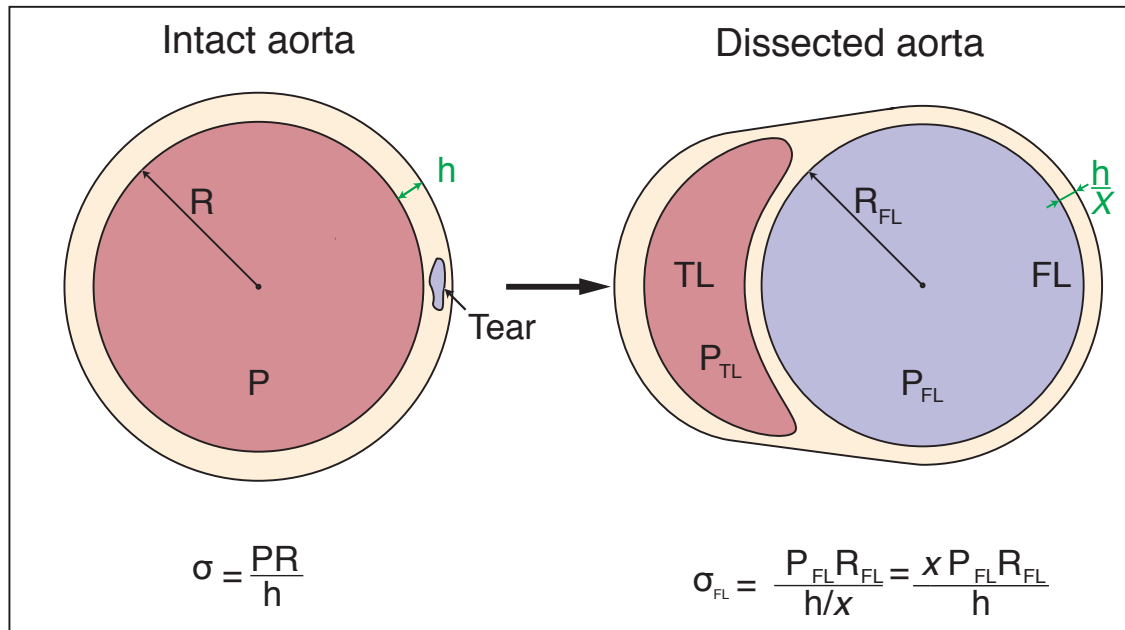


Figure 5.3: Anatomical risk factors in idealised models study: Laplace's law describing wall stress (σ) as a function of MP, radius (R) and vessel wall thickness (h) in an intact aorta (*left*) and a dissected aorta (*right*). Following dissection, pressure in the FL (purple region) may be significantly larger, FL wall thickness will be some ratio (x) of the undisturbed vessel wall, and the FL radius (R_{FL}) may be larger than that of the intact aorta, potentially causing σ to increase several fold.

findings are consistent with those reported by Rudenick et al. [118].

The location of the primary entry tear at the inner curvature has been previously identified as a predictor of complicated acute TBAD in Weiss et al. [153] and Loewe et al. [87]. Tolenaar et al. [138] showed that FL location at the outer curvature is associated with decreased aortic growth. Therefore, it appears that location of the FL in the inner arch of the aorta is associated with more adverse haemodynamics. Our results corroborated these findings (Figure 4.12). Larger MP, PP and lower velocities were found in the FL when this was located at the inner curvature. This pattern can be explained by Bernoulli's law:

$$\frac{v^2}{2} + gz + \frac{p}{\rho} = \text{constant} \quad (5.1)$$

where v is the fluid flow at a point on a streamline, g is gravitational acceleration, z is

the elevation above a reference plane (in our simulations, $g = 0$), p is pressure and ρ is density. This implies regions of higher velocity as what the FL experiences when located in the outer curvature, have lower MP for a given degree of total energy.

This study has shown that it is the combination of both entry and exit tear size that determines FL haemodynamics. For a given exit tear size, larger entry tears increased FL pressure. This is in agreement with the studies of Evangelista et al. [39, 38], which showed that entry tear size greater or equal to 1 cm diameter was a predictor of aortic growth. Conversely, for a given entry tear size, larger exit tears decreased FL pressure whereas smaller or occluded exit tears resulted in FL pressure increase. These results are consistent with clinical studies that identified FL partial thrombosis as a predictor of aortic growth [141, 132, 137] and mortality [142]. Our results were also in agreement with experimental studies [7, 117] that showed equilibration of TL and FL pressures as the tears size increases. Contrary to Tsai et al.[143] and Rudenick et al. [117], we did not find an increase in FL diastolic pressure when the exit tear was occluded, but a 16 % drop. This discrepancy might be explained by the lack of compliance in the 3D part of the models.

Thoracic Endovascular Aortic Repair (TEVAR) is one of the treatments for TBAD. Covering the entry tear with a stent graft aims to restore TL size and induce FL thrombosis by reducing FL velocities [104]. We investigated two models with proximal tear occlusion (*S0-10*, *St-0-10*), which revealed large decreases in FL pressure, velocity and flow. These haemodynamics are consistent with thrombus formation (due to slower blood velocity) and positive aortic remodeling (due to smaller FL pressure).

5.3 Strain quantification via dual phase black blood MRI in healthy and aortic dissection subjects

The results, using black blood MRI, produced similar deformation trends to those reported in other studies on healthy subjects [98, 97, 47].

E_{Long} and E_{Cir} both contribute to E_{Vol} which was found to be less in the **AAo** than in the **AA**. This may be due to added rigidity originating from the ligamentum arteriosum attaching the **AA** to the left pulmonary artery, the branching vessels, particularly the supra-aortic vessels and the attachment of the **DA** to the rigid spine. These all contribute to mitigate the longitudinal motion in the **AA** and **DA**. Figure 5.4 demonstrates how strain is affected. The image shows an overlay of the systolic (red) and diastolic (blue) segmentations for the healthy subject discussed previously in Figure 4.18.

Section A details the **AA** and the furcation of the supra-aortic vessels, the displacement of **InoA** is larger than that of the **LSCA** and is of a similar magnitude to the **LCoA** (Section B & C). Each ascending vessel is contributing to dampen the longitudinal motion, resulting in a relatively large value of E_{Long} in the **AA** (20.5 %). Further, the force generated in the inferior direction due to the contraction of the heart tends to pull the **AA** downwards and results in a compressive force and a negative value of E_{Long} in the **DA** (-1.9 %). As there are no branching vessels between the **LCoA** and **InoA**, deformation of the **AAo** more akin to a rigid body deformation, leading to lower E_{Long} with the primary contribution to E_{Vol} attributed to E_{Cir} . The **AA** demonstrates a larger E_{Vol} as both E_{Long} and E_{Cir} are relatively large. At the **LCoA**, mean displacement for the healthy cohort was found to be 10mm.

Both patients had a repaired **TAAD** with Dacron interposition grafts made of synthetic material significantly stiffer (up to 18 times) than normal aortic tissue [148]. It might be

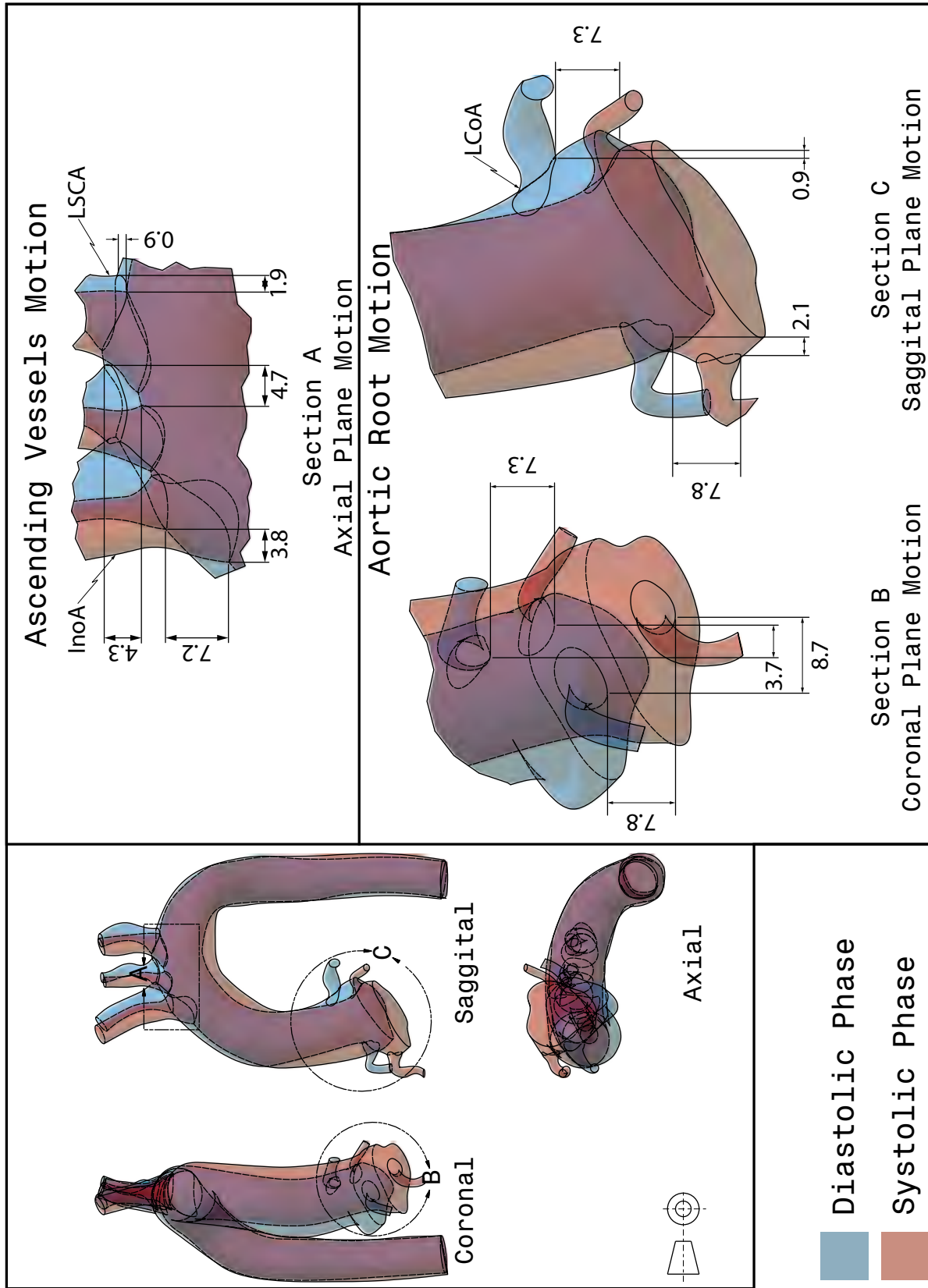


Figure 5.4: Strain quantification Study: Aortic root motion. Shown is an overlay of the diastolic (blue) and systolic (red) segmentations for the subject shown in Figure 4.19. Section A highlights the deformation at the ascending vessels. As can be seen the PInoA experiences a larger displacement than the more distal LSCA. This is likely due to the ascending vessels which act to tether the aorta and retard the tensile force imposed on the aorta due to contraction of the heart, and the rigid attachment of the DA to the spine. As the distal end of the AAo experiences less displacement than the proximal end this results in a greater E_{Long} in this region.

expected therefore, that the **AAo** would have a lower E_{Vol} , however patients A and B demonstrated greater E_{Vol} in the **AAo** than in the **AA**. There are many potential reasons for this trend.

Patient A has an apparent luminal stenosis of the aorta approximately halfway between **LCoA** and **DInoA**. This is possibly an irregularity as a result of the the configuration of the graft. The stenosis may result in a large pressure differential, subjecting the region proximal to the stenosis to relatively high pressures, and the vasculature distal to a significantly lower pressure at peek systole. Further, normal cardiac contraction may be causing the irregularity to widen across its cross-section in systole, resulting in a large increase in the **AAo** cross-sectional area and therefore an increasing the systolic volume. While less pronounced, patient B also exhibited the same trend and had an apparent stenosis proximal to **PInoA** which may have affected the pressure and strain distribution in a similar manner to patient A.

Both patients were older than the healthy cohorts (patient A: 46, patient B: 53 at time of scan). As the body ages, the aorta tends to lengthen by 3 % in the **AAo**, 7 % in the **AA** and 5 % in the **DA** [23, 22]. Patient B also had suspected Marfan syndrome could lead to even greater aortic lengthening [58]. The hearts of both patients were rotated towards the axial plane relative to the younger healthy cohorts, perhaps due to such lengthening. Contraction in this plane may be responsible for a compressive force and negative centreline strains as seen in the **AA** of both patients. Marfan syndrome is also known to affect vessel elasticity which may have further affected the strain distribution.

In regions affected by an **AD**, there is a complex interplay between the **TL** and **FL** which are separated a thin, highly distensible septum. This interaction is visible on the image reslices at a number of locations and may be due to a pressure differential between the two lumina. This differential may be due to the location and size of the entry and exit

tears. Dillon-Murphy et al. [27] demonstrated the number and location of connecting tears can have a significant impact on the the pressure field in the TL and FL, and Ben Ahmed et al. [6] demonstrated that the size and location of tears, particularly the relative size of entry and exit tears, can have a dramatic effect on FL pressure. Rudenick [118] showed similar results in their *in-vitro* study. It is know that the structural properties of both lumina can alter over time following dissection [110]. Differing vessel wall structural properties of the TL and FL may result in the stiffness of either lumina to be significantly larger than the other at any single material plane, which may result in differing observed strains in either lumina when exposed to the same pressure.

In the DA both patients A and B demonstrated compressive or negligible E_{Long} in the TL and a larger positive strain in the FL. This may be due to the geometry of the dissection. Curved vessels, such as the AA, undergoing radial strain only will then to experience larger E_{Long} in the tissue at the outer curvature than at the inner curvature (see Figure 5.5). As the FL is on the outer curvature in these two patients this may explain the results in the DA. This suggests if the FL is on the inner curvature it may experience a compressive E_{Long} in the DA.

As E_{Vol} is a product of E_{Long} and E_{Cir} , if the FL is on the inner curvature it may experience greater E_{Cir} and reduced E_{Long} for the same E_{Vol} relative to a FL on the outer curvature. This larger E_{Cir} could in turn could lead to an increased radial stress acting in the plane normal to the propagating crack edge between the intima and media and may drive peeling or mode I type crack propagation (see Figure 5.6). This has been suggested previously to be the primary mode of dissection growth [49, 127]. Clinical observations support this hypothesis and note that dissections which are orientated on the outer curvature have typically been associated with reduced risk of growth [138, 146].

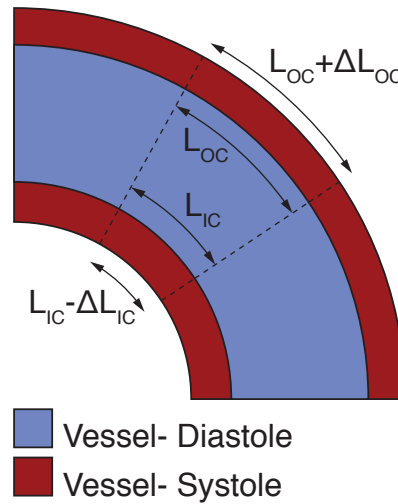


Figure 5.5: Strain quantification Study: Strain distribution in vessels with curvature. The figure shows an overlay of idealised vessel in systole (red) and diastole (blue). In the case of pure radial strain the arc length at the outer curvature L_{OC} will increase by ΔL_{OC} , and conversely at the inner curvature L_{IS} will decrease by ΔL_{IC} .

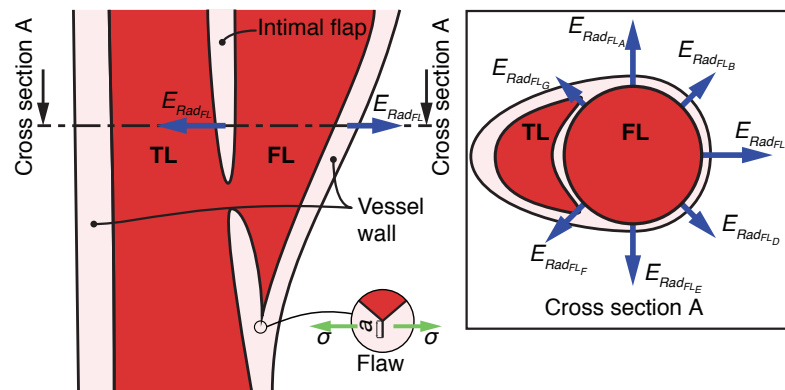


Figure 5.6: Strain quantification Study: Mode I crack propagation. As the FL deforms, it will be subjected to a number of different strains including radial strain ($E_{Rad_{FL}}$) shown here with the blue arrows. Radial strain will be experienced along the length of the FL and is due to wall stresses in the FL. At the crack tip, $E_{Rad_{FL}}$ will lead to tensile wall stresses acting in opposition across a crack flaw, represented by the green arrows (σ). Fracture theory states that energy that must be supplied to a crack tip for it to grow, the strain energy release rate $G_c = (\pi\sigma_f a)/E$, where σ_f is the stress at fracture, a is the length of the crack flaw, and E is the Young's modulus of the material. In mode I fracture if $\sigma > \sigma_f$ the crack will tend to propagate.

5.4 Impact of septum distensibility on simulated haemodynamics using a LPN

The results of the 3D patient-specific study (Section 4.1) showed that while it was possible to achieve mean flows that closely matched the observed data, we were not able to match the systolic and diastolic ranges of flows despite extensive iterations with outflow boundary condition parameters. Our CFD simulations showed a significantly higher flow in systole and reduced flow in diastole than seen with the 2D PC-MRI.

We have assumed that this was due to the lack of compliance in our 3D simulation. To test this hypothesis, a 0D analogue of the 3D simulation was constructed. While it cannot accurately model the complex haemodynamics at a small scale, this analogue makes it possible to introduce capacitors to simulate compliance in each lumina with a relatively low computational cost. The model was based on dimensions taken from the 3D geometry. All ascending vessels were combined into a single RCR and all branching and descending vessels into a second RCR. The values for these were calculated via Kirchoff's laws using the RCR parameters defined in the 3D simulation (see Table 4.1).

The simulations were run with two different stiffnesses. The first was relatively high ($E = 400 \times 10^{11}$ Pa) representing the rigid condition (for comparison the stiffness of diamond is approximately $E = 10.5 - 12.1 \times 10^{11}$ Pa). For the second simulation the stiffness was set to be more akin to that of aortic tissue ($E = 400 \times 10^3$ Pa). The results were consistent with Rudenick's original study [119]. Increased stiffness led to an increase in the systolic flows and decrease in diastolic flows. The results were also compared to the primary patient specific simulation corresponding to the minimal tears study. The mean and peak to peak values of both flow and pressure in each of the lumina for the rigid 3D simulation were found to be more comparable to the stiffer 0D model while the

2D PC-MRI flow data acquired in the patient's descending aorta was more comparable to the more compliant model. These results would seem to support our hypothesis that the mismatch between the flow waveforms observed via 2D PC-MRI and those simulated via CFD in the primary patient specific study (Section 4.1) is likely the result of one of the main limitations of the study, which is the lack of compliance in the model. Custom FSI techniques must be developed for this purpose.

5.5 Potential of AD modelling

AD represents a disease where the specific geometry leads to a unique and complex combination of haemodynamics and elastodynamics for each patient. Presently, clinicians have been limited to using markers and clinical indicators defined on image data to determine the best course of action for AD patients, however, as has been shown in this thesis, even small features and minor variations of geometries can have a significant impact on AD haemodynamics. While the 3D CFD simulations presented here have been rigid, we have also shown how variable the septum movement can be along the length of the AD, being likely an effect of the thickness and structural properties of the flap, the location of calcifications and thrombus formation, and the pressure differential between the TL and FL.

Currently pharmacologically treated AD patients routinely undergo regular follow up MRI and/or ionising CT scans to monitor the progression of the disease and determine treatment strategies which tend to be reactive to changes in the AD morphology rather than proactive. The work presented in this thesis involved the development of a workflow to generate patient specific 3D CFD simulations which could be applied to other AD patients. It is not inconceivable that with the falling cost of computing power and improvements in imaging, segmentation and simulation technology, such a workflow could

be developed to allow CFD analysis to be routine for AD patients and lead to treatments tailored to individual patients needs. Such simulation data might also be used to identify key areas of concern such as localised regions of undesirable haemodynamics or regions where the wall is under increased risk of failure due to high values of stress in the wall. Further, better knowledge and confidence of how stable the AD is may allow for fewer scans for patients and should assist clinicians in determining when surgical intervention is necessary and to pre-empt sudden events such as FL growth or rupture. Such tools may even allow the possibly to plan different surgical interventions, trial the performance of multiple types of stent graft in a variety of configurations and assess the ultimate outcome of each.

6

CONCLUSIONS

This chapter will briefly summarise this thesis's findings and will discuss the limitations of each of the four studies. This will in turn motivate the suggested future work described in Chapter 7.

Contents

6.1	Primary patient specific study	126
6.1.1	Limitations	126
6.2	Computational Study of Anatomical Risk Factors	129
6.2.1	Limitations	130
6.3	Strain quantification via dual phase black blood MRI	130
6.3.1	Limitations	131
6.4	Impact of septum distensibility on simulated haemodynamics	132
6.4.1	Limitations	133

6.1 Primary patient specific study: Multi-modality image-based computational analysis of haemodynamics in aortic dissection

In this primary patient specific study, multi-modality medical image data were used to create and validate a detailed computational model of haemodynamics in the human dissected aorta. This is the first study in which numerical predictions are quantitatively compared against [PC-MRI](#) data in the descending aorta. Our results show that secondary communicating tears, particularly larger tears, have a significant impact on haemodynamics in the descending and thoracic aorta.

There is a clear need for better imaging and computational methods to produce more accurate anatomical and physiological models of aortic dissection. Enhanced image-based simulation methods hold the key to improving our current understanding of the biomechanics of this complex disease. This better understanding will make it possible to devise better strategies for the long-term management of patients with chronic dissection, allowing for the identification of potential areas of aortic growth, ensuring visceral organs are adequately perfused and potentially aiding in surgical planning.

6.1.1 Limitations

Pressure data

In the study we did not have subject specific pressure data. Therefore, our pressure results are not validated per se, and are simply representative of a physiologically realistic range. This is an important limitation as the pressure in [TL](#) and [FL](#) may differ significantly depending of the size and number of connecting tears [\[117\]](#). In this work, the large size

of the connecting tears (13 mm proximally and 9.3 mm distally) makes the differences between TL and FL pressure modest, and therefore, the lack of pressure data may be less critical.

Image data

As the CAD segmentation is based on the image data, its accuracy is limited by the quality of image data. In this study, the available CT data had a voxel sizes of $0.73 \times 0.73 \times 2 \text{ mm}^3$ and $0.55 \times 0.55 \times 0.9 \text{ mm}^3$. While highly resolved, even better image data should yield better identification of small features such as tears, a more accurate model and therefore lead to more faithful simulations.

Further, CT data was acquired in two separate scans. A model was created using each image data set and bony landmarks were used to merge both parts of the model together. While multiple checks were made to ensure alignment was correct, small errors may have resulted in a misalignment of the data. Image data acquired in a single scan would avoid such errors.

In this study, the CT data acquired was not gated. As has been shown in this thesis, the septum can deform significantly during the normal cardiac cycle and it has been clinically observed that lumina can experience complete collapse [115]. Gated CT should allow the acquisition of the AD at the same point during the cardiac cycle and ensure better alignment of structures in the image data. The main limiting factor against using gated CT is acquisition time.

The boundary conditions were based on single VENC 2D PC-MRI data acquired in the ascending aorta and at three locations in the descending aorta. In order to be accurate, PC-MRI data must be perpendicular to the direction of flow [167]. While effort was made to ensure the 2D PC-MRI planes were orthogonal to the vessel centreline, flow not

perpendicular to the imaging plane may have introduced error. Further, multiple **VENC** should allow for the better acquisition of low velocities and result in more accurate values of flow.

Modelling Limitations

In the study, when comparing haemodynamics in the dissected and undissected models, two main assumptions were made. Firstly, given the acute nature of the dissection, we assumed that no **FL** remodelling had taken place, and therefore, we simply removed the intimal flap in the **AD** model to create a model of the undissected geometry. This was justified by the acute nature of the aortic dissection. In acute **AD**, there is minimal remodelling of the lumina and septum. Although the **FL** can potentially enlarge acutely due to its smaller thickness [91, 43, 36, 77], this expansion was not observed in this study. Secondly, we neglected the potential responses of both the baroreflex and the cerebral auto-regulation [82], which are likely to react to changes in aortic pressure and upper branch flow following aortic dissection. Ignoring the baroreflex and local auto-regulations resulted in assuming identical inflow and outflow boundary conditions for both the dissected and undissected cases.

Since no flow data were available prior to the onset of the **AD**, it was assumed that the cardiac output remained unchanged pre- and post-dissection. This assumption implies that the heart adapted to changes in afterload with the overall objective to maintain the cardiac output constant.

The heart model allows the estimation of stroke work, but as there were no image data available on ventricular volumes, a number of assumptions were made for the heart lumped parameter model such as end diastolic volume and preload. Our heart parameter models were taken from a previously published study [82]. As such, the stroke work shown

is an estimation of the cardiac workload. Future studies may benefit from the acquisition of cine image data of the heart.

The main limitation in the modelling approach for this study was the rigid wall assumption. As shown in Section 4.3 the septum flap can undergo significant strains in the normal cardiac cycle. By not simulating these displacements, it is not possible for the 3D CFD simulation to replicate the peak-to-peak range of flow observed in the 2D PC-MRI data. The introduction of greater compliance to the lumina leads to a better match between the observed and simulated data as demonstrated by the 0D simulation (Section 4.4). In order to accurately simulate the motion of the septum immersed in the blood flow, there are a variety of FSI methods which have potential for future work, some of which are summarised in Section 7.3.

6.2 Computational Study of Anatomical Risk Factors in Idealised Models of TBAD

Computational modelling enables systematic investigation of anatomical determinants of AD haemodynamics. Unlike clinical studies in which a single factor is investigated, computational analysis enables controlled parametric approaches such as those presented here.

In general, AD revealed increases in pulse and mean pressure relative to normal aortas. It is the combination of the proximal and distal tear size that determines AD haemodynamics. Smaller exit or larger entry tears increased FL pressures whereas larger exit or smaller entry tears decreased FL pressures. Other anatomical predictors such as distal tear occlusion and location of FL at the inner curvature also resulted in FL pressure increases.

6.2.1 Limitations

This study has several limitations. As with the primary patient specific study, the vessel walls were assumed to be rigid. A compliant 3D domain is likely to yield more realistic results.

The idealised models had a maximum of two tears, while AD patients have usually more than two [115, 78, 157]. The size and number of connecting tears will affect the transfer of flow between lumina, and therefore the pressure field. Each presentation of AD is likely to have its own unique haemodynamics.

The models did not include side branches, while in most cases several vessels branch off both TL and FL. Flow to side branches makes the velocity in AD more complex [124]. This may result in areas of slow flow (and therefore more likely to thrombose), alterations in mean pressure and pulse pressure, etc. The flap was not helical as is usually the case in AD. A more complex configuration of the flap will affect velocity and potentially pressure in TL and FL as seen in Section 3.1. Lastly, our models had a constant ratio of TL to FL area (0.175), except in the stented model (1.485). Models with different area ratios are likely to show substantial differences in haemodynamics. Recently, Lavangia et al. [83] showed that aortic growth rate and need for intervention was significantly higher in patients with TL/FL volume ratio < 0.8 .

6.3 Strain quantification via dual phase black blood MRI in healthy and aortic dissection subjects

The primary aim of this study was the quantification of strain in the aorta *in vivo*. The aorta is a highly compliant vessel, particularly at the aortic root. In this work, we quantified the longitudinal, circumferential and, for the first time, the volumetric strain

the aorta experiences *in vivo* during a normal cardiac cycle using entirely non-invasive MRI sequences.

3D Dual Phase Black Blood MRI images were acquired for a number of healthy subjects and for two patients with a repaired TAAD and residual TBAD component. Circumferential displacements were measured using the image data at 7 branching locations. Longitudinal and volumetric displacements were calculated for the ascending aorta, aortic arch and descending aorta using a 3D CAD segmentation created from the image data. For the AD patients TL and FL strains were measured separately.

For the healthy subjects, mean circumferential strains were found to be between 10.4% at the aortic root and 6.3% at the 5th intercostal artery, which agrees with other studies [98, 97]. Longitudinal strains were found to be largest in the aortic arch (13.2% mean) and a compressive strain was observed in the descending aorta (-1.5%). The largest volumetric strain was in the aortic arch (29.0%) and lowest in the descending aorta (16.7%). These results aligned with those found in similar studies [97, 98]. Both dissected patients showed the larger volumetric and longitudinal strain in the ascending aorta than in the aortic arch or descending aorta. Circumferential strains were found to highly variable due to the interplay between the TL and FL and these strains may drive FL growth via peeling and mode I type fracture.

6.3.1 Limitations

In order to quantify the maximum strain in this study we attempted to acquire image data at the point when the left ventricle was at maximum contraction and the aortic root at its most inferior point (i.e., systole), and at the point where the left ventricle was at maximum relaxation and the aortic root at its most superior point (i.e., diastole). It may be, particularly in the case of AD, that the maximum strain might be experienced at

some other point in the cardiac cycle. Images acquired at more data points throughout the cardiac cycle could resolve this question, however, this would dramatically increase scan time.

Images were also only acquired in the thoracic aorta. While the same material points were used in systole and diastole to measure the various strains, it may be that in the abdominal region different trends in strains might be observed. This may be particularly true in AD cases, as each of the lumina will supply a different set of abdominal vessels with different flow requirements, and could have a significant impact on the haemodynamics as seen with the primary patient specific study.

6.4 Impact of septum distensibility on simulated haemodynamics

One observation of the 3D simulations was that adequate tuning of the distal Windkessel parameters allowed for accurate replication of the mean flows observed in the 2D PC-MRI data. However the computed peak-to-peak value of flow was far greater than that of the observed in the patient data. We hypothesised that the reason for this was the lack of compliance in the TL and FL.

To test the hypothesis, a 0D surrogate of the 3D model was created, where the 17 RCRs representing the distal vasculature of the 3D model were lumped into two, and the 3D domain itself was represented by inductors, resistors, and capacitors, the values for each calculated directly from the 3D geometry. The value for compliance in each of the lumina was also dependent on stiffness, and two 0D simulations were run: One with a high stiffness, and one with a low stiffness. While the 0D model is not capable of replicating the highly complex haemodynamics observed in the 3D simulation, it does allow for the

reasonable analysis of the impact of compliance on both the pressure and flow field in regions where the haemodynamics are not as complex.

The results seem to confirm the hypothesis. Large values of stiffness (low compliance) in the lumina led to larger peak-to-peak values of both flow and pressure. The stiffer simulation gave more comparable results to the rigid 3D simulation, where as the more compliant simulation resulted in values more aligned with the [2D PC-MRI](#) data.

6.4.1 Limitations

While there is a reasonable agreement between the 0D and 3D models, it should be noted that the 0D model is a gross simplification of the 3D simulation. Energy losses from the complex flows observed are not accounted for in the 0D analysis.

For simplicity, the model lumps a number of [RCRs](#) into two individual outlets and does not contain any abdominal branches. This was considered justified as results were compared only in the thoracic region of the [AD](#), proximal to the abdominal branches.

A further simplification was to remove all secondary tears from the model and consider only the primary entry and exit tears, basing the 0D model off the minimal tears model from the primary patient specific study. The primary study does show that the secondary tears can have a significant influence on haemodynamics, and their inclusion may be necessary to accurately replicate [2D PC-MRI](#) flow data. This may explain the mismatch between the mean flows observed in the 0D model and [2D PC-MRI](#) data.

7

FUTURE WORK

There are a number of methods which may allow for better data acquisition and simulation and could lead to more accurate results in future work. This chapter will suggest techniques of imaging, pressure acquisition and fluid structure interaction methods which might be of interest for future research.

Contents

7.1	Imaging	135
7.2	Pressure data	136
7.3	Lack of compliance in 3D domain	136
7.3.1	Immersed boundary method	139
7.3.2	Fictitious domain method & mortar element method	140
7.3.3	Immersed finite element	140
7.3.4	Immersed structural potential method	141
7.4	Potential for future studies	141

7.1 Imaging

The primary imaging modality used to create the aortic dissection computer model in the primary patient specific study was non-gated contrast-enhanced CT. It has been observed that non-gated CT may contain pulsation artefacts that can result in the generation of an artificial intimal flap [113, 44]. There are inherent disadvantages to gated CT such as higher radiation dose and longer scan time. However, gating does allow for the capture of the septum at the same phase in the cardiac cycle, thereby eliminating motion due to pulsation. Imaging the septum in such a way should eliminate the majority of motion artefacts and allow the reconstruction of a more accurate representation of the geometry.

It is generally desirable to have higher spatial resolution for both CT and MRI data when performing image segmentation as low spatial resolution limits the size of features that may be included in the computer model, and, in this instance, made identification of the relatively small secondary tears difficult. Twenty-five images were acquired for both 2D PC-MRI and 4D PC-MRI data sets resulting in a temporal resolution of 52 ms. When acquiring PC-MRI data, higher temporal resolution may enable better observation of the septum motion. Higher temporal and spatial resolution of 4D PC-MRI should allow for flow patterns through tears to be more readily observed.

The 2D PC-MRI data were acquired at three locations in close proximity in the thoracic region of the aorta. A greater number of 2D PC-MRI scans capturing flow in the coeliac and iliac regions may have enabled a better, more accurate tuning of the outflow Windkessel models. Furthermore, dual VENC in the descending aorta would have increased the fidelity of the reconstructed TL and FL flows since significantly different maximum velocities are found in the two lumina.

The results indicate that inclusion of the difficult to image connecting tears is necessary

for accurate modelling. Arterial spin labelling (ASL) is an MRI technique which allows the tracking of labelled blood over time [161]. This technique could be used in dissection patients to identify secondary connecting tears by detecting the transfer of labelled blood between the lumina.

Lastly, initial results using black-blood imaging techniques such as those used for the strain study have yielded excellent results in imaging the intimal flap accurately. This technique avoids the exposure to radiation of CT. However, scan time can be excessive, particularly when trying to acquire the full geometry of the AD.

7.2 Pressure data

One of the primary limitations of the 3D study was the lack of pressure data for the patient. Future studies may benefit from accurate measurements of patient pressure which should allow for more accurate simulations. Patient-specific pressure data may be acquired using an external pressure cuff, or using soft, pliable wires with a high-fidelity sensors which can be collected at multiple locations in the aorta from patients and may be performed during planned endovascular procedures. As the AD has a significant influence on the pressure field, invasive pressure measurements would be far more accurate than cuff measurements. These pressure data will provide a gold standard for the simulated CFD pressures.

7.3 Lack of compliance in 3D domain

One of the primary limitations with the simulations presented in this thesis is the lack of compliance in the 3D domain. As seen with the strain quantification study (Section 4.3) the septum flap can undergo significant deformations during systole. Other studies

have also shown that the TL experiences expansion and forward flow during systole, and an almost complete collapse during diastole due to pressure fluctuations. This may increase the risk of end-organ ischaemia. FL flow can be seen to be delayed, absent or even reversed, depending on the geometry configuration of the tear and the degree of communication between the TL and FL [36]. To properly account for these deformations, it is necessary to simulate the interaction between the solid and fluid.

Typically fluids are described by an Eulerian description (i.e. one in which the frame does not move and velocities and pressures are observed at fixed locations) while solids are treated with a Lagrangian description (i.e. one in which the frame is fixed relative to the solid, and deformations and stresses are measured at fixed points). As an analogy, if one considers a boat flowing down the a river, a Lagrangian description is similar to sitting in the boat and observing its motion, while a Eulerian description is similar to standing on the river bank and observing the boats motion. Deformations in solids are relatively small and particles in solids do not generally move out of position relative to each other when deformed, whereas the opposite is the case with fluids. For finite element analysis, meshes based on these two descriptions are used to model either solids or fluids. It should be noted however that both fluids and solids can be modelled by either description.

In cardiovascular flows, there exists a situation where there is a viscous, incompressible, pulsatile fluid; blood, is being transported within a deformable vessel; the walls of the vasculature [135]. The motion of the solid and the flow of the fluid highly influence each other. In order to model both fluid and solid 3D domains, strategies need to be used to couple the Eulerian and Lagrangian reference frames. This has become a major area of research in the field of cardiovascular mechanics.

For relatively small deformations, methods such as the coupled momentum method which models a linear stress strain relationship for the vessel wall and embed the elastodynamics

equations weakly as a boundary condition for the fluid problem [41] give a relatively accurate approximation of the interaction between fluid and solid in most cases. However, for cases where these deformations are larger, such as those seen in cases of dissection, these methods can be inadequate. The issue is further complicated by the fact arteries, like many biological tissues, are both anisotropic and have a non-linear stress strain relationship, therefore, more advanced methods must be sought.

Two different families of methods could be pursued: boundary fitted and non-boundary fitted. Boundary fitted methods maintain a sharp interface between the fluid and solid domains via mesh modification, potentially requiring remeshing, whereas non-boundary fitted methods do not have a sharp interface. Conservation is achieved by imposing the kinematic compatibility condition, which is due to the no-slip condition of viscous fluids at a solid boundary, and the dynamic compatibility condition, which stems from Newton's third law, i.e. imposing the continuity of forces between the solid and fluid domains.

Arbitrary Lagrangian-Eulerian (ALE) formulations are an example of a boundary fitted method. This is an adaptive re-meshing approach whereby mesh updating algorithms revise the Eulerian mesh so that node-on-node compatibility is maintained at the fluid structure interface at the boundary of the fluid and the solid as the Lagrangian mesh deforms. Therefore compatibility throughout the Eulerian mesh is maintained. There is an arbitrary grid velocity which is determined by the dynamic and kinematic compatibility conditions between the two continua [135, 106, 107].

Essentially, there are three tasks the solver must perform on each time step. Firstly, the Navier Stokes equations of motion for the fluid domain are solved representing the blood flow, secondly, the elastodynamics equations of motion are computed for the solid domain, and finally the fluid grid is updated to maintain compatibility between the two domains throughout the Eulerian mesh [129, 135]. This can be computationally expensive and

especially so when there is a large degree of oscillatory motion of the solid phase, leading to excessive distortion of the fluid mesh and the necessity for constant re-meshing [5, 169]. To overcome these issues numerous non-boundary fitted methods have been developed which do not require re-meshing or node on node compatibility, but rather impose the necessary dynamic and kinematic compatibility conditions between the fluid and solid phases by the introduction of a fictitious force field in the Navier Stokes equations.

7.3.1 Immersed boundary method

In recent years, non-boundary-fitted methods have been developed to represent the dynamics of thin structures embedded in a fluid. Peskin, in his 1972 seminal paper [111], coined the term *Immersed Boundary Method (IBM)*. Peskin had set out to establish a fast and efficient method to study the deformation of slender heart valves immersed in a dynamic fluid. Unlike *ALE*, this method does not have the requirement that a Eulerian mesh be updated as a Lagrangian mesh deforms. Rather, the formulation established a fluid domain represented by a regular 2D Cartesian grid, and the solid domain represented by a dynamic, 1D Lagrangian mesh. The solid motion is then imposed not by modifying the mesh, but rather by the imposition of a fictitious force value which serves to replace the solid. It is the spreading of forces from the solid mesh to the fluid that imposes the dynamic compatibility and similarly, spreading the velocities from the fluid to the solid, imposing the kinematic compatibility.

Between each nodal point of the fluid and solid mesh, the dynamic and kinematic compatibility conditions are maintained by use of the Dirac delta function. The method developed by Peskin was originally proposed for the finite differences method, and is severely restricted (e.g. limited to regular Cartesian grids and solids with the same density as the fluid etc.), but researchers have since overcome these drawbacks by modifying

Peskins original idea and its concepts have since been extended by other researchers to the [Finite Element Method \(FEM\)](#) [5, 169, 54, 61].

7.3.2 Fictitious domain method & mortar element method

The [Fictitious Domain Method \(FDM\)](#) developed by Glowinski et al. [54] was originally developed for the purpose of solving complex geometries on a regular grid in a highly efficient manner. Like with Peskins [IBM](#) approach, the actual domain of interest is embedded in a regular rectangular mesh. However, in place of the Dirac delta function, Lagrange multipliers are used in a fictitious domain to restrain the domain boundary. The key advantage to this method is that it allows the use of a fairly structured mesh on a simple auxiliary domain which contains the actual domain.

The [FDM](#) of Glowinski was extended to fluid structure interactions by Baaijens [5]. The fluid phase is again represented by Eulerian mesh while the solid by the incompatible Lagrangian mesh. The method uses Lagrange multipliers and considers the energies of both systems (solid, fluid and the interface).

7.3.3 Immersed finite element

The [Immersed Finite Element \(IFM\)](#) method was proposed by Zhang et al. [169]. This method developed the [IBM](#) extending it to Finite Elements and also allowing for the use of higher order kernel functions. One of the disadvantages of [IBM](#) is the necessity of regular uniform grids. Use of higher order kernels for the delta functions allows the domain to be non-uniform and therefore finer meshes in areas of interest can be specified, allowing for more computationally efficient implementation.

7.3.4 Immersed structural potential method

The **Immersed Structural Potential Method (ISPM)** was developed by Gil et al. [51, 162, 52]. This was developed as a modification to **IBM**. It uses the same method of representing the solid and it handles the **FSI** problem via the introduction of a fictitious force in a modified version of the standard Navier Stokes equations. A key improvement in this method is the ability to consider the density of the solid, and therefore the bodies mass can be considered and not the massless structures to which **IBM** is limited. The solid phase is represented with the Helmholtz free energy functional and the principle of virtual work can be applied to minimise the strain energy of the solid body. The force of the body can then be defined in terms of the first Piola-Kirchhoff stress tensor.

This method was originally formulated in a finite volumes context but has also been extended to finite elements by Hesch et al. [61].

7.4 Potential for future studies

In summary, there exist a wide variety of methods which may be used to simulate **FSI** in 3D domains. For the case of **AD**, where there may be large septum motions, the computational cost of constant re-meshing required for **ALE** may make it prohibitive. Non boundary fitted methods may be more efficient and less computationally expensive and particularly well suited to this task. Inclusion of wall motion may yield more accurate results, and potential additional insights into the wall dynamics involved in **AD** and the interplay between the **TL** and **FL**.

OTHER CONTRIBUTIONS

In the process of completing this thesis, there are a number of projects which are on-going, and significant contributions which do not fit under the paradigm of AD modelling. This chapter will discuss these briefly.

Contents

8.1	Introduction	143
8.2	Effects of Age-Associated Regional Changes	143
8.2.1	Overview	143
8.2.2	Contribution: CAD modelling	144
8.3	Haemodynamic and morphological changes over time	147
8.4	Patient specific segmentation for 3D printing	151
8.4.1	Experimental aortic coarctation simulation to assess the interaction of stents with haemodynamics and arterial wall	151
8.4.2	Haemodynamic and strain alterations arising from varying tear patency in cases of aortic dissection	154

8.1 Introduction

In the undertaking of this PhD, there are a number of other worthy contributions which do not fall under the paradigm of AD or are continuing currently still under investigation. This chapter gives a short summary of this work and the contribution made.

8.2 Effects of Age-Associated Regional Changes in Human Central Artery Mechanics on Systemic Haemodynamics Revealed by Computational Modelling

8.2.1 Overview

Stiffening is an inevitable by-product of ageing. It may be accelerated due to an acquired disease such as Marfan syndrome, Elhas Dhanos syndrome, hypertension, etc [47]. Increased arterial stiffness leads to increased [Pulse Wave Velocity \(PWV\)](#) which in turn causes larger wave reflections, augmenting pulse wave and giving rise to increased [Pulse Pressure \(PP\)](#), cardiac workload and decreased diastolic perfusion. It is thought that these conditions may lead to a vicious cycle, and contribute to additional damage to connective tissues, especially elastin, deterioration of [SMCs](#), propagation of [GAGs](#), and reduced [SMC](#) function, all of which contribute to increased stiffening [25, 47].

To many, the gold standard measure of arterial stiffness remains the [Carotid-to-Femoral PWV \(cf-PWV\)](#) [12] which considers a large portion of the arterial tree, averaging geometric and material properties. Age related changes tend not to be uniform along the length of the aorta and there remains the question of whether early changes in [cf-PWV](#) can indicate a future disease risk.

The main aim of this study is to examine the effects ageing has on haemodynamics,

specifically *cf-PWV*, over a 45 year period. This involved a multifaceted approach. Image flow and pressure data were acquired for a 30 year old male volunteer. Population averaged changes were then applied to this model in terms of material properties of the vessel wall (e.g. biaxial stiffness and thickness), haemodynamic boundary conditions and geometry. Four models for the subject were created, at 30 , 40, 60 and 75 years old. A simulation was then run for the 40, 60 and 75 year old geometries, the 30 year old was disregarded due to a lack of material properties data in the ascending aorta at this age. For each simulation, arterial wall stiffness was modified for each model based on data in the literature [116] and *FSI* was modelled using the coupled momentum method [41].

The results of the study compare well to clinical data from large populations and provide a high resolution description of the evolution of local and global age related metrics of arterial wall stiffening. This research is led by Federica Cuomo (Department of Biomedical Engineering, University of Michigan). A paper is currently under review.

8.2.2 Contribution: CAD modelling

An initial *CAD* model was created for the 30 year old volunteer using high resolution *MRI* image data. The model was created using the 2D segmentation approach described previously (see Section 3.3.4). An advantage of the 2D segmentation method and the parametric nature of the contours is they allow for relatively simply and yet highly controlled manipulation of the geometry. Three artificially aged models were created representing the subject at 40, 60 and 75 years old (Figure 8.1).

Modification of aorta centreline

The first task in creating the aged model was to alter the length of the aorta, reflecting the population-averaged changes in aortic length observed in the thoracic aorta associated

with normal ageing. Craiem et al. [22] has noted that this length increase is not uniform, and that per 10 years ageing, the ascending aorta (branching point of the LCoA to the InoA) exhibits a 3% increase in length, the arch (region between the InoA and LSCA branching points) a 7% increase in length, and the thoracic descending aorta (the region from the LSCA to the level of the Coronary Sinus (CS)) a 5% increase in length. Distal to this point no significant changes in length are observed.

The centroid position for each contour was calculated in the thoracic region (from LSCA to CS) and used to create a 3D cubic spline. This spline was then modified with the aim of reflecting the expected change in length and each contour was transformed and rotated to lie at the same relative position to the updated spline.

Tortuosity in abdominal aorta

An expected decrease in the subject's height due to ageing [128] was incorporated into the modified models. This involved using a process similar to that described for the modification of the thoracic aorta, reducing the distance between CS and iliac bifurcation, in this instance maintaining the arc length of the aorta. This resulted in a realistic increase in the tortuosity in the abdominal aorta.

Change in diameter

As well as changes in length of the aorta, there is also a quantifiable, non-linear change in diameter associated with ageing [116]. The equivalent diameter of each contour was adjusted based on its relative position along the aorta centreline (from LCoA to iliac bifurcation).

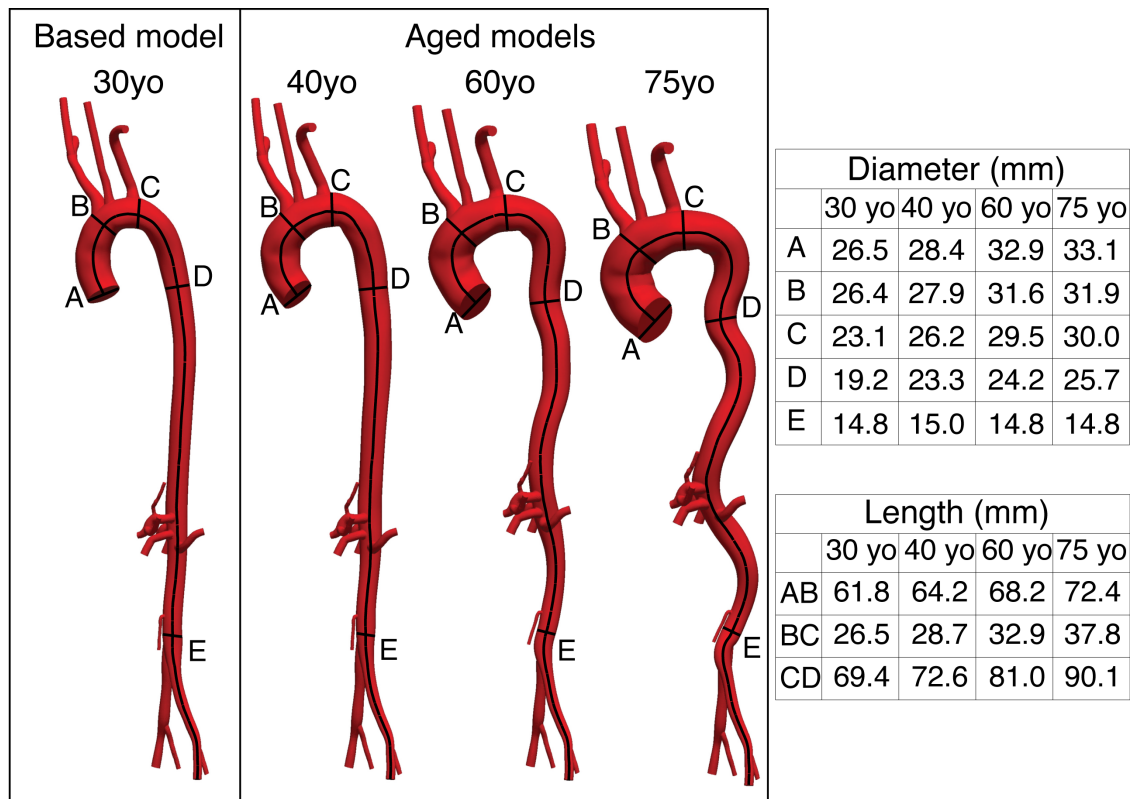


Figure 8.1: Other Contributions - Ageing study: Illustrative 3D geometrical models for (left) initial 30 year old (yo) model and (centre) three artificially aged models, namely, 40, 60, and 75 yo for the test subject. The prescribed values of local inner diameters and segmental centreline lengths (right). The transverse lines on the geometric models denote the key material points (i.e. A (*LCoA*), B (*InoA*), C (*LCCA*), D (*CS*), E (*iliac bifurcation*)). The cross-sectional areas of each contour defining the geometry were also modified using values interpolated based on the contours relative position along the vessel centreline [116]. All dimensions are given in mm.

Vessel branches

The position of branching vessels along the aorta was also modified to maintain the same branching location relative to the updated vessel centreline. Branching vessels diameters were also uniformly scaled based on their branching position along the arc length of the aorta.

8.3 Haemodynamic and morphological changes over time in cases of chronic AD

Patients with chronic AD can live for years managing the disease pharmacologically without the need for surgical intervention. For some, thrombus formation can completely occlude the FL, stabilising the FL and restoring full flow to the TL, while for others, aortic growth or added complications may occur leading to surgical intervention and an elevated risk of a morbid event.

For this reason, chronic AD patients undergo monitoring and have regular MRI, ultrasound or CT scans. MRI and ultrasound are recommended for monitoring as they do not have the issues of imparting ionising radiation as CT does, but do not have the same resolution as CT. Regardless of the technique used, clinicians attempt to use these image data to identify indicators of imminent problems warranting surgical intervention such as those discussed in Section 3.2.

Studying the progression of AD haemodynamics over time may yield a better understanding of the evolution of the disease. It may also be possible to identify if the AD is stable, or whether the FL is thrombosing.

The primary aim of this study will be to use patient specific blood flow modelling to try to assess haemodynamic and geometric changes in AD over time. The study will utilise the routinely acquired image data along with cuff pressure measurements and 2D PC-MRI flow data acquired at the time of CT scanning. A number of segmentations of the vasculature will then be created using the CT data and a similar work flow as the one formulated for the primary patient specific study (Section 3.1) will be utilised.

To date, a number of chronic AD patients have been recruited and data has been acquired over a 12 month period. Models have been built for a selection of the patients (Figure 8.2),

and initial simulations have been run on a number of meshes. While no final results have been completed, the initial results are promising. Figure 8.3 shows results corresponding to a single patient. The left panel of the figure shows the mean pressure in the domain over a single cycle, while the right shows the maximum velocities observed throughout the cycle. Each panel shows results at baseline (0 months) and at 12 months respectively. The boundary conditions for each simulation were tuned to match the mean flow (within $\pm 2.5\%$) and mean pressure (within $\pm 4\%$) for the patient at time of scan.

The geometric model seems to indicate the patient is performing well with pharmacological treatment. Thrombus has occluded a large portion of the FL in the thoracic region, leaving a small residual component distal to the LSCA at the arch, and is partially thrombosed in the abdominal aorta. The follow up scan indicates thrombus has continued to grow, and a large tear at the proximal end of the abdominal region of the FL has become partially occluded.

The changes in morphology have had an influence on the haemodynamics. The mean pressure gradient between TL and FL has increased from approximately 3.0 mmHg to 4.5 mmHg and mean pressure in the FL is significantly lower at 12 months than at baseline. The partially occluded tear has also caused a localised increase in the peak velocity but has resulted in lower peak velocities being observed distally in the FL. These conditions are often seen as more favourable to thrombus growth and stability of the FL. Again, it is important to note that boundary conditions for both baseline and 12 month simulations are applied to match patient specific pressure and flow data acquired at the same time as image data.

This work is being performed in collaboration with Dr Alia Noorani (Imaging and Biomedical Engineering, Kings College London) and Dr C. Alberto Figueroa (Conrad Jobst Vascular Research Lab, University of Michigan Health Systems).

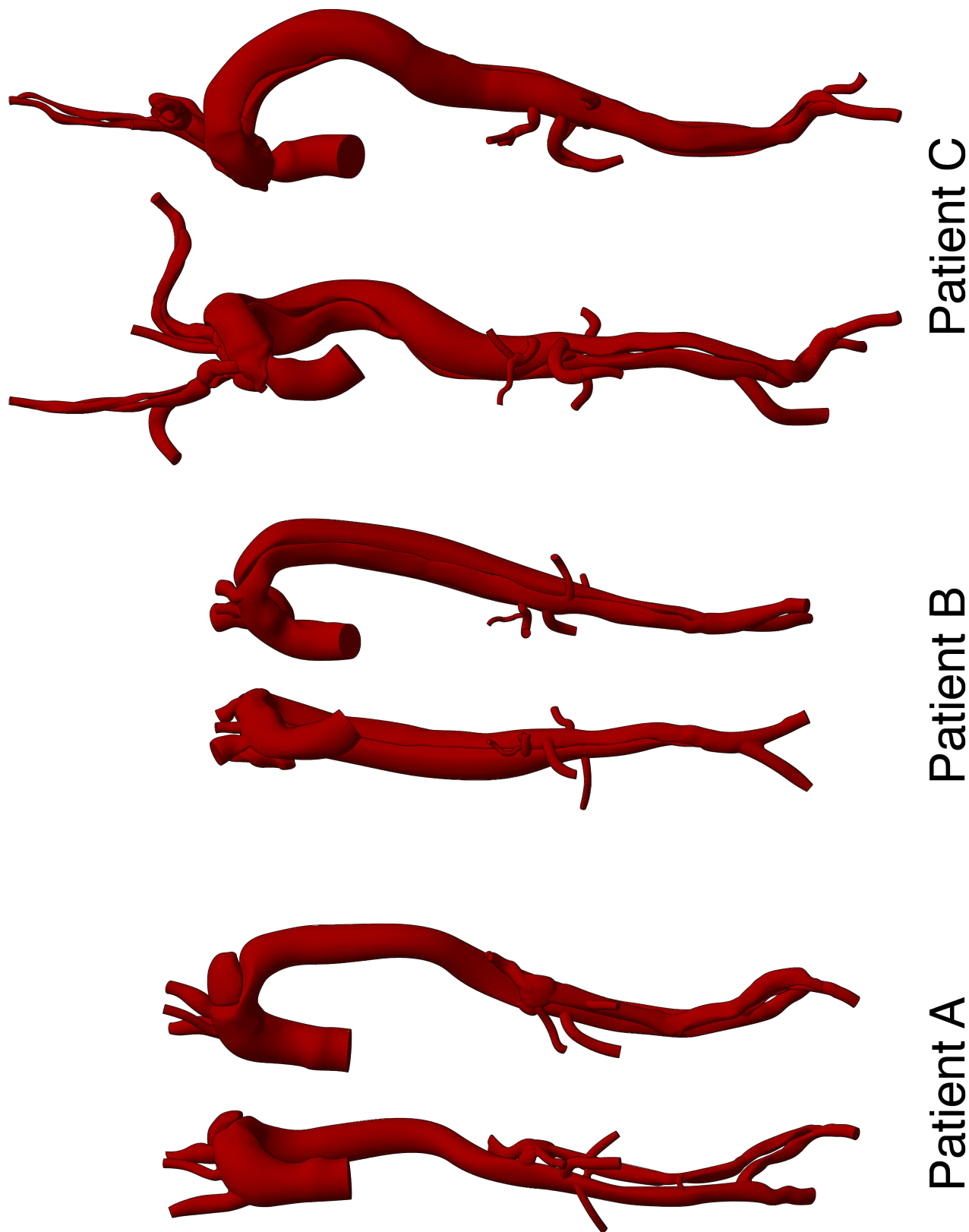


Figure 8.2: Other Contributions - Time related changes in AD: Example geometries. A sample of segmentations completed for the patients recruited in the study. All examples shown here are built from the initial CT scan. The patients show various degrees of thrombus growth in the FL and extent of the AD.

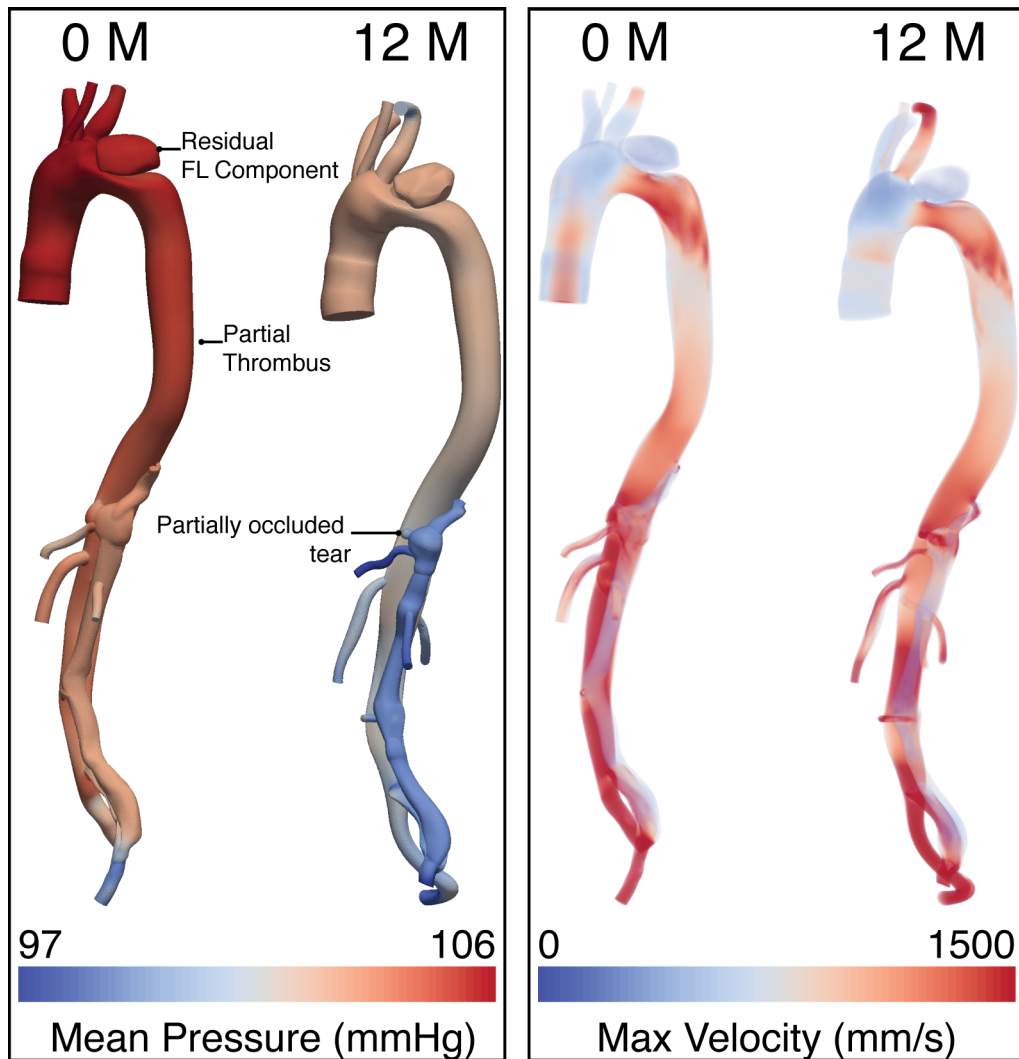


Figure 8.3: Other Contributions - Time related changes in AD: Initial results example. The image shows the results for the simulations run for a single AD patient spaced 12 months (M) apart. Each model is built from CT image data, 2D PC-MRI flow data is applied at the inlet and at each outlet RCRs are tuned to match flow data in the descending aorta and cuff pressure measurements acquired at the time of scanning. **Left** shows the mean pressure values averaged over a single cycle, and **Right** shows the values of peak velocity.

8.4 Patient specific segmentation for 3D printing

Recently, falling costs, wider availability and better materials technology have allowed 3D printing to become more widespread. 3D printing typically involves the generation of a surface mesh file, typically an [STereoLithography \(STL\)](#) file or similar. This is passed to a printer which performs a layering process, sequentially depositing and fusing thin layers of material to create a complex 3D shape. This work uses 3D printing and segmentation to create phantom models of diseased geometries. These models can be useful for a variety of purposes such as validation of [CFD](#) results, or real time analysis of the haemodynamic effects of surgical intervention or to test medical devices [9].

Two such projects have been undertaken with the intention of creating 1:1 scale silicone phantom replicas of different aortic segmentations. For this, the lost wax method is employed. 3D printed wax models of the vessels are created and then coated in a thin layer of silicone. Once dry, the wax is then heated to remove it from the cast.

8.4.1 Experimental aortic coarctation simulation to assess the interaction of stents with haemodynamics and arterial wall

The first of these was created from a segmentation of a 15 year old male with a severe congenital aortic coarctation located in the descending thoracic aorta exhibiting a 60% reduction in lumen diameter and a 24 mmHg systolic pressure gradient across the coarctation. As is typical for patients with such congenital coarctation, the flow demand of the abdominal organs leads to the remodelling of the internal thoracic arteries. As a result, these arteries abnormally enlarge to carry additional flow.

Figure 8.4 shows a volume rendered 3D [Steady-state free precession MRI \(3DSSFP\)](#) image data acquired for the patient with the segmentation *in situ*. The coarctation and

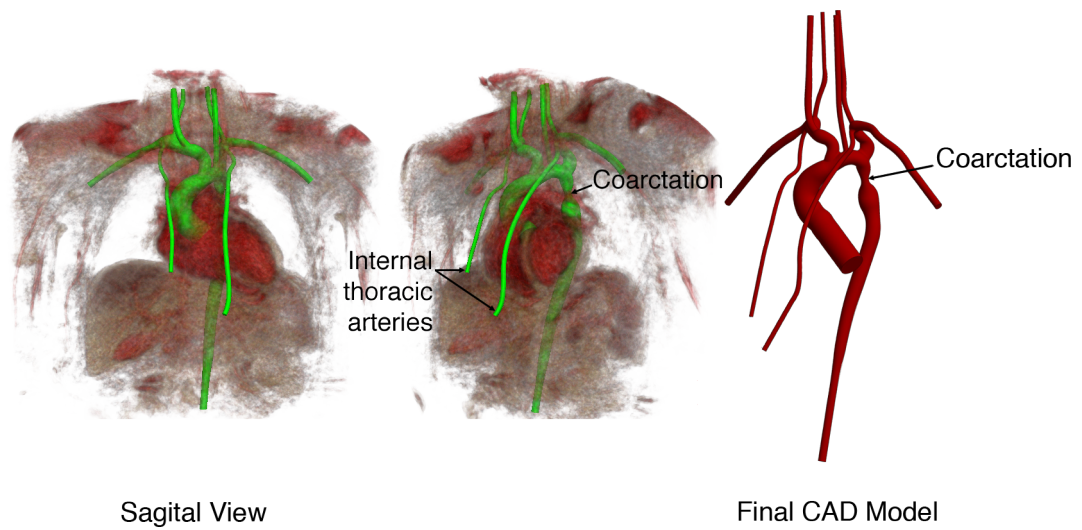


Figure 8.4: Other Contributions - Patient Specific segmentation for 3D printing: CAD models. The image shows a (**Left**) sagittal view and (**Centre**) 45° rotation about the vertical axis of a volume render of the anatomy with the 3D segmentation presented *in situ* (shown in *green*). **Right** the final CAD model used to create the printed wax mould. The model has been altered and each of the outlets extended significantly (50-100mm) to allow them to be attached to various fittings. The coarctation and enlarged internal thoracic arteries are highlighted.

enlarged internal thoracic arteries are highlighted. This model was then exported to a commercial CAD package [4] and minor modifications were performed to produce the final surface mesh. This model was then printed in wax and then cast in silicone using the method described previously, the resulting phantom shown in Figure 8.5.

The printed phantom was then mounted on a wet table and connected to a PC controlled ventricle. A modular haemodynamic simulation was performed and acquisitions of pressure, flow and linear strain were recorded at 1000Hz. A stent was then deployed and measurements were retaken. These measurements were compared to patient specific measures acquired in the Cathlab.

This work is being led by Dr Nicholas Gaddum (Imaging and Biomedical Engineering, Kings College London). The results are awaiting publication.

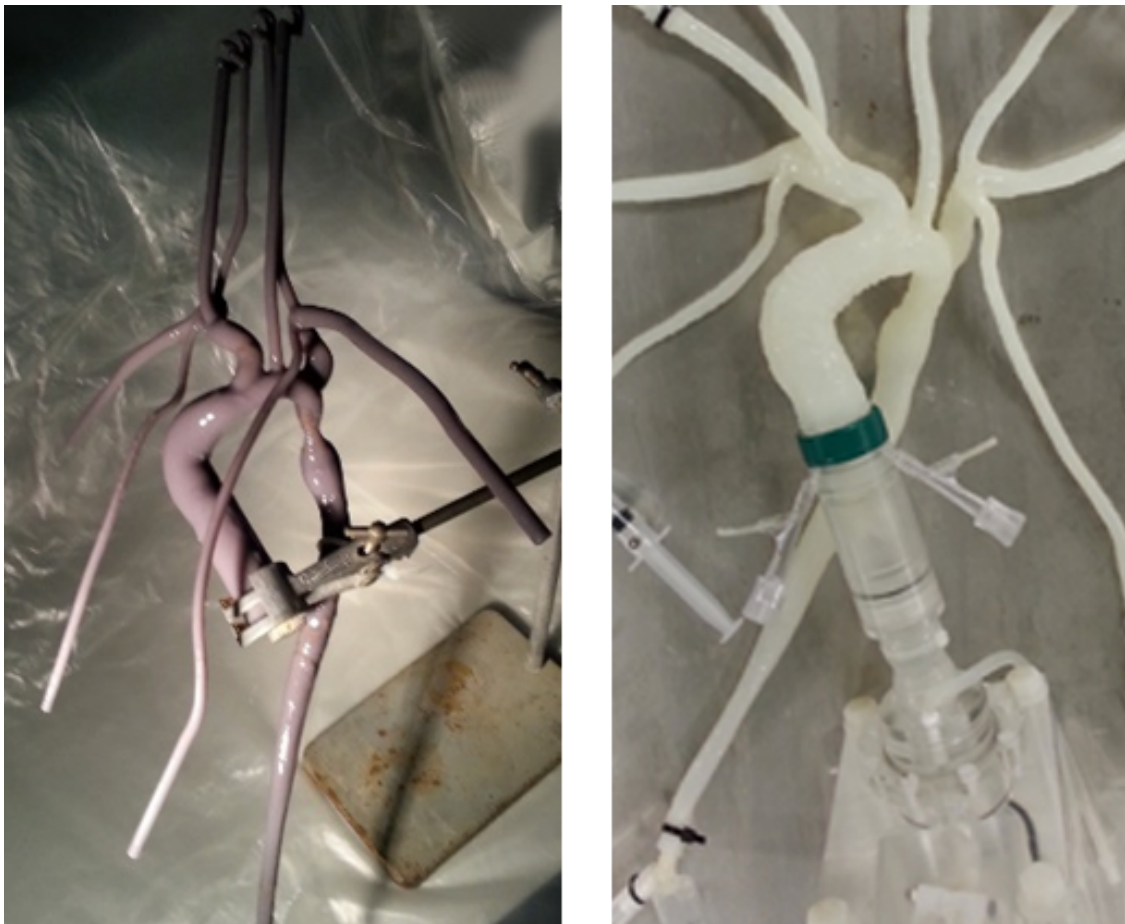


Figure 8.5: Other Contributions - Patient Specific segmentation for 3D printing: Patient A: Final phantom model. The figure shows the final 3D printed silicone model created via the lost wax method and 3D printed wax mould.

8.4.2 Haemodynamic and strain alterations arising from varying tear patency in cases of aortic dissection

The second segmentation to be considered is a model of a 31 year old, male chronic AD patient. The AD exhibited no thrombus formation and extended the entire length of the descending aorta. A number of minor modifications needed to be made to the model. The orientation of a number of the vessels was adjusted distal to their branching point so the model could lie flat without vessels impinging upon one another. Due to limitations on the structural integrity of silicone, the septum flap needed to be thickened in a number of locations to prevent the final model tearing. Only the primary entry and exit tear were included in the model and all secondary tears were ignored. The final surface mesh is shown in Figure 8.6.

At time of writing, the final silicone model is not yet complete, but it is intended that this model have a capability for adjustment of the inlet and exit tear, allowing for the controlled reduction in tear diameter. Coupled with pressure wire measurements it will be possible to observe in an *ex vivo* setting how tear patency affects pressure and flow in the FL. The model will also serve as a useful validation of any FSI methods used in future simulations which include septum flap motion. It may also be possible to simulate the effect that stent graft deployment has on the AD yielding interesting insights into the changing haemodynamics during surgery.

This work is on-going and being preformed in collaboration with Dr Nicholas Gaddum, Dr Alia Noranni (Imaging and Biomedical Engineering, Kings College London) and Dr C. Alberto Figueroa (Conrad Jobst Vascular Research Lab, University of Michigan Health Systems).

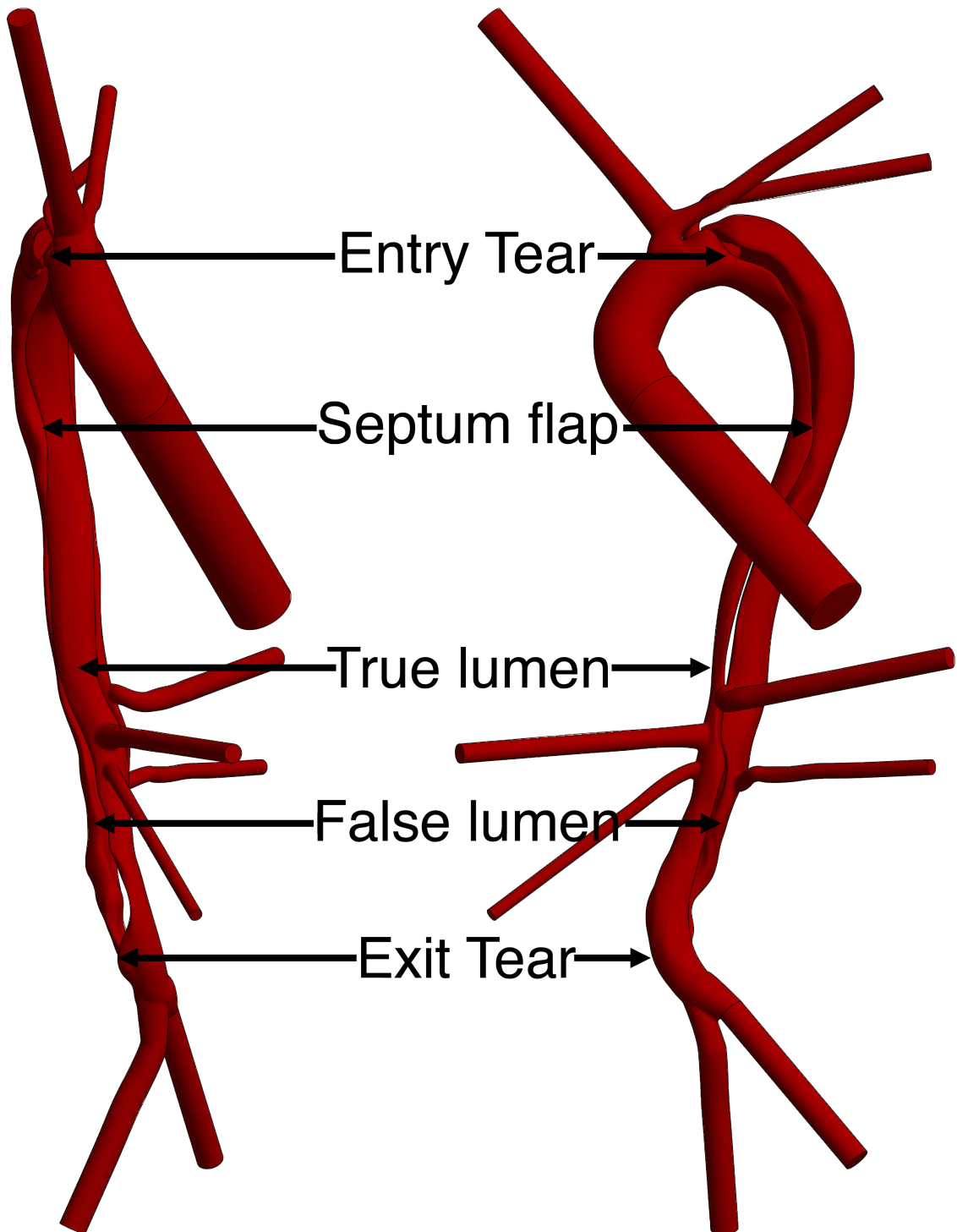


Figure 8.6: Other Contributions - Patient Specific segmentation for 3D printing: Patient B: CAD model of AD. The image shows a front and side elevation of the CAD model. Entry tear, exit tear, TL, FL and septum flap are indicated. A number of the vessels have been rotated so the model can lie flat without vessels impinging on one another. The septum flap was artificially thickened due to silicone's structural integrity. The model only includes the primary entry and exit tears. As before, the vessels were extended to allow attachment to various fittings.

BIBLIOGRAPHY

- [1] ALASTRUEY, J., PARKER, K., PEIRÓ, J., BYRD, S., AND SHERWIN, S. Modelling the circle of Willis to assess the effects of anatomical variations and occlusions on cerebral flows. *J. Biomech.* *40*, 8 (Jan 2007), 1794–1805.
- [2] ALIMOHAMMADI, M., AGU, O., BALABANI, S., AND DÍAZ-ZUCCARINI, V. Development of a patient-specific simulation tool to analyse aortic dissections: Assessment of mixed patient-specific flow and pressure boundary conditions. *Med. Eng. Phys.* *36*, 3 (Mar 2014), 275–284.
- [3] ANTIGA, L. *Patient-specific modeling of geometry and blood flow in large arteries*. Thesis, Politecnico di Milano, 2002.
- [4] AUTODESK. Inventor, 2015.
- [5] BAAIJENS, F. P. T. A fictitious domain/mortar element method for fluid-structure interaction. *Int. J. Numer. Methods Fluids* *35*, 7 (Apr 2001), 743–761.
- [6] BEN AHMED, S., DILLON-MURPHY, D., AND FIGUEROA, C. A. Computational study of anatomical risk factors in idealized models of type B aortic dissection. *Eur. J. Vasc. Endovasc. Surg.* (Paper accepted 2016, awaiting publication).
- [7] BERGUER, R., PARODI, J. C., SCHLICHT, M., AND KHANAFER, K. Experimental and clinical evidence supporting septectomy in the primary treatment of acute type B thoracic aortic dissection. *Ann. Vasc. Surg.* *29*, 2 (Feb 2015), 167–173.
- [8] BERNSTEIN, M. A., ZHOU, X. J., POLZIN, J. A., KING, K. F., GANIN, A., PELC, N. J., AND GLOVER, G. H. Concomitant gradient terms in phase contrast MR: Analysis and correction. *Magn. Reson. Med.* *39*, 2 (Feb 1998), 300–308.

- [9] BIGLINO, G., VERSCHUEREN, P., ZEGELS, R., TAYLOR, A. M., AND SCHIEVANO, S. Rapid prototyping compliant arterial phantoms for in-vitro studies and device testing. *J. Cardiovasc. Magn. Reson.* 15, 1 (2013), 2.
- [10] BÖCKLER, D., SCHUMACHER, H., GANTEN, M., VON TENGG-KOBLIGK, H., SCHWARZBACH, M., FINK, C., KAUCZOR, H.-U., BARDENHEUER, H., AND ALLENBERG, J.-R. Complications after endovascular repair of acute symptomatic and chronic expanding Stanford type B aortic dissections. *J. Thorac. Cardiovasc. Surg.* 132, 2 (Aug 2006), 361–368.e4.
- [11] BOUTOUYRIE, P., LAURENT, S., BENETOS, A., GIRERD, X. J., HOEKS, A. P., AND SAFAR, M. E. Opposing effects of ageing on distal and proximal large arteries in hypertensives. *J. Hypertens.* 10, Supplement (Aug 1992), S87–S92.
- [12] BOUTOUYRIE, P., LAURENT, S., AND BRIET, M. Importance of arterial stiffness as cardiovascular risk factor for future development of new type of drugs. *Fundam. Clin. Pharmacol.* 22, 3 (jun 2008), 241–246.
- [13] BRONZINO, J. D. *Biomedical engineering handbook, volume I*. Springer, 1999.
- [14] CARDAMONE, L., VALENTÍN, A., EBERTH, J. F., AND HUMPHREY, J. D. Origin of axial prestretch and residual stress in arteries. *Biomech. Model. Mechanobiol.* 8, 6 (Dec 2009), 431–446.
- [15] CHEN, D., MÜLLER-ESCHNER, M., KOTELIS, D., BÖCKLER, D., VENTIKOS, Y., AND VON TENGG-KOBLIGK, H. A longitudinal study of Type-B aortic dissection and endovascular repair scenarios: Computational analyses. *Med. Eng. Phys.* 35, 9 (Sep 2013), 1321–1330.
- [16] CHENG, Z., TAN, F. P. P., RIGA, C. V., BICKNELL, C. D., HAMADY, M. S., GIBBS, R. G. J., WOOD, N. B., AND XU, X. Y. Analysis of flow patterns in

- a patient-specific aortic dissection model. *J. Biomech. Eng.* 132, 5 (May 2010), 051007.
- [17] CHOI, G., CHENG, C. P., WILSON, N. M., AND TAYLOR, C. A. Methods for quantifying three-dimensional deformation of arteries due to pulsatile and non-pulsatile forces: Implications for the design of stents and stent grafts. *Ann. Biomed. Eng.* 37, 1 (Jan 2009), 14–33.
- [18] CIBC. Imaging Institute (SCI). Seg3d: Volumetric image segmentation and visualization, 2015.
- [19] CLOUGH, R. E., HUSSAIN, T., URIBE, S., GREIL, G. F., RAZAVI, R., TAYLOR, P. R., SCHAEFFTER, T., AND WALTHAM, M. A new method for quantification of false lumen thrombosis in aortic dissection using magnetic resonance imaging and a blood pool contrast agent. *J. Vasc. Surg.* 54, 5 (2011), 1251–1258.
- [20] CLOUGH, R. E., WALTHAM, M., GIESE, D., TAYLOR, P. R., AND SCHAEFFTER, T. A new imaging method for assessment of aortic dissection using four-dimensional phase contrast magnetic resonance imaging. *J. Vasc. Surg.* 55, 4 (Apr 2012), 914–923.
- [21] COADY, M. A., IKONOMIDIS, J. S., CHEUNG, A. T., MATSUMOTO, A. H., DAKE, M. D., CHAIKOF, E. L., CAMBRIA, R. P., MORA-MANGANO, C. T., SUNDT, T. M., AND SELLKE, F. W. Surgical management of descending thoracic aortic disease: open and endovascular approaches: A scientific statement from the american heart association. *Circulation* 121, 25 (jun 2010), 2780–2804.
- [22] CRAIEM, D., CHIRONI, G., REDHEUIL, A., CASCIARO, M., MOUSSEAUX, E., SIMON, A., AND ARMENTANO, R. L. Aging impact on thoracic aorta 3D morphometry in intermediate-risk subjects: looking beyond coronary arteries with non-

- contrast cardiac CT. *Ann. Biomed. Eng.* 40, 5 (May 2012), 1028–1038.
- [23] CUOMO, F., ROCCABIANCA, S., DILLON-MURPHY, D., XIAO, N., HUMPHREY, J., AND FIGUEROA, C. A. Effects of age-associated regional changes in human central artery mechanics on systemic hemodynamics revealed by computational modeling. *Am. J. Hypertens.* (Under review).
- [24] DE BAKEY, M. E., COOLEY, D. A., AND CREECH, O. Surgical considerations of dissecting aneurysm of the aorta. *Ann. Surg.* 142, 4 (Oct 1955), 586–612.
- [25] DE FIGUEIREDO BORGES, L., AND SAMPAIO GUTIERREZ, P. Possible mechanical roles of glycosaminoglycans in thoracic aortic dissection and associations with dysregulated transforming growth factor-beta. *J. Vasc. Res.* 50, 3 (2013), 197–199.
- [26] DILLON-MURPHY, D., NOORANI, A., HENNINGSSON, M., AND FIGUEROA, C. A. Strain quantification via dual phase black blood MRI in healthy and aortic dissection subjects. *Med. Image Anal.* (Under review).
- [27] DILLON-MURPHY, D., NOORANI, A., NORDSLETTEN, D., AND FIGUEROA, C. A. Multi-modality image-based computational analysis of haemodynamics in aortic dissection. *Biomech. Model. Mechanobiol.* 30 (Aug 2016), 857–876.
- [28] DIXON, B. S. Why don't fistulas mature? *Kidney Int.* 70, 8 (Oct 2006), 1413–22.
- [29] DONEA, J., AND HUERTA, A. *Finite element methods for flow problems.* 2003.
- [30] DRANEY, M. T., ARKO, F. R., ALLEY, M. T., MARKL, M., HERFKENS, R. J., PELC, N. J., ZARINS, C. K., AND TAYLOR, C. A. Quantification of vessel wall motion and cyclic strain using cine phase contrast MRI: In vivo validation in the porcine aorta. *Magn. Reson. Med.* 52, 2 (Aug 2004), 286–295.
- [31] DRANEY, M. T., HERFKENS, R. J., HUGHES, T. J. R., PELC, N. J., WEDDING, K. L., ZARINS, C. K., AND TAYLOR, C. A. Quantification of vessel wall cyclic

- strain using cine phase contrast magnetic resonance imaging. *Ann. Biomed. Eng.* 30, 8 (Sep 2002), 1033–1045.
- [32] EBERTH, J. F., GRESHAM, V. C., REDDY, A. K., POPOVIC, N., WILSON, E., AND HUMPHREY, J. D. Importance of pulsatility in hypertensive carotid artery growth and remodeling. *J. Hypertens.* 27, 10 (Oct 2009), 2010–2021.
- [33] EBERTH, J. F., POPOVIC, N., GRESHAM, V. C., WILSON, E., AND HUMPHREY, J. D. Time course of carotid artery growth and remodeling in response to altered pulsatility. *AJP Hear. Circ. Physiol.* 299, 6 (Dec 2010), H1875–H1883.
- [34] ELEFTERIADES, J. A., LOVOULOS, C. J., COADY, M. A., TELLIDES, G., KOPF, G. S., AND RIZZO, J. A. Management of descending aortic dissection. *Ann. Thorac. Surg.* 67, 6 (jun 1999), 2002–2005.
- [35] ELLIS, P. R., COOLEY, D. A., AND DE BAKEY, M. E. Clinical considerations and surgical treatment of annulo-aortic ectasia. Report of successful operation. *J. Thorac. Cardiovasc. Surg.* 42 (Sep 1961), 363–70.
- [36] ERBEL, R. Diagnosis and management of aortic dissection Task Force on Aortic Dissection, European Society of Cardiology. *Eur. Heart J.* 22, 18 (Sep 2001), 1642–1681.
- [37] ESMAILY MOGHADAM, M., VIGNON-CLEMENTEL, I. E., FIGLIOLA, R., AND MARSDEN, A. L. A modular numerical method for implicit 0D/3D coupling in cardiovascular finite element simulations. *J. Comput. Phys.* 244 (Jul 2013), 63–79.
- [38] EVANGELISTA, A., GALUPPO, V., GRUOSSO, D., CUÉLLAR, H., TEIXIDÓ, G., AND RODRÍGUEZ-PALOMARES, J. Role of entry tear size in type B aortic dissection. *2Annals Cardiothorac. Surg.* 3, 4 (Nov 2014), 403–405.

- [39] EVANGELISTA, A., SALAS, A., RIBERA, A., FERREIRA-GONZALEZ, I., CUELLAR, H., PINEDA, V., GONZALEZ-ALUJAS, T., BIJNENS, B., PERMANYER-MIRALDA, G., AND GARCIA-DORADO, D. Long-term outcome of aortic dissection with patent false lumen: predictive role of entry tear size and location. *Circulation* 125, 25 (jun 2012), 3133–3141.
- [40] FATTORI, R., NAPOLI, G., LOVATO, L., GRAZIA, C., PIVA, T., ROCCHI, G., ANGELI, E., DI BARTOLOMEO, R., AND GAVELLI, G. Descending thoracic aortic diseases: Stent-graft repair. *Radiology* 229, 1 (Oct 2003), 176–83.
- [41] FIGUEROA, C. A. *A coupled-momentum method to model blood flow and vessel deformation in human arteries: Applications in disease research and simulation-based medical planning*. Stanford University, March 2006.
- [42] FIGUEROA, C. A., KHLEBNIKOV, R., LAU, K. D., XIAO, N., FONT, M. A., DILLON-MURPHY, D., VIEIRA, M. S., AND ARTHURS, C. J. CRIMSON: Cardiovascular Integrated Modelling and Simulation. *Comput. Methods Programs Biomed.* (In preperation).
- [43] FISHER, E. R., STERN, E. J., GODWIN, J. D., OTTO, C. M., AND JOHNSON, J. A. Acute aortic dissection: Typical and atypical imaging features. *RadioGraphics* 14, 6 (Nov 1994), 1263–1271.
- [44] FLOHR, T., PROKOP, M., BECKER, C., SCHOEPF, U., KOPP, A., WHITE, R., SCHALLER, S., AND OHNESORGE, B. A retrospectively ECG-gated multislice spiral CT scan and reconstruction technique with suppression of heart pulsation artifacts for cardio-thoracic imaging with extended volume coverage. *Eur. Radiol.* 12, 6 (jun 2002), 1497–1503.
- [45] FORMAGGIA, L., LAMPONI, D., TUVERI, M., AND VENEZIANI, A. Numerical

- modeling of 1D arterial networks coupled with a lumped parameters description of the heart. *Comput. Methods Biomech. Biomed. Engin.* 9, 5 (Oct 2006), 273–288.
- [46] FORMAGGIA, L., NOBILE, F., QUARTERONI, A., AND VENEZIANI, A. Multiscale modelling of the circulatory system: a preliminary analysis. *Comput. Vis. Sci.* 2, 2-3 (Dec 1999), 75–83.
- [47] FOX, K. M., AND FERRARI, R. Heart rate: a forgotten link in coronary artery disease? *Nat. Rev. Cardiol.* 8, 7 (Apr 2011), 369–379.
- [48] FUNG, Y. C. *Biomechanics*. Springer New York, New York, NY, 1993.
- [49] GASSER, T. C., AND HOLZAPFEL, G. A. Modeling Plaque Fissuring and Dissection during Balloon Angioplasty Intervention. *Ann. Biomed. Eng.* 35, 5 (Apr 2007), 711–723.
- [50] GATEHOUSE, P. D., ROLF, M. P., GRAVES, M. J., HOFMAN, M. B., TOTMAN, J., WERNER, B., QUEST, R. A., LIU, Y., VON SPICZAK, J., DIERINGER, M., FIRMIN, D. N., VAN ROSSUM, A., LOMBARDI, M., SCHWITTER, J., SCHULZ-MENGER, J., AND KILNER, P. J. Flow measurement by cardiovascular magnetic resonance: a multi-centre multi-vendor study of background phase offset errors that can compromise the accuracy of derived regurgitant or shunt flow measurements. *J. Cardiovasc. Magn. Reson.* 12, 1 (Jan 2010), 5.
- [51] GIL, A., ARRANZ CARREÑO, A., BONET, J., AND HASSAN, O. The Immersed Structural Potential Method for haemodynamic applications. *J. Comput. Phys.* 229, 22 (Nov 2010), 8613–8641.
- [52] GIL, A. J., ARRANZ CARREÑO, A., BONET, J., AND HASSAN, O. An enhanced immersed structural potential method for fluid-structure interaction. *J. Comput. Phys.* 250 (2013), 178–205.

- [53] GLOWER, D. D., SPEIER, R. H., WHITE, W. D., SMITH, L. R., RANKIN, J. S., AND WOLFE, W. G. Management and long-term outcome of aortic dissection. *Ann. Surg.* 214, 1 (Jul 1991), 31–41.
- [54] GLOWINSKI, R., PAN, T. W., AND PERIAUX, J. A fictitious domain method for Dirichlet problem and applications. *Comput. Methods Appl. Mech. Eng.* 111, 3 (1994), 283–303.
- [55] GREENBERG, R., KHWAJA, J., HAULON, S., AND FULTON, G. Aortic dissections: new perspectives and treatment paradigms. *Eur. J. Vasc. Endovasc. Surg.* 26, 6 (Dec 2003), 579–586.
- [56] HAGAN, P. Acute aortic dissection: presentation, management and outcomes in 1996 - results from the International Registry for Aortic Dissection (IRAD). *J. Am. Coll. Cardiol.* 31, 2 (Feb 1998), 217A.
- [57] HARTNELL, G. G. Imaging of aortic aneurysms and dissection: CT and MRI. *J. Thorac. Imaging* 16, 1 (2001), 35–46.
- [58] HAUGHTON, D., AND MERODIO, J. The elasticity of arterial tissue affected by Marfan’s syndrome. *Mech. Res. Commun.* 36, 6 (Sep 2009), 659–668.
- [59] HEIM, L., POOLE, R. J., WARWICK, R., AND POUILLIS, M. The concept of aortic replacement based on computational fluid dynamic analysis: patient-directed aortic replacement. *Interact. Cardiovasc. Thorac. Surg.* 16, 5 (May 2013), 583–588.
- [60] HERMENT, A., LEFORT, M., KACHENOURA, N., DE CESARE, A., TAVIANI, V., GRAVES, M. J., PELLOT-BARAKAT, C., FROUIN, F., AND MOUSSEAUX, E. Automated estimation of aortic strain from steady-state free-precession and phase contrast MR images. *Magn. Reson. Med.* 65, 4 (Apr 2011), 986–993.

- [61] HESCH, C., GIL, A., ARRANZ CARREÑO, A., AND BONET, J. On continuum immersed strategies for fluid-structure interaction. *Comput. Methods Appl. Mech. Eng.* 247-248 (Nov 2012), 51–64.
- [62] HICKSON, S. S., BUTLIN, M., GRAVES, M., TAVIANI, V., AVOLIO, A. P., MCENERY, C. M., AND WILKINSON, I. B. The relationship of age with regional aortic stiffness and diameter. *JACC Cardiovasc. Imaging* 3, 12 (Dec 2010), 1247–1255.
- [63] HUGHES, T. J., AND WELLS, G. N. Conservation properties for the Galerkin and stabilised forms of the advection-diffusion and incompressible Navier-Stokes equations. *Comput. Methods Appl. Mech. Eng.* 194, 9-11 (Mar 2005), 1141–1159.
- [64] HUNTER, P. J., PULLAN, A. J., AND SMAILL, B. H. Modeling total heart function. *Annu. Rev. Biomed. Eng.* 5, 1 (Aug 2003), 147–177.
- [65] ISNARD, R. N., PANNIER, B. M., LAURENT, S., LONDON, G. M., DIEBOLD, B., AND SAFAR, M. E. Pulsatile diameter and elastic modulus of the aortic arch in essential hypertension: A noninvasive study. *J. Am. Coll. Cardiol.* 13, 2 (Feb 1989), 399–405.
- [66] JANSEN, K. E., WHITING, C. H., AND HULBERT, G. M. A generalized- α method for integrating the filtered Navier-Stokes equations with a stabilized finite element method. *Comput. Methods Appl. Mech. Eng.* 190, 3-4 (Oct 2000), 305–319.
- [67] JUVONEN, T., ERGIN, M. A., GALLA, J. D., LANSMAN, S. L., MCCULLOUGH, J. N., NGUYEN, K., BODIAN, C. A., EHRLICH, M. P., SPIELVOGEL, D., KLEIN, J. J., AND GRIEPP, R. B. Risk factors for rupture of chronic type B dissections. *J. Thorac. Cardiovasc. Surg.* 117, 4 (Apr 1999), 776–86.
- [68] KARMONIK, C., BISMUTH, J., DAVIES, M. G., SHAH, D. J., YOUNES, H. K., AND LUMSDEN, A. B. A Computational Fluid Dynamics Study Pre- and Post-

- Stent Graft Placement in an Acute Type B Aortic Dissection. *Vasc. Endovascular Surg.* 45, 2 (Feb 2011), 157–164.
- [69] KARMONIK, C., BISMUTH, J., REDEL, T., ANAYA-AYALA, J. E., DAVIES, M. G., SHAH, D. J., AND LUMSDEN, A. B. Impact of tear location on hemodynamics in a type B aortic dissection investigated with computational fluid dynamics. In *2010 Annu. Int. Conf. IEEE Eng. Med. Biol.* (Aug 2010), vol. 2010, IEEE, pp. 3138–3141.
- [70] KARMONIK, C., BISMUTH, J., SHAH, D. J., DAVIES, M. G., PURDY, D., AND LUMSDEN, A. B. Computational study of haemodynamic effects of entry- and exit-tear coverage in a debakey type III aortic dissection: Technical report. *Eur. J. Vasc. Endovasc. Surg.* 42, 2 (Aug 2011), 172–177.
- [71] KARMONIK, C., BISMUTH, J. X., DAVIES, M. G., AND LUMSDEN, A. B. Computational hemodynamics in the human aorta: A computational fluid dynamics study of three cases with patient-specific geometries and inflow rates. *Technol. Heal. Care* 16, 5 (Jan 2008), 343–354.
- [72] KARMONIK, C., DURAN, C., SHAH, D. J., ANAYA-AYALA, J. E., DAVIES, M. G., LUMSDEN, A. B., AND BISMUTH, J. Preliminary findings in quantification of changes in septal motion during follow-up of type B aortic dissections. *J. Vasc. Surg.* 55, 5 (May 2012), 1419–1426.e1.
- [73] KARMONIK, C., MULLER-ESCHNER, M., PARTOVI, S., GEISBUSCH, P., GANTEN, M.-K., BISMUTH, J., DAVIES, M. G., BOCKLER, D., LOEBE, M., LUMSDEN, A. B., AND TENGG-KOBLIGK, H. V. Computational fluid dynamics investigation of chronic aortic dissection hemodynamics versus normal aorta. *Vasc. Endovascular Surg.* 47, 8 (Nov 2013), 625–631.

- [74] KARMONIK, C., PARTOVI, S., MÜLLER-ESCHNER, M., BISMUTH, J., DAVIES, M. G., SHAH, D. J., LOEBE, M., BÖCKLER, D., LUMSDEN, A. B., AND VON TENGG-KOBLIGK, H. Longitudinal computational fluid dynamics study of aneurysmal dilatation in a chronic DeBakey type III aortic dissection. *J. Vasc. Surg.* 56, 1 (Jul 2012), 260–263.e1.
- [75] KARTHIKESALINGAM, A., HOLT, P., HINCHLIFFE, R., THOMPSON, M., AND LOFTUS, I. The diagnosis and management of aortic dissection. *Vasc. Endovascular Surg.* 44, 3 (Apr 2010), 165–169.
- [76] KERCKHOFFS, R. C. P., NEAL, M. L., GU, Q., BASSINGTHWAIGHTE, J. B., OMENS, J. H., AND MCCULLOCH, A. D. Coupling of a 3D finite element model of cardiac ventricular mechanics to lumped systems models of the systemic and pulmonic circulation. *Ann. Biomed. Eng.* 35, 1 (Dec 2006), 1–18.
- [77] KHAN, I. A. Clinical, diagnostic, and management perspectives of aortic dissection. *Chest* 122, 1 (Jul 2002), 311–328.
- [78] KHOYNEZHAD, A., WALOT, I., KRUSE, M. J., RAPAE, T., DONAYRE, C. E., AND WHITE, R. A. Distribution of intimomedial tears in patients with type B aortic dissection. *J. Vasc. Surg.* 52, 3 (Sep 2010), 562–568.
- [79] KIM, H. J., VIGNON-CLEMENTEL, I. E., FIGUEROA, C. A., LADISA, J. F., JANSEN, K. E., FEINSTEIN, J. A., AND TAYLOR, C. A. On coupling a lumped parameter heart model and a three-dimensional finite element aorta model. *Ann. Biomed. Eng.* 37, 11 (Nov 2009), 2153–2169.
- [80] KINGSTON, H. M. *ABC of clinical genetics*, 3rd ed. BMJ Books, London, 2002.
- [81] KUSAGAWA, H. Changes in False Lumen After Transluminal Stent-Graft Placement in Aortic Dissections: Six Years' Experience. *Circulation* 111, 22 (jun 2005), 2951–

- 2957.
- [82] LAU, K. D., AND FIGUEROA, C. A. Simulation of short-term pressure regulation during the tilt test in a coupled 3D-0D closed-loop model of the circulation. *Biomech. Model. Mechanobiol.* 14, 4 (Aug 2015), 915–929.
- [83] LAVINGIA, K. S., LARION, S., AHANCHI, S. S., AMMAR, C. P., BHASIN, M., MIRZA, A. K., DEXTER, D. J., AND PANNETON, J. M. Volumetric analysis of the initial index computed tomography scan can predict the natural history of acute uncomplicated type B dissections. *J. Vasc. Surg.* 62, 4 (Oct 2015), 893–899.
- [84] LEHOUX, S., TRONC, F., AND TEDGUI, A. Mechanisms of blood flow-induced vascular enlargement. *Biorheology* 39, 3-4 (2002), 319–324.
- [85] LEPAGE, M. A., QUINT, L. E., SONNAD, S. S., DEEB, G. M., AND WILLIAMS, D. M. Aortic dissection: CT features that distinguish true lumen from false lumen. *Am. J. Roentgenol.* 177, 1 (Jul 2001), 207–211.
- [86] LIU, X., WU, H., BYRNE, M., KRANE, S., AND JAENISCH, R. Type III collagen is crucial for collagen I fibrillogenesis and for normal cardiovascular development. *Proc. Natl. Acad. Sci.* 94, 5 (Mar 1997), 1852–1856.
- [87] LOEWE, C., CZERNY, M., SODECK, G. H., TA, J., SCHODER, M., FUNOVICS, M., DUMFARTH, J., EHRLICH, M., GRIMM, M., AND LAMMER, J. A new mechanism by which an acute type B aortic dissection is primarily complicated, becomes complicated, or remains uncomplicated. *Ann. Thorac. Surg.* 93, 4 (Apr 2012), 1215–1222.
- [88] LYONS, O., CLOUGH, R., PATEL, A., SAHA, P., CARRELL, T., AND TAYLOR, P. Endovascular management of stanford type A dissection or intramural hematoma with a distal primary entry tear. *J. Endovasc. Ther.* 18, 4 (Aug 2011), 591–600.

- [89] MANI, K., CLOUGH, R., LYONS, O. T. A., BELL, R., CARRELL, T. W., ZAYED, H., WALTHAM, M., AND TAYLOR, P. R. Predictors of outcome after endovascular repair for chronic type B dissection. *Eur. J. Vasc. Endovasc. Surg.* 43, 4 (Apr 2012), 386–391.
- [90] MARKL, M., BAMMER, R., ALLEY, M., ELKINS, C. J., DRANEY, M. T., BARNETT, A., MOSELEY, M., GLOVER, G. H., AND PELC, N. J. Generalized reconstruction of phase contrast MRI: Analysis and correction of the effect of gradient field distortions. *Magn. Reson. Med.* 50, 4 (Oct 2003), 791–801.
- [91] MASUDA, Y., TAKANASHI, K., TAKASU, J., MOROOKA, N., AND INAGAKI, Y. Expansion rate of thoracic aortic aneurysms and influencing factors. *Chest* 102, 2 (Aug 1992), 461–466.
- [92] MATLAB. *version 7.14.0.739 (R2012a)*. The MathWorks Inc., Natick, Massachusetts, 2012.
- [93] MCGEE, E. C., PHAM, D. T., AND GLEASON, T. G. Chronic descending aortic dissections. *Semin. Thorac. Cardiovasc. Surg.* 17, 3 (Sep 2005), 262–267.
- [94] MCMAHON, M. A., AND SQUIRRELL, C. A. Multidetector CT of aortic dissection: A pictorial review. *RadioGraphics* 30, 2 (Mar 2010), 445–460.
- [95] MÉSZÁROS, I., MÓROCZ, J., SZLÁVI, J., SCHMIDT, J., TORNÓCI, L., NAGY, L., AND SZÉP, L. Epidemiology and clinicopathology of aortic dissection. *Chest* 117, 5 (May 2000), 1271–8.
- [96] MOFRAD, M. R. K., AND KAMM, R. D. *Cytoskeletal mechanics: models and measurements in cell mechanics*. Cambridge University Press, 2006.
- [97] MORRISON, T. M., CHOI, G., ZARINS, C. K., AND TAYLOR, C. A. Circumferential and longitudinal cyclic strain of the human thoracic aorta: Age-related changes.

- J. Vasc. Surg.* 49, 4 (Apr 2009), 1029–1036.
- [98] MUHS, B., VINCKEN, K., VAN PREHN, J., STONE, M., BARTELS, L., PROKOP, M., MOLL, F., AND VERHAGEN, H. Dynamic cine-CT angiography for the evaluation of the thoracic aorta; insight in dynamic changes with implications for thoracic endograft treatment. *Eur. J. Vasc. Endovasc. Surg.* 32, 5 (Nov 2006), 532–536.
- [99] NEDERVEEN, A. J., AVRIL, S., AND SPEELMAN, L. MRI strain imaging of the carotid artery: Present limitations and future challenges. *J. Biomech.* 47, 4 (Mar 2014), 824–833.
- [100] NICHOLLS, F. Observations concerning the body of his late majesty, October 26, 1760, by Frank Nicholls, MDRS physician to his late majesty. *Philos. Trans.* 52 (1761), 265–275.
- [101] NICHOLS, W., AND O’ROURKE, M. *McDonald’s blood flow in arteries: theoretical, experimental and clinical principles [hardcover]*. CRC Press; 4 edition, 1998.
- [102] NIENABER, C. A. Aortic dissection: New frontiers in diagnosis and management: Part II: Therapeutic management and follow-up. *Circulation* 108, 6 (Aug 2003), 772–778.
- [103] NIENABER, C. A., AND EAGLE, K. A. Aortic dissection: new frontiers in diagnosis and management Part I: From etiology to diagnostic strategies. *Circulation* 108, 5 (2003), 628–635.
- [104] NIENABER, C. A., KISCHE, S., ROUSSEAU, H., EGGBRECHT, H., REHDE, T. C., KUNDT, G., GLASS, A., SCHEINERT, D., CZERNY, M., KLEINFELDT, T., ZIPFEL, B., LABROUSSE, L., FATTORI, R., AND INCE, H. Endovascular repair of

- type B aortic dissection: long-term results of the randomized investigation of stent grafts in aortic dissection trial. *Circ. Cardiovasc. Interv.* 6, 4 (Aug 2013), 407–416.
- [105] NOKES, L., JENNINGS, D., FLINT, T., AND TURTON, B. *Introduction to medical electronics applications*. Elsevier Science, 1995.
- [106] NORDSLETTEN, D., KAY, D., AND SMITH, N. A non-conforming monolithic finite element method for problems of coupled mechanics. *J. Comput. Phys.* 229, 20 (Oct 2010), 7571–7593.
- [107] NORDSLETTEN, D., MCCORMICK, M., KILNER, P. J., HUNTER, P., KAY, D., AND SMITH, N. P. Fluid-solid coupling for the investigation of diastolic and systolic human left ventricular function. *Int. j. numer. method. biomed. eng.* 27, 7 (Jul 2011), 1017–1039.
- [108] O’ROURKE, M. F., AND HASHIMOTO, J. Mechanical factors in arterial aging. *J. Am. Coll. Cardiol.* 50, 1 (Jul 2007), 1–13.
- [109] OTTESEN, J. T., OLUFSEN, M. S., AND LARSEN, J. K. *Applied mathematical models in human physiology*. Monographs on Mathematical Modeling and Computation. Society for Industrial and Applied Mathematics, 2004.
- [110] PAPE, L. A., TSAI, T. T., ISSELBACHER, E. M., OH, J. K., O’GARA, P. T., EVANGELISTA, A., FATTORI, R., MEINHARDT, G., TRIMARCHI, S., BOSSONE, E., SUZUKI, T., COOPER, J. V., FROELICH, J. B., NIENABER, C. A., AND EAGLE, K. A. Aortic diameter \geq 5.5 cm is not a good predictor of type A aortic dissection: Observations from the International Registry of Acute Aortic Dissection (IRAD). *Circulation* 116, 10 (Sep 2007), 1120–1127.
- [111] PESKIN, C. S. Flow patterns around heart valves: A numerical method. *J. Comput. Phys.* 10, 2 (Oct 1972), 252–271.

- [112] POPE, S., ELLWEIN, L., ZAPATA, C., NOVAK, V., KELLEY, C., AND OLUFSEN, M. Estimation and identification of parameters in a lumped cerebrovascular model. *Math. Biosci. Eng.* 6, 1 (Dec 2008), 93–115.
- [113] QANADLI, S. D., EL HAJJAM, M., MESUROLLE, B., LAVISSE, L., JOURDAN, O., RANDOUX, B., CHAGNON, S., AND LACOMBE, P. Motion artifacts of the aorta simulating aortic dissection on spiral CT. *J. Comput. Assist. Tomogr.* 23, 1 (Jan 1999), 1–6.
- [114] QIN, Y.-L., DENG, G., LI, T.-X., JING, R.-W., AND TENG, G.-J. Risk factors of incomplete thrombosis in the false lumen after endovascular treatment of extensive acute type B aortic dissection. *J. Vasc. Surg.* 56, 5 (Nov 2012), 1232–1238.
- [115] QUINT, L. E., PLATT, J. F., SONNAD, S. S., DEEB, G. M., AND WILLIAMS, D. M. Aortic intimal tears: Detection with spiral computed tomography. *J. Endovasc. Ther.* 10, 3 (jun 2003), 505–510.
- [116] ROCCABIANCA, S., FIGUEROA, C. A., TELLIDES, G., AND HUMPHREY, J. Quantification of regional differences in aortic stiffness in the aging human. *J. Mech. Behav. Biomed. Mater.* 29 (Jan 2014), 618–634.
- [117] RUDENICK, P., BIJNENS, B., BUTAKOFF, C., GARCÍA-DORADO, D., AND EVANGELISTA, A. Understanding hemodynamics and its determinant factors in type B aortic dissections using an equivalent lumped model. In *STACOM, Proc. Int. Conf. Med. Image Comput. Comput. Assist. Interv. LNCS vol. 7746*, vol. 7746. Springer Berlin Heidelberg, 2013, pp. 375–382.
- [118] RUDENICK, P. A., BIJNENS, B. H., GARCÍA-DORADO, D., AND EVANGELISTA, A. An in vitro phantom study on the influence of tear size and configuration on the hemodynamics of the lumina in chronic type B aortic dissections. *J. Vasc. Surg.*

- 57, 2 (Feb 2013), 464–474.e5.
- [119] RUDENICK, P. A., BIJNENS, B. H., SEGERS, P., GARCÍA-DORADO, D., AND EVANGELISTA, A. Assessment of Wall Elasticity Variations on Intraluminal Haemodynamics in Descending Aortic Dissections Using a Lumped-Parameter Model. *PLoS One* 10, 4 (Apr 2015), e0124011.
- [120] RUDENICK, P. A., BORDONE, M., BIJNENS, B. H., SOUDAH, E., ONATE, E., GARCIA-DORADO, D., AND EVANGELISTA, A. Influence of tear configuration on false and true lumen haemodynamics in type B aortic dissection. In *2010 Annu. Int. Conf. IEEE Eng. Med. Biol.* (Aug 2010), IEEE, pp. 2509–2512.
- [121] SABIK, J. F., LYTLE, B. W., BLACKSTONE, E. H., MCCARTHY, P. M., LOOP, F. D., AND COSGROVE, D. M. Long-term effectiveness of operations for ascending aortic dissections. *J. Thorac. Cardiovasc. Surg.* 119, 5 (May 2000), 946–964.
- [122] SAGAWA, K. Translation of Otto frank’s paper Die Grundform des arteriellen Pulses zeitschrift für biologie 37: 483-526 (1899). *J. Mol. Cell. Cardiol.* 22, 3 (Mar 1990), 253–254.
- [123] SAHNI, O., MÜLLER, J., JANSEN, K., SHEPHARD, M., AND TAYLOR, C. Efficient anisotropic adaptive discretization of the cardiovascular system. *Comput. Methods Appl. Mech. Eng.* 195, 41-43 (Aug 2006), 5634–5655.
- [124] SHAHCHERAGHI, N., DWYER, H. A., CHEER, A. Y., BARAKAT, A. I., AND RUTAGANIRA, T. Unsteady and three-dimensional simulation of blood flow in the human aortic arch. *J. Biomech. Eng.* 124, 4 (2002), 378.
- [125] SHERRATT, M. J. Tissue elasticity and the ageing elastic fibre. *Age (Omaha)*. 31, 4 (Dec 2009), 305–325.

- [126] SODECK, G., AND DOMANOVITS, H. D-dimer in ruling out acute aortic dissection: a systematic review and prospective cohort study: reply. *Eur. Heart J.* 29, 6 (Feb 2008), 829–829.
- [127] SOMMER, G., GASSER, T. C., REGITNIG, P., AUER, M., AND HOLZAPFEL, G. A. Dissection properties of the human aortic media: An experimental study. *J. Biomech. Eng.* 130, 2 (2008), 021007.
- [128] SORKIN, J. D., MULLER, D. C., AND ANDRES, R. Longitudinal change in height of men and women: Implications for interpretation of the body mass index: The baltimore longitudinal study of aging. *Am. J. Epidemiol.* 150, 9 (Nov 1999), 969–977.
- [129] STEIN, E., DE BORST, R., AND HUGHES, T. J. R., Eds. *Encyclopedia of computational mechanics*, vol. 1. John Wiley & Sons, Ltd, Chichester, UK, Aug 2004.
- [130] STERGIOPULOS, N., YOUNG, D., AND ROGGE, T. Computer simulation of arterial flow with applications to arterial and aortic stenoses. *J. Biomech.* 25, 12 (Dec 1992), 1477–1488.
- [131] SUBRAMANIAN, S., AND ROSELLI, E. E. Thoracic aortic dissection: long-term results of endovascular and open repair. *Semin. Vasc. Surg.* 22, 2 (jun 2009), 61–68.
- [132] SUEYOSHI, E., SAKAMOTO, I., AND UETANI, M. Growth rate of affected aorta in patients with type B partially closed aortic dissection. *Ann. Thorac. Surg.* 88, 4 (Oct 2009), 1251–1257.
- [133] TAKAMI, Y., TAJIMA, K., KATO, W., FUJII, K., HIBINO, M., MUNAKATA, H., UCHIDA, K., AND SAKAI, Y. Can we predict the site of entry tear by computed

- tomography in patients with acute type A aortic dissection? *Clin. Cardiol.* 35, 8 (Aug 2012), 500–504.
- [134] TAM, A. S., CATHERINE SAPP, M., AND ROACH, M. R. The effect of tear depth on the propagation of aortic dissections in isolated porcine thoracic aorta. *J. Biomech.* 31, 7 (Jul 1998), 673–676.
- [135] TAYLOR, C., AND FIGUEROA, C. A. Patient-specific modeling of cardiovascular mechanics. *Annu. Rev. Biomed. Eng.* 11, 1 (Aug 2009), 109–134.
- [136] THOMPSON, A. C. *George II: King and elector*. Yale University Press, 2011.
- [137] TOLENAAR, J. L., EAGLE, K. A., JONKER, F. H. W., MOLL, F. L., ELEFTERI-
ADES, J. A., AND TRIMARCHI, S. Partial thrombosis of the false lumen influences aortic growth in type B dissection. *Ann. Cardiothorac. Surg.* 3, 3 (May 2014), 275–7.
- [138] TOLENAAR, J. L., VAN KEULEN, J. W., JONKER, F. H. W., VAN HERWAARDEN, J. A., VERHAGEN, H. J., MOLL, F. L., MUHS, B. E., AND TRIMARCHI, S. Morphologic predictors of aortic dilatation in type B aortic dissection. *J. Vasc. Surg.* 58, 5 (Nov 2013), 1220–1225.
- [139] TOLENAAR, J. L., VAN KEULEN, J. W., TRIMARCHI, S., JONKER, F. H., VAN HERWAARDEN, J. A., VERHAGEN, H. J., MOLL, F. L., AND MUHS, B. E. Number of entry tears is associated with aortic growth in type B dissections. *Ann. Thorac. Surg.* 96, 1 (Jul 2013), 39–42.
- [140] TRIMARCHI, S., JONKER, F. H. W., VAN BOGERIJEN, G. H. W., TOLENAAR, J. L., MOLL, F. L., CZERNY, M., AND PATEL, H. J. Predicting aortic enlargement in type B aortic dissection. *Ann. Cardiothorac. Surg.* 3, 3 (2014), 285–291.

- [141] TRIMARCHI, S., TOLENAAR, J. L., JONKER, F. H., MURRAY, B., TSAI, T. T., EAGLE, K. A., RAMPOLDI, V., VERHAGEN, H. J., VAN HERWAARDEN, J. A., MOLL, F. L., MUHS, B. E., AND ELEFTERIADES, J. A. Importance of false lumen thrombosis in type B aortic dissection prognosis. *J. Thorac. Cardiovasc. Surg.* 145, 3 (Mar 2013), S208–S212.
- [142] TSAI, T. T., EVANGELISTA, A., NIENABER, C. A., MYRMEL, T., MEINHARDT, G., COOPER, J. V., SMITH, D. E., SUZUKI, T., FATTORI, R., LLOVET, A., FROEHLICH, J., HUTCHISON, S., DISTANTE, A., SUNDT, T., BECKMAN, J., JANUZZI, J. L., ISSELBACHER, E. M., AND EAGLE, K. A. Partial thrombosis of the false lumen in patients with acute type B aortic dissection. *N. Engl. J. Med.* 357, 4 (Jul 2007), 349–359.
- [143] TSAI, T. T., SCHLICHT, M. S., KHANAFER, K., BULL, J. L., VALASSIS, D. T., WILLIAMS, D. M., BERGUER, R., AND EAGLE, K. A. Tear size and location impacts false lumen pressure in an ex vivo model of chronic type B aortic dissection. *J. Vasc. Surg.* 47, 4 (Apr 2008), 844–851.
- [144] TSE, K. M., CHIU, P., LEE, H. P., AND HO, P. Investigation of hemodynamics in the development of dissecting aneurysm within patient-specific dissecting aneurysmal aortas using computational fluid dynamics (CFD) simulations. *J. Biomech.* 44, 5 (Mar 2011), 827–836.
- [145] VAN ANDEL, C. J., PISTECKY, P. V., AND BORST, C. Mechanical properties of porcine and human arteries: implications for coronary anastomotic connectors. *Ann. Thorac. Surg.* 76, 1 (Jul 2003), 58–64.
- [146] VAN BOGERIJEN, G. H., TOLENAAR, J. L., RAMPOLDI, V., MOLL, F. L., VAN HERWAARDEN, J. A., JONKER, F. H., EAGLE, K. A., AND TRIMARCHI, S. Pre-

- dictors of aortic growth in uncomplicated type B aortic dissection. *J. Vasc. Surg.* 59, 4 (Apr 2014), 1134–1143.
- [147] VAN PREHN, J., VINCKEN, K. L., MUHS, B. E., BARWEGEN, G. K. W., BARTELS, L. W., PROKOP, M., MOLL, F. L., AND VERHAGEN, H. J. M. Toward endografting of the ascending aorta: Insight into dynamics using dynamic cine-CTA. *J. Endovasc. Ther.* 14, 4 (Aug 2007), 551–560.
- [148] VARDOULIS, O., COPPENS, E., MARTIN, B., REYMOND, P., TOZZI, P., AND STERGIOPULOS, N. Impact of aortic grafts on arterial pressure: A computational fluid dynamics study. *Eur. J. Vasc. Endovasc. Surg.* 42, 5 (Nov 2011), 704–710.
- [149] VIGNON-CLEMENTEL, I. E., ALBERTO FIGUEROA, C., JANSEN, K. E., AND TAYLOR, C. A. Outflow boundary conditions for three-dimensional finite element modeling of blood flow and pressure in arteries. *Comput. Methods Appl. Mech. Eng.* 195, 29-32 (Oct 2006), 3776–3796.
- [150] VIGNON-CLEMENTEL, I. E., FIGUEROA, C. A., JANSEN, K. E., AND TAYLOR, C. A. Outflow boundary conditions for three-dimensional finite element modeling of blood flow and pressure in arteries. *Comput. Methods Appl. Mech. Eng.* 195, 29-32 (jun 2006), 3776–3796.
- [151] WANG, K. C., DUTTON, R. W., AND TAYLOR, C. A. Improving geometric model construction for blood flow modeling: Geometric image segmentation and image-based model construction for computational hemodynamics. *IEEE Eng. Med. Biol. Mag.* 18, 6 (1999), 33–39.
- [152] WEDDING, K. L., DRANEY, M. T., HERFKENS, R. J., ZARINS, C. K., TAYLOR, C. A., AND PELC, N. J. Measurement of vessel wall strain using cine phase contrast MRI. *J. Magn. Reson. Imaging* 15, 4 (Apr 2002), 418–428.

- [153] WEISS, G., WOLNER, I., FOLKMANN, S., SODECK, G., SCHMIDLI, J., GRABENWOGER, M., CARREL, T., AND CZERNY, M. The location of the primary entry tear in acute type B aortic dissection affects early outcome. *Eur. J. Cardio-Thoracic Surg.* 42, 3 (Sep 2012), 571–576.
- [154] WESTERHOF, N., LANKHAAR, J.-W., AND WESTERHOF, B. E. The arterial Windkessel. *Med. Biol. Eng. Comput.* 47, 2 (Feb 2009), 131–141.
- [155] WHITING, C. H., AND JANSEN, K. E. A stabilized finite element method for the incompressible Navier-Stokes equations using a hierarchical basis. *Int. J. Numer. Methods Fluids* 35, 1 (Jan 2001), 93–116.
- [156] WILBERS, C. R., CARROL, C. L., AND HNILICA, M. A. Optimal diagnostic imaging of aortic dissection. *Tex. Heart Inst. J.* 17, 4 (1990), 271–8.
- [157] WILLOTEAUX, S., LIONS, C., GAXOTTE, V., NEGAIWI, Z., AND BEREGI, J. P. Imaging of aortic dissection by helical computed tomography (CT). *Eur. Radiol.* 14, 11 (Nov 2004), 1999–2008.
- [158] WILSON, G. N. *Biochemistry and genetics PreTest self-assessment and review, third edition*. McGraw-Hill, 2007.
- [159] WITTEK, A., MILLER, K., AND NIELSEN, P. M. F. MICCAI 2012 workshop proceedings computational biomechanics for medicine VII. In *MICCAI 2012 Work. Proc. Comput. Biomech. Med. VII* (October 2012), A. Wittek, K. Miller, and P. M. F. Nielsen, Eds., pp. 165–176.
- [160] WOLF, I., VETTER, M., WEGNER, I., BÖTTGER, T., NOLDEN, M., SCHÖBINGER, M., HASTENTEUFEL, M., KUNERT, T., AND MEINZER, H.-P. The medical imaging interaction toolkit. *Med. Image Anal.* 9, 6 (2005), 594–604.

- [161] WONG, E. C. An introduction to ASL labeling techniques. *J. Magn. Reson. Imaging* 40, 1 (Jul 2014), 1–10.
- [162] WOOD, C., GIL, A., HASSAN, O., AND BONET, J. Partitioned block-Gauss-Seidel coupling for dynamic fluid-structure interaction. *Comput. Struct.* 88, 23-24 (Dec 2010), 1367–1382.
- [163] WWW.VMTK.ORG. The Vascular Modeling Toolkit.
- [164] XIAO, N., ALASTRUEY, J., AND FIGUEROA, C. A. A systematic comparison between 1-D and 3-D hemodynamics in compliant arterial models. *Int. J. Numer. Method. Biomed. Eng.* 30, 2 (Feb 2014), 204–231.
- [165] XIAO, N., HUMPHREY, J. D., AND FIGUEROA, C. A. Multi-scale computational model of three-dimensional hemodynamics within a deformable full-body arterial network. *J. Comput. Phys.* 244 (Jul 2013), 22–40.
- [166] YUSHKEVICH, P. A., PIVEN, J., HAZLETT, H. C., SMITH, R. G., HO, S., GEE, J. C., AND GERIG, G. User-guided 3D active contour segmentation of anatomical structures: Significantly improved efficiency and reliability. *Neuroimage* 31, 3 (Jul 2006), 1116–1128.
- [167] YZET, T., BOUZERAR, R., ALLART, J.-D., DEMUYNCK, F., LEGALLAIS, C., ROBERT, B., DERAMOND, H., MEYER, M.-E., AND BALÉDENT, O. Hepatic vascular flow measurements by phase contrast MRI and doppler echography: A comparative and reproducibility study. *J. Magn. Reson. Imaging* 31, 3 (Mar 2010), 579–588.
- [168] ZALZSTEIN, E., HAMILTON, R., ZUCKER, N., DIAMANT, S., AND WEBB, G. Aortic dissection in children and young adults: diagnosis, patients at risk, and outcomes. *Cardiol. Young* 13, 4 (Aug 2003), 341–4.

-
- [169] ZHANG, L., AND GAY, M. Immersed finite element method for fluid-structure interactions. *J. Fluids Struct.* 23, 6 (Aug 2007), 839–857.